MODELING THE GENERATION, DISTRIBUTION AND TRANSPORT OF POINT
DEFECTS IN OXIDE MIXED IONIC-ELECTRONIC CONDUCTORS

BY

KEITH L. DUNCAN

DISSERTATION PRESENTED TO THE GRADUATE SCHOOL OF THE
UNIVERSITY OF FLORIDA IN PARTIAL FULFILLMENT OF THE
REQUIREMENTS FOR THE DEGREE OF DOCTOR OF PHILOSOPHY

UNIVERSITY OF FLORIDA

2001

ACKNOWLEDGMENTS

I would like to thank my advisor, Dr. Eric D. Wachsman, for his support, encouragement and facilitation of my graduate research. Under his tutelage, I have come a long way in the burgeoning field of solid state electrochemistry and have been equipped to go even farther. I am also grateful to my committee members, Dr. R. T. Dehoff, Dr. R. Hummel, Dr. M. Orazem, Dr. W. Sigmund and Dr. S. Sinnott, for making themselves accessible for discussion and for challenging me to expand the horizons of my research.

I would like to thank my family. My wife Nicole and son Matthew have given me tremendous support through the ordeals of doctoral research. They allowed me to take them from their contented life in Jamaica and they endured much hardship to help realize my ambitions. Moreover, they enabled me to retain a balanced perspective, helping me to smell a few roses along the journey. I must also express my sincere appreciation for the efforts of my mother, Merdean Bennett, a single parent who gave all she could, often under trying conditions.

Finally, I thank God who through his Holy Spirit and the saving grace of Jesus, His son, shepherded me through the years. God has blessed me in countless way. He blessed me with this opportunity to study. He made a way where there was none. He provided me with the best situation in which to thrive. May all of my life be to His honor and glory. Ad majorem Dei gloriem.

TABLE OF CONTENTS

iii

LIST OF TABLES

LIST OF FIGURES

KEY TO SYMBOLS AND ABBREVIATIONS

Abbreviations

BDC   boundary defect concentration

DED   defect equilibrium diagram

ESB   erbia-stabilized bismuth oxide

GDC   gadolinia-doped ceria

MIEC   mixed ionic-electronic conductor

LSCF   lanthanum strontium cobalt iron oxide

NASA   National Aeronautical and Space Agency

OCV   *open-circuit* voltage

PEM   proton exchange membrane

SDC   samaria-doped ceria

SOFC   solid oxide fuel cell

YSZ   yttria-stabilized zirconia

Symbols

a activity of the chemical species

a_i^θ reference state

c_i concentration of the *i*th defect

c_A concentration of acceptor dopant

$c_{cat}°$ concentration of cations without trapped electrons or holes

c_{cat} total concentration of all (*charged* and *uncharged*) cations.

c_e concentration of electrons

c_h	concentration of holes
$c_{e>}$	concentration of *itinerant* electrons
$c_{h>}$	concentration of *itinerant* holes
c_{O_i}	concentration of oxygen atoms in interstitial sites
c_{O_O}	concentration of oxygen atoms in oxygen sites
c_{sp-}	concentration of *negatively charged* small polarons
c_{sp+}	concentration of *positively charged* small polarons
c_{V_A}	concentration of metal vacancies in the sublattice of cation A
c_{V_B}	concentration of metal vacancies in the sublattice of cation B
$c_{V_{A/B}}$	total concentration of A-site and B-site cation vacancies ($c_{V_A} + c_{V_B}$)
c_V, c_{V_O}	concentration of oxygen vacancies in the oxygen sublattice
$c_{V_O}^{\text{red}}$,	reduced oxygen vacancy concentration
c_{sp-}^{red}	reduced small polaron concentration
c_{d1}	concentration of the $\left(\text{Sm}'_{\text{Ce}} \circ \text{V}^{\bullet\bullet}_{\text{O}} \circ \text{Sm}'_{\text{Ce}}\right)^{\times}$ defect associate
c_{d2}	concentration of the $\left(\text{Ce}'_{\text{Ce}} \circ \text{V}^{\bullet\bullet}_{\text{O}} \circ \text{Sm}'_{\text{Ce}}\right)^{\times}$ defect associate
c_{d3}	concentration of the $\left(\text{Ce}'_{\text{Ce}} \circ \text{V}^{\bullet\bullet}_{\text{O}} \circ \text{Ce}'_{\text{Ce}}\right)^{\times}$ defect associate
c_{O*}	concentration of the *encounter group* $\left(\text{V}^{\bullet\bullet}_{\text{O}} \circ \text{O}^{2-}_{ads}\right)$
D_{ambi}	ambipolar diffusivity
D_e	electron diffusivity
D_h	hole diffusivity
D_V	oxygen vacancy diffusivity
E_g	band gap energy
f_i	activity coefficient of the ith species
F	Faraday's constant
ΔG	Gibbs' free energy associated with a reaction
I_i	current due to the ith species
I_{ext}	net current supplied to the external circuit by an SOFC

j_i	flux density of the ith species
J_i	current density of the ith species
J	total current density
k_B	Boltzmann's constant
K	mass action (equilibrium) constant for a reaction
K_-	mass action constant for the formation of *negatively charged* small polarons
K_+	mass action constant for the formation of *positively charged* small polarons
K_1	mass action constant for formation of the $\left(Sm'_{Ce} \circ V_O^{\bullet\bullet} \circ Sm'_{Ce}\right)^{\times}$ defect associate
K_2	mass action constant for formation of the $\left(Ce'_{Ce} \circ V_O^{\bullet\bullet} \circ Sm'_{Ce}\right)^{\times}$ defect associate
K_3	mass action constant for formation of the $\left(Ce'_{Ce} \circ V_O^{\bullet\bullet} \circ Ce'_{Ce}\right)^{\times}$ defect associate
K_f	mass action constant for the formation of anti-Frenkel defect pairs
K_i	mass action constant for the formation of electron-hole pairs
K_s	mass action constant for the formation of Schottky defect pairs
K_h	mass action constant for external equilibrium reaction in oxidizing conditions
K_m	mass action constant for external equilibrium reaction in intermediate conditions
K_r	mass action constant for the external equilibrium reaction in reducing conditions
K_t	mass action constant for the decomposition of ceria to cerium (III) oxide
K_r^*	unit bearing pre-exponential factor related to K_r
K_m^*	unit bearing pre-exponential factor related to K_m
L_D	Debye length
L	length (of MIEC)
N_v	density of states per unit volume in the valence bands
N_c	density of states per unit volume in the conduction bands
P_{O_2}	oxygen partial pressure (used in text)
P	oxygen partial pressure (used in equations)
P_0	oxygen partial pressure at $x = 0$, i.e., on the reducing side of MIEC membrane
P_L	oxygen partial pressure at $x = L$, i.e., on the oxidizing side of MIEC membrane

P_I	Interfacial oxygen partial pressure between the layers of a bilayered membrane
q	charge on an electron
r	radius of the charged defect
R_i	electrical resistance of the ith species
R_e	electrical resistance of electrons
R_h	electrical resistance of holes
R_V	electrical resistance of oxygen vacancies
S	cross-sectional area
t_i	transference number of the ith species
t_{ion}	ionic transference number
$\bar{t}_i$,	*effective* (average) transference number of the ith species
$\bar{t}_{ion}$,	*effective* (average) ionic transference number
t	time
T	temperature
u_i	mobility of the ith species
x	distance (positional) coordinate
z_i	charge number of the ith species
$2\text{-}\delta$	non-stoichiometry of fluorite
$3\text{-}\delta$	non-stoichiometry of perovskite
Δ_{err}	absolute error
ε_0	permittivity of free space
ε_r	relative permittivity
ϕ	electrical potential
$\Delta\Phi$	potential difference across an MIEC membrane
Φ_{app}	applied voltage (from the voltage drop across a load or an external source)
Φ_{oc}	*open-circuit* voltage

Φ_{th}	theoretical (Nernst) potential
Γ_i	rate of the formation of the ith species due to homogenous chemical reactions
κ	rate constant for a reaction
μ	chemical potential of the ith the species
$\tilde{\mu}_i$	electrochemical potential of the ith the species
v	reaction rate for a reaction
Θ	$D_e/4D_V$ or $D_h/4D_V$
σ_i	conductivity of the ith species
σ_e	electronic conductivity
σ_h	hole conductivity
σ_{el}	electron plus hole conductivity
σ_{ion}	ionic conductivity
σ_V	oxygen vacancy conductivity
σ_{tot}	total conductivity
$\overline{\sigma}_i$	average conductivity of the ith species
ψ_i	absolute activity
τ	thickness ratio
τ^*	optimal thickness ratio
ξ	number of atoms associated with the standard state of a permeating gas
ζ_J	current efficiency
ζ_P	power efficiency

Abstract of Dissertation Presented to the Graduate School of the University of Florida in Partial Fulfillment of the Requirements for the Degree of Doctor of Philosophy

MODELING THE GENERATION, DISTRIBUTION AND TRANSPORT OF POINT DEFECTS IN OXIDE MIXED IONIC-ELECTRONIC CONDUCTORS

By

Keith L. Duncan

August 2001

Chair: Dr. Eric D. Wachsman
Major Department: Materials Science and Engineering

Point defect equilibria were used to develop analytical expressions for the dependence of defect concentration on oxygen partial pressure (P_{O_2}) in mixed ionic-electronic conductors (MIECs) with the fluorite and perovskite structures. This thermodynamic model was able to reproduce the results of the conventional Brouwer approach in the Brouwer regimes but unlike that approach the models were continuous across two Brouwer regimes. To verify the model, a case study was effected for samaria-doped ceria (SDC) in which (a) the model was compared to numerical solutions of SDC defect equilibria, (b) the model was used to obtain values for the external equilibrium constant, K_r, (c) the model was fitted to experimental data for total (ionic plus electronic) conductivity as a function of P_{O_2} and (d) the impact of defect associates on defect concentration and total conductivity was evaluated. In addition K_r was correlated to the ratio of the diffusivities of the electronic and ionic species, Θ (= $D_e/4D_V$), and $K_r(3+4\Theta)^2$ constitutes a material constant.

Fundamental transport laws were then used to derive transport models for the spatial distribution and transport of defects in an MIEC in a P_{O_2} gradient with and without assuming a linear potential gradient across the MIEC. The former was found to be

applicable to true electrolytes (i.e., electrolytes with negligible electronic conductivity) while the latter had general application to all MIECs. As an advance over present models, the use of *potential dependent* rather than *fixed* boundary conditions was investigated. It was found that using *fixed* boundary conditions often caused misleading results. The transport model for *open-circuit* conditions was applied to experimental data consisting of OCV measurements for various values of P_{O_2} (on the reducing side) and at temperatures from 500 °C to 800 °C. Excellent fits of this model to the experimental data were obtained, thereby demonstrating its accuracy.

Finally, both thermodynamic and transport models were used to determine the optimal thickness ratio of a bilayered electrolyte consisting of SDC and erbia-stabilized bismuth oxide. The optimal (giving the lowest total resistance) thickness ratio of the layers was shown to depend on which layer was more resistive to the transported species, which were charged in *closed-circuit* conditions and were neutral in *open-circuit* conditions.

CHAPTER 1
INTRODUCTION

In this introduction to oxide mixed ionic-electronic conductors (MIECs) the definition, history, and importance of charge-conducting ceramics are briefly reviewed; first in general then in more specific terms. Then the applications and issues concerning MIECs are addressed more specifically. Finally, the general assumptions used in modeling the performance and properties of MIECs are discussed.

1.1 Mixed Ionic-Electronic Conductors

For a long time, ceramics were assumed to consist entirely of insulators, and little thought was given to their potential for any type of charge conduction. To varying degrees, that notion remains prevalent today. Some time ago, however, a number of events conspired to begin a change in the status quo. Unwittingly, one important motivation for this change in thinking arose from studying corrosion of the quintessential charge-conducting family, metals. While studying the growth of oxide (ceramic) films on metals, researchers began to appreciate the potential for charge conduction in ceramics.

Materials science has evolved significantly since those halcyon days, but it is only recently that the conductive properties of ceramics are being put to use. In the last 30 years, research in charge-conducting ceramics has increased significantly (though it still has a long way to go). This research, while not limited to, is dominated by the oxide family of ceramics. Specifically, scientists and engineers investigating conducting oxides are primarily concerned with two general classes: semiconductors and ion conductors. Semiconducting oxides are being developed for use in a number of technologically

1
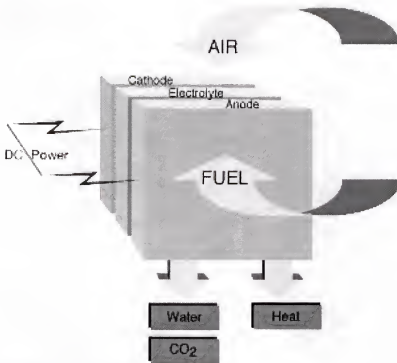
Figure 1-1. SOFC power generation.

significant devices such as lasers, solar cells, transistors and flat-panel displays. Ion-conducting oxides are being developed for use in fuel cells, batteries, sensors, gas separation membranes and oxygen pumps. The latter is addressed in this work.

1.2 Applications of Oxide Mixed-Ionic Electronic Conductors

To justify the interest in ion-conducting oxides, some elaboration on the performance of the aforementioned applications of ion-conducting oxides is required. The recent surge in oil prices in the world market makes increased efficiency in energy production from oil based products necessary. Fuel cells (Figure 1-1) have the potential to provide the required rise in efficiency. One example shows this potential. After more than 120 years of research, development and production, the most efficient internal combustion engine today offers, in ideal conditions, 40% efficiency. After thirty years of research, ordinary

fuel cells offer 70 to 80% efficiency. In other words, a fuel cell could effectively halve the pecuniary resources consumed by gasoline.

A fuel cell is an electrochemical device that converts fuel directly to electricity through an electrochemical reaction. A solid oxide fuel cell (SOFC) is a solid state device that consists of an oxide membrane and two (oxide, metal or cermet) electrodes. Oxygen from air is reduced at one electrode and fuel (e.g., natural gas) is oxidized to carbon dioxide and water at the other electrode. Both batteries and fuel cells produce electric power without conventional combustion or rotating machinery. Batteries convert stored chemical energy to electrical energy while fuel cells convert chemical energy directly to electrical energy.

Solid oxide fuel cells have many advantages: they can be modular, they can be distributed to eliminate the need for transmission lines, they operate quietly, and they do not produce nitrogen oxide pollution. SOFCs could provide higher system efficiency, higher power density, and simpler designs than fuel cells based on liquid/molten (e.g., phosphoric acid, molten carbonate) or polymer (e.g., proton exchange membranes, PEM, made of Nafion®) electrolytes. At low enough costs, they could compete with gas turbines for distributed applications.

Another area of intense research concerns lithium batteries, which have found their way into almost every portable computer on the market today. Their success was made possible by the ability of many oxides to store *large* amounts of lithium ions in their lattice structure (a process called intercalation). A significant bloc of battery research today concerns finding materials (primarily ceramic oxides) that can store even more lithium ions (for a longer battery life) and conduct them more efficiently (for better power conversion).

Although not as glamorous as fuel cell and battery applications, the use of ion-conducting oxides in gas separation membranes also promises great rewards. Somewhat ironically, membranes, or membrane reactors, have generated interest from oil refineries

for the high-temperature conversion of methane to synthesis gas, an important intermediate in the production of liquid fuels and chemicals. The use of ceramic membranes would increase the efficiency of the refining process and could lower the price consumers pay for petroleum derivatives. An oxide MIEC membrane reactor separates oxygen from air on one side. Selective hydrocarbon oxidation—for example, conversion of methane into valuable synthesis gas (CO and H_2)—occurs on the other side. Membrane reactors for converting methane to synthesis gas, offer significant economic incentives because they eliminate the need for a dedicated oxygen separation system. In more general terms, ceramic membrane reactors combine reaction and separation in a single unit and offer unique control of product selectivities and save energy by reducing recycle and separation requirements.

Another useful device based on ion-conducting oxides is the electrocatalytic reactor, also known as the oxygen pump. An electrocatalytic reactor is a fuel cell run in reverse. An applied voltage drives a specific chemical reaction by, for example, pumping oxygen across the oxide membrane. These devices may provide enhanced selectivity in the synthesis of chemicals by partial oxidation of hydrocarbons, but they are limited by high operating temperature. At lower temperatures, however, a wider range of useful reactions becomes accessible. Oxygen pumps have also drawn attention from the National Aeronautical and Space Agency (NASA) for use in their efforts to put a man on Mars.

Finally, oxide sensors, which have been used in the control of catalytic converters in automobiles since 1975 are similar in operation to SOFCs. They develop a voltage directly related to the effective oxygen partial pressure of the mix of gases that the sensor is exposed to.

1.3 Research Challenges and Opportunities

Now that the tremendous potential of oxide ion conductors has been reviewed, albeit briefly, it is pertinent to discuss the source of this potential. Succinctly, it comes from

their ability to generate, stably sustain and transport charge carrying point defects. In the most rudimentary sense, a defect may be described as any structural or compositional departure from ideal found in the lattice of a solid. Point defects refer to those departures that are located in, and characterized by a specific position in said lattice. Many materials exhibit a propensity for forming defects in their lattices and this phenomenon has generally been put to good effect in such materials by scientists and engineers. By controlling the type, concentration and distribution of defects formed in the lattice of a material its properties may, in principle, be tailored for numerous applications. For example, lattice dislocations are created in metals to improve their ductility. Likewise, in ion-conducting ceramics point defects are particularly useful for charge and mass transport. In fact, the transport properties of ion-conducting ceramics are determined wholly by the characteristics of the point defect population in a given set of operating conditions. Consequently, the development of technologies based on ion-conducting ceramics relies primarily on the ability of scientists and engineers to first understand and second control these characteristics; therein lies the problem.

Despite intense research in the field of ion-conducting ceramics, the central issue of understanding and controlling the characteristics of the point defect population is unresolved and underdeveloped. Part of the explanation for this problem lies in the complexity and sheer breadth of the field, which incorporates aspects of solid state physics, electrochemistry and thermodynamics. In this age of specialization, few scientists have training or are comfortable in all these areas. Moreover, this is compounded, insidiously, by the demands of funded research that values results more than understanding. Results mean products to sell and thus more funding.

Another issue concerning the development of MIECs, is the high temperature needed for optimal performance. That is one reason that SOFCs have been limited thus far to providing power in stationary rather than the more visible and exciting automotive applications. High operating temperatures result in long startup times that are of

sufficient duration to frustrate would-be automobile users. Additionally, high temperatures also require exotic and expensive ancillary components such as interconnects used in fuel cell stacks. Consequently, significant research effort is being devoted to solve this problem. One research path concerns discovering new candidate materials for the electrolyte [1, 2] as well as the electrodes [1 - 4] which can operate efficiently at low temperatures. Along a second path, researchers are pursuing thinner (lower resistance) electrolytes [1, 2, 5, 6]. Finally, some research is being done on bilayered SOFCs to take advantage of the properties of each layer.

Yet another issue concerns the development of catalytically active electrodes that balance the seemingly opposite tasks of compatibility (chemical and mechanical) and performance (i.e., high oxygen permeability and electronic conductivity). In other words, the electrodes need to match the thermal expansion coefficient of, and be depositable on the electrolyte (or vice versa). But they must not form any (detrimental) secondary phase at the electrolyte-electrode interface. Neither should their components diffuse (appreciably), via grain boundaries or bulk, into the electrolyte (or vice versa) over the desired life span of the system.

Additional issues concern the reliable measurement of these material properties, especially the fundamental ones. For example, numerous researchers measure conductivity with a fair degree of accuracy and repeatability. Conversely, diffusivity and activation energy, both determinants of conductivity, often cannot be measured with any reliability [7 - 9]. Sadly, these constants are of critical importance in understanding many properties of these materials. Moreover, they may serve as a guide to those researchers who attempt to model the properties and behaviour of ion-conducting ceramics.

In summary, there are several important issues concerning the understanding, development and performance of MIECs in their various applications. Although it would be good to address all of them, doing so would consume perhaps a career's worth of research. Consequently, this study addresses only a few of the uncertainties concerning

the characteristics of the defect population in ion-conducting oxides. This task is approached primarily by developing analytical models for the generation, distribution and transport of point defects in MIECs. The basic theoretical framework in which this endeavour is cast is shown in Figure 1-2. First Chapter 2 explores the generation of point defects in MIECs; a phenomenon driven by the thermodynamics of the system. General equations are developed followed by a case study on a specific MIEC. In this study the relationships between conductivity, diffusivity and non-stoichiometry are explored. In Chapter 3 transport laws are used to derive the transport properties and spatial distribution of defects in MIECs in an oxygen potential gradient. The relationships obtained in Chapter 2 are use at the gas-MIEC interface to provide appropriate boundary conditions for the system. Moreover, phenomena peculiar to an MIEC in an oxygen potential gradient are examined specifically ambipolar diffusion and energy conversion (i.e., fuel cell operation). Chapter 4 focuses on applying the models and principles obtained in the preceding chapters to guide the development of a new device. Throughout the development of the models, attempts are made to demonstrate how they might be exploited to obtain values for elusive material constants. Finally, it is hoped that these models engender a better understanding of how point defect population, operating conditions and material properties of MIECs are related. And that an improved understanding facilitates their optimization in various applications.

1.4 Major Assumptions Used in Model Development

Before moving on to the model development, it is important to spend some time discussing the assumptions that are an essential component of the framework for the development of the models. The first assumption is that local charge neutrality, which may be expressed as:

$$\sum_i z_i c_i \approx 0 \qquad (1.1)$$
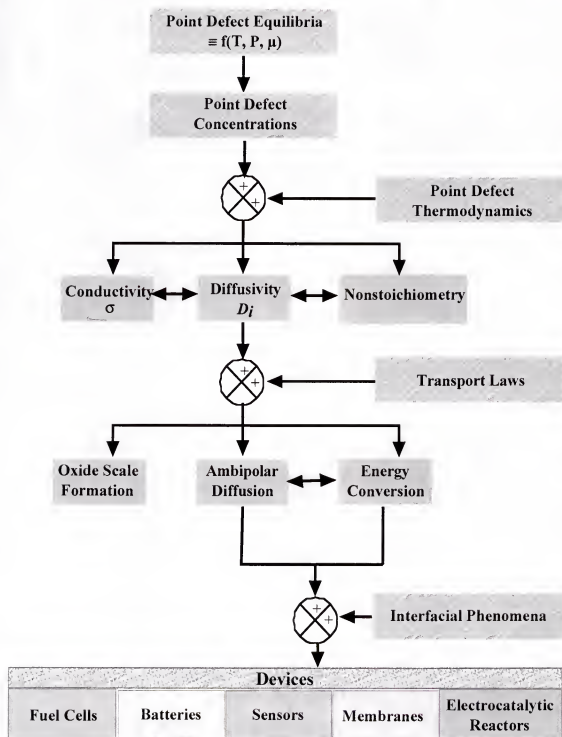
Figure 1-2. Overarching theoretical framework of this study.

is maintained throughout the MIEC; where z_i is the charge number of the ith species and c_i is concentration of the ith defect. Local charge neutrality is not a fundamental law, however, and its applicability may be compromised in the presence of high concentration gradients and large Debye lengths that may be present near (within 10 Å) to the electrode-electrolyte interface.

The Debye length, L_D, is useful as a qualitative first approximation to the degree of interaction between charged species and the magnitude of the space charge region near the electrode-electrolyte interface. It is given by the formula

$$L_D = \sqrt{\frac{\varepsilon_r \varepsilon_0 k_B T}{q^2 \sum_i z_i^2 c_i}} \tag{1.2}$$

where q is the charge on an electron, k_B is Boltzmann's constant, T is temperature, ε_r is relative permittivity and ε_0 is the permittivity of free space. For a typical MIEC operating at 1000 K, with $\varepsilon_r \approx 10$ and containing oxygen vacancies[1] and an aliovalent-acceptor dopant—where, on average, the acceptor-dopant concentration, $c_A \approx 5 \times 10^{27}$ m^{-3}; the oxygen vacancy concentration, $c_V \approx 2.5 \times 10^{27}$ m^{-3}; and the electron concentration, $c_e = 5 \times 10^{27}$ m^{-3}—$L_D \approx 0.4$ Å. This small value of L_D (less than an atomic layer) is caused by the relatively large number of charge carriers present in the typical MIEC and it gives credence to the assumption of local charge neutrality. This is in contrast to common liquid electrolytes, however, where small concentrations of the conducting ions are dissolved in a dielectric solvent, thereby allowing the build up of a large space charge region. Semiconductors are similarly characterized by small numbers of (highly mobile) electrons or holes and so the thickness of the space charge region is accordingly large ($\sim$1 to 10 µm).

---

[1] i.e., vacant oxygen sites in the lattice that behave like ions with a +2 charge.

The second assumption is that the activities of the chemical species may be sufficiently represented by their concentrations. To a significant extent, the correctness of the numerous electrochemically related formulae in solid state electrochemistry rely heavily on the assumption that the activities of the various ionic species may be replaced, without loss of accuracy, by their concentrations. However, though this assumption is common, it is not necessarily true in all circumstances. The relationship between the absolute activity ψ_i and the concentration of the ith species, is given by

$$\psi_i = c_i f_i a_i^{\theta} \tag{1.3}$$

where f_i is the activity coefficient and a_i^{θ} is a reference state (which if chosen appropriately is equal to unity). To properly assess the amount of error involved in replacing the activities of the defects by their concentrations, one needs to determine the magnitude of the activity coefficients. From the Debye-Huckel theory:

$$\ln f_i = -\frac{z_i^2 e^2}{8\pi\varepsilon_r\varepsilon_0 k_B T} \cdot \frac{L_D}{L_D + r} \tag{1.4}$$

where r is the radius of the charged defect.

For the typical MIEC described above with the ionic radius of an oxygen vacancy $\approx$ 0.1 nm, a value of $\ln f \approx 10^{-9}$ is obtained; or, in other words $f \approx 1$. This result suggests that, at least on a rudimentary level, the assumption that the activities of the defects may be replaced by their concentrations is justifiable. Nevertheless, it is more complete conceptually to use, whenever possible, the activities of the defects rather than their concentrations.

The third assumption is that the system is dilute and the point defects do not interact and hence the cross terms in the Onsager phenomenological equations [10] are zero. This assumption is perhaps the hardest to justify. Moreover, the operating conditions of an

SOFC may drive the defect concentration at some locations well beyond the dilute limit. The real reason for this assumption is that there is not enough experimental information to conclusively verify the mechanics and magnitude of possible defect-defect interaction. Therefore, any attempt at modeling this behaviour retains an uncomfortably large degree of speculation. Nonetheless, an attempt is made to model this behaviour in Chapter 2 (in a case study of ceria). Elsewhere the phenomenon is neglected. Some solace may be had in knowing that many other researchers make that assumption too; however, that doesn't minimize the potential impact on the results of the models.

1.5 Summary

In this chapter, the definition, history, and importance of charge-conducting ceramics were briefly discussed to give a summarized context for MIECs. This was followed by a discussion of applications and issues specific to the development of MIECs that provide the rationale and motivation for this study. Finally, to provide the framework for the models developed in later chapters, the general assumptions used in modeling the performance and properties of MIECs were examined. Of the many issues driving research on MIECs, the following chapters focus mainly on understanding the characteristics of the defect population and how it affects the properties and performance of the MIEC.

CHAPTER 2
THE THERMODYNAMICS OF OXIDE MIXED IONIC-ELECTRONIC CONDUCTORS

2.1 Introduction

In this chapter, models are developed for the functional dependence of defect concentration on oxygen partial pressure, P_{O_2}, in MIECs. First, previous attempts by other researchers [11 - 22] are reviewed then a new model is developed. Next, to demonstrate the model's performance a case study is presented for the MIEC, ceria. The model presented here is restricted to MIECs with either the fluorite (general chemical formula AO_2) or the perovskite structure (general chemical formula ABO_3 where A and B are trivalent[2]) shown in Figure 2-1. This restriction is appropriate in this context because all known MIECs of interest (those described in Chapter 1) have one of these structures or else a distorted variant.

Suitable equations for the functional dependence of the concentration of defects as a function of P_{O_2} have thus far been elusive for one reason, high-order polynomials. The usual method of solving the system of defect equations and the charge neutrality equation for the material generates fourth-order or higher polynomials. However, the roots of polynomials of orders greater than four (i.e., quintic or higher) are rather difficult to find. This is a long appreciated point and was recently discussed by Porat and Tuller [11] in relation to oxygen vacancy conducting MIECs and, more recently, Poulsen [12, 13] in relation to proton conducting MIECs. Nevertheless, with reasonable simplifications, the system of defect equations may be reduced so that they generate cubic equations. When

---

[2] This requirement is imposed solely because these types of perovskites are of chief technical interest. Moreover, including other perovskite structures would make the chapter inordinately long. The principles employed in developing the models are generally applicable to any perovskite structure.
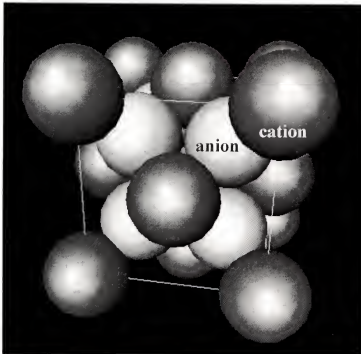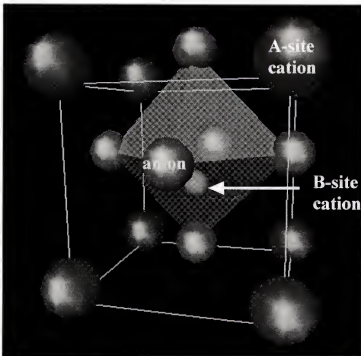
Figure 2-1. Unit cell of (a) the fluorite structure and (b) the perovskite structure.

all the coefficients in the equation are real, cubic equations have at least one real root. However, the roots of such a cubic equation are not useful because they modulate between being real or complex depending on the P_{O_2} value that is being used in the calculation. Hence, any analytical expression so derived would be severely limited to a narrow range of P_{O_2}. This problem has inspired some novel solutions. However, their usefulness is compromised for a variety of reasons (a point discussed briefly in the next section). Consequently, a new approach to determining the functional dependence of the concentration of defects as a function of P_{O_2}, such as the one presented below, is needed.

2.2   Previous Models

2.2.1. Brouwer Approach

One of the earliest, most common and useful approaches was developed by Brouwer [14]. In summary, the Brouwer approach [14] divides the defect equilibria into regions, called Brouwer regimes, where only a pair of oppositely charged defects (e.g., oxygen vacancies and electrons) dominate. The Brouwer approach [14] is successful in that it gives appropriate functional dependences in each limiting case, i.e., Brouwer regime. However, each Brouwer regime has a unique set of formulae for the defects. Hence, the equations are inaccurate and discontinuous near the boundary between two Brouwer regimes because there is no smooth transition from one equation to the other.

The Brouwer approach has been used to obtain [15 - 17] the conductivity expression below:

$$\sigma_{tot} = \sigma_{ion} + \sigma_e + \sigma_h = |z_{ion}|Fu_{ion}c_{ion} + |z_e|Fu_e c_e + |z_h|Fu_h c_h$$
$$= |z_{ion}|Fu_{ion}\alpha + |z_e|Fu_e\beta P_{O_2}^{-\frac{1}{2(|z_i|+|\theta_e|)}} + |z_h|Fu_h\gamma P_{O_2}^{\frac{1}{2(|z_i|+|\theta_h|)}} \qquad (2.2.1)$$

where the subscripts "ion", "e" and "h" refer to ions, electrons and holes respectively; σ is conductivity, z is the charge equivalence number, u is the mobility; c is concentration;

α, β and γ are constants related to the defect reactions and doping levels and F is Faraday's constant. Also, $\theta_{e,h} = z_{e,h}$ if either c_e or $c_h \geq \sim c_{ion}$ and $\theta_{e,h} = 0$ if both c_e and c_h $\ll c_{ion}$ (the electrolytic region).

The discontinuous nature of the equations obtained from the Brouwer approach [14] is evidenced in Eq. (2.2.1) where the exponent, $1/2(|z_i| + |\theta_{e,h}|)$, changes from one region to the other. Additionally, the concentration of ionic defects is assumed to be constant throughout. This assumption is reasonable only in the electrolytic region when both n and $p \ll c_{ion}$. Nevertheless, some ionic conducting oxides, like cubic stabilized zirconia, find useful application primarily in one regime and in such cases the Brouwer approach [14] provides appropriate expressions for the functional dependence of the concentration of defects. However, the range of application for many other materials encompasses more than one Brouwer regime. Therewith, the dependences obtained from the Brouwer approach [14] are not usable.

2.2.2 Oxygen Partial Pressure as a Function of Defect Concentration

In recognition of the inadequacy of the Brouwer [14] approximations to sufficiently describe the concentration of defects that fall in between Brouwer regimes in MIECs, an approach to obtaining an analytical solution to the system of defect equations (described in the next section) describing the defect equilibria of an MIEC was developed in a simplified manner by Porat [18] and Porat and Riess [19]. Subsequently, Spinolo and Anselmi-Tamburini [20] developed the approach into a more general one. Then Porat and Tuller [11] applied the approach to the MIECs $Gd_2(Ti_yZr_{1-y})_2O_7$ and $Ce_yU_{1-y}O_2$ using the equation below:

$$P_{O_2}^{\frac{1}{2}} = \frac{1}{2a} \cdot \left[-b + \left(b^2 - 4ac \right)^{\frac{1}{2}} \right] \tag{2.2.2}$$

where a, b and c are functions of the defect equilibrium constants and defect

concentrations. Equation (2.2.2) relates the external conditions (i.e., the P_{O_2}) to the concentration of defects in an oxide but it expresses the P_{O_2} as a function of the defect concentration. However, description of pertinent phenomena, such as defect conductivity and flux, requires expressions for the defect concentration as a function of P_{O_2} instead. Unfortunately, there is no readily apparent way of extracting an inverse function from Eq. (2.2.2) for defect concentration as a function of P_{O_2}, without oversimplification.

Van Hassel *et al.* [21], in modeling oxygen permeation in perovskites, also obtained expressions for the dependence of P_{O_2} on defect concentration with a slightly different approach.

2.2.3 Numerical Methods

Since the advent of powerful computing power in a desktop package, numerical modeling has become increasingly popular. In principle, the only requirements for numerical modeling are an accurate description of the system in consideration and computing power. Nevertheless, while the results of numerical modeling can yield tremendous quantities of data it may be argued that analytical expressions give more insight and are inherently more tractable and, ultimately, more useful. The viability of numerical and analytical modeling both depend on how accurately the system being modeled is described. Unlike analytical modeling, however, numerical modeling relies on the quality of the algorithm(s) employed. Moreover, different algorithms often return different results. Nevertheless, Poulsen [12, 13] and Bonanos and Poulsen [22] recently developed useful numerical models for defect generation and conductivity dependence on P_{O_2} in doped $LaMnO_3$ [12], $SrCeO_3$ [13] and $BaCeO_3$ [22]. Numerical models, however, are often limited in comparison to analytical models in terms of the insight each method furnishes. Moreover, the results of numerical models are often only as good as the algorithm used to generate them. Thus, the program has the potential to (often covertly) adulterate the science.

2.3   Defect Generation

2.3.1 Defect Equations and Charge Neutrality

Using Kröger-Vink notation, the defect equations governing fluorite and perovskite MIECs are given below. The first three equations apply generally to all MIECs while the rest are categorized for the fluorite and the perovskite structure. Additionally, because a dilute solution is assumed, the activity of the host sublattice is assumed to be unity. All the K's are equilibrium (mass action) constants for the adjacent reactions.

Electron-Hole Pair Formation. Electron-hole pairs are thermally generated in MIECs and their formation is given by:

$$null \rightarrow e' + h^{\bullet} \qquad \Rightarrow \qquad K_i = c_{e'} c_{h} = N_v N_c \exp\left(-\frac{E_g}{k_B T}\right) \qquad (2.3.1)$$

where N_v and N_c are the density of states per unit volume in the valence and conduction bands respectively, E_g is the band gap energy, k_B is Boltzmann's constant and T is temperature.

External Equilibria[3]. The MIECs equilibrium with the gas phase occurs by exchange of oxygen between the crystal lattice and the gas as depicted in Figure 2-2. How this exchange is conducted depends on the relative magnitudes of the equilibrium constants and the ambient P_{O_2}. The equilibrium equations are written here for *Low, Intermediate* and *High* P_{O_2} because the forms given are most appropriate for those P_{O_2} ranges. They are not independent expressions, however, and are connected to each other through electron-hole formation (Eq. (2.3.1)) or internal disorder (Eqs. (2.3.7) through (2.3.9)). This is discussed in greater detail in section 2.3.2.

---

[3] External equilibria for the cation sublattice is ignored because they are thermodynamically unfavorable under normal operating conditions.
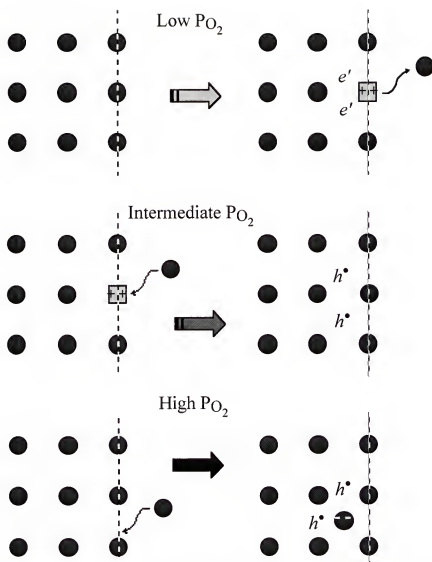
Figure 2-2. Reactions between the oxygen sublattice of an oxide MIEC (fluorite structure) and an external gas phase in the P_{O_2} regions outlined in the text.

Low P_{O_2}:

$$O_O^\times \leftrightarrow V_O^{\bullet\bullet} + 2e' + \tfrac{1}{2}O_2 \qquad \Rightarrow \qquad K_r = c_{V_O} c_e^2 P^{\frac{1}{2}} \qquad (2.3.2)$$

where c_{V_O} is the concentration of oxygen vacancies in the oxygen sublattice[4] and P is the oxygen partial pressure.

---

[4] The usual assumption is made that the concentration of oxygen atoms remains approximately constant.

Intermediate P_{O_2}:

$$V_O^{\bullet\bullet} + \tfrac{1}{2}O_2 \leftrightarrow O_O^{\times} + 2h^{\bullet} \qquad \Rightarrow \qquad K_m = \frac{c_h^2}{c_{V_O}}P^{-\frac{1}{2}} \qquad (2.3.3)$$

High P_{O_2}:[5]

Fluorites:

$$\tfrac{1}{2}O_2 \leftrightarrow O_i'' + 2h^{\bullet} \qquad \Rightarrow \qquad K_h = c_{O_i}c_h^2 P^{-\frac{1}{2}} \qquad (2.3.4)$$
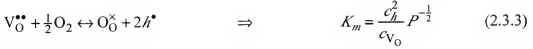
where c_{O_i} is the concentration of oxygen atoms in interstitial sites.

Perovskites: (i) A-site compensation

$$\tfrac{3}{4}O_2 \leftrightarrow \tfrac{3}{2}O_O^{\times} + V_A''' + 3h^{\bullet} \qquad \Rightarrow \qquad K_{h_A} = c_{V_A}c_h^3 P^{-\frac{3}{4}} \qquad (2.3.5)$$

where c_{V_A} is the concentration of metal vacancies on A sites in that metal sublattice.

Perovskites: (ii) B-site compensation

$$\tfrac{3}{4}O_2 \leftrightarrow \tfrac{3}{2}O_O^{\times} + V_B''' + 3h^{\bullet} \qquad \Rightarrow \qquad K_{h_B} = c_{V_B}c_h^3 P^{-\frac{3}{4}} \qquad (2.3.6)$$

where c_{V_B} is the concentration of metal vacancies on B sites in that metal sublattice.

Perovskites: (iii) Combination of A-site and B-site compensation

$$\tfrac{3}{2}O_2 \leftrightarrow 3O_O^{\times} + V_A''' + V_B''' + 6h^{\bullet} \qquad \Rightarrow \qquad K_h = K_{h_A}K_{h_B} = c_{V_A}c_{V_B}c_h^6 P^{-\frac{3}{2}} \quad (2.3.7)$$

---
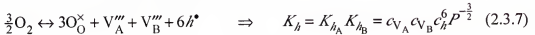
[5] The oxygen incorporation mechanism at high P_{O_2} (oxygen excess) is generally different for fluorites and perovskites. Fluorites generally incorporate excess oxygen in interstitial sites. Conversely, perovskites incorporate excess oxygen by extending their lattice and forming cation vacancies.

Internal Disorder. Anti-Frenkel disorder, whereby an oxygen atom migrates from its site on the lattice to an interstitial site leaving behind a vacancy, is the primary type of internal disorder found in fluorites. Hence, other types of internal disorder are ignored for fluorites. Similarly, Schottky disorder, whereby a pair of metal and oxygen atoms each migrate from their normal sublattices to another location—usually outside the initial lattice boundaries—leaving behind a pair of vacancies, is the dominant type of internal disorder found in perovskites and is the only one treated below.

Fluorites: Anti-Frenkel disorder

$$O_O^\times \leftrightarrow V_O^{\bullet\bullet} + O_i'' \qquad \Rightarrow \qquad K_f = c_{V_O} c_{O_i} \qquad (2.3.8)$$

Perovskites: (i) Schottky disorder on the A-site

$$null \leftrightarrow 2V_A''' + 3V_O^{\bullet\bullet} \qquad \Rightarrow \qquad K_{s_A} = c_{V_O}^3 c_{V_A}^2 \qquad (2.3.9)$$

Perovskites: (ii) Schottky disorder on the B-site

$$null \leftrightarrow 2V_B''' + 3V_O^{\bullet\bullet} \qquad \Rightarrow \qquad K_{s_B} = c_{V_O}^3 c_{V_B}^2 \qquad (2.3.10)$$

Perovskites: (iii) General Schottky disorder

$$null \leftrightarrow V_A''' + V_B''' + 3V_O^{\bullet\bullet} \qquad \Rightarrow \qquad K_s = c_{V_O}^3 c_{V_A} c_{V_B} \qquad (2.3.11)$$

Doping. Only fixed-valence-acceptor doping is considered for the fluorite MIECs because it is predominant in MIECs used for the applications described in Chapter 1. Donor doping, while possible, produces ionic species that have low mobility or are structurally unsuitable (e.g., oxygen interstitials and metal vacancies). For similar reasons, only A-site doping with fixed-valence-acceptor dopants and B-site doping with

multivalent cations—where A and B are trivalent[2]—are presented for perovskite MIECs. It is important to note however, that the multivalent dopant is chosen so that at least one of its valence states coincides with that of the B-site host. Consequently, its incorporation does not require compensation with another defect in that oxidation state.

Fluorites: Fixed-valence-acceptor doping

$$M_2O_3 \xrightarrow{AO_2} 2M'_A + V_O^{\bullet\bullet} + 3O_O^{\times} \qquad (2.3.12)$$
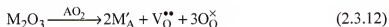
Perovskites: (i) Fixed-valence-acceptor doping on the A-site

$$MO \xrightarrow{ABO_3} M'_A + 2V_O^{\bullet\bullet} + 3e' + O_O^{\times} \qquad (2.3.13)$$

or

$$MO \xrightarrow{ABO_3} M'_A + 2V_O^{\bullet\bullet} + V'''_B + O_O^{\times} \qquad (2.3.14)$$
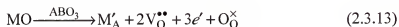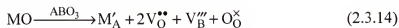
Perovskites: (ii) Doping with an isovalent cation on the B-site

$$AMO_3 \xrightarrow{ABO_3} A_A^{\times} + M_B^{\times} + 3O_O^{\times} \qquad (2.3.15)$$
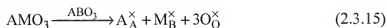
Typical dopant concentrations in common MIECs are given in Table 2-1.

Small Polaron Formation. A polaron is a defect in an ionic crystal that is formed when an excess of charge at a point polarizes or distorts the lattice in its immediate vicinity [23, 24]. For example, if a cation captures an electron the cations surrounding it are attracted to the defect and move towards it, whereas the anions move away. This polarization essentially traps or slows down the electronic defect at it moves through the lattice. When small polarons are formed, the conduction mechanism involves the

Table 2-1. Typical dopant concentrations and unit cell volumes in common oxide mixed ionic-electronic conductors

	Material composition	Structure	Unit cell volume (Å^3)	Dopant concentration, c_A (10^{27} x atoms/m^3)
Fluorites	$Ce_{0.8}Sm_{0.2}O_{1.9}$	cubic	160.99	5
	$Zr_{0.8}Y_{0.2}O_{1.9}$	cubic		
	$Bi_{0.8}Er_{0.2}O_{1.5}$	cubic	181.27	$22^{\dagger}$
Perovskites	$Sr_{0.9}La_{0.1}Co_{0.5}Fe_{0.5}O_{3-\delta}$	cubic	59.06	
	$La_{0.6}Sr_{0.4}Co_{0.2}Fe_{0.8}O_{3-\delta}$	rhombohedral	349.1	

† See Appendix C.

"hopping" of electronic defects between adjacent ions of usually, but not necessarily, the same type but with varying oxidation states. Because of the ease by which transition-metal cations can vary in oxidation states, this type of conduction is most often observed in oxides containing transition-metal cations. Polarization of the lattice results in a reduction of the energy of the system, and the carrier is then assumed to be localized in a potential energy well. It follows that for migration to occur, the carrier has to be supplied with enough (thermal) energy to escape the well and, consequently, the mobility becomes thermally activated. Discussions on large polarons may be found in works by Barsoum [23] and Madelung [24].

Some cations in MIECs are able to accommodate or *trap* an electron liberated from its valence band by localizing the electron in its potential well to form small polarons as described above. These electrons play an important role in conduction because they can *hop* from one cation to the other under the influence of an electric field. Sometimes, for convenience, the formation of a small polaron is treated like chemical reaction—with an associated equilibrium constant. While useful, this treatment may be misleading because, as Madelung [24] points out, the formation (not migration) of the small polarons is not dependent on thermal energy. Nevertheless, it is used here because it harmonizes with the

treatment of the other defect equations. The correct treatment of small polaron formation is discussed in Appendix A, however, presently, the approach given below suffices.

(i) For $c_h \ll c_e$

$$M^\times_{cat} + e' \leftrightarrow M'_{cat} \qquad \Rightarrow \qquad K_- = \frac{c_{sp-}}{c_e c_{cat^\circ}} \qquad (2.3.16)$$

where $M^\times_{cat}$ is a metal ion sitting on a cation site[6] and M'_{cat} is a small polaron consisting of an electron *trapped* on a cation; c_{sp-} and c_{cat° are the concentration of *negatively charged* small polarons and the *uncharged* (i.e., relative to the cation site) cations respectively.

(ii) For $c_e \ll c_h$

$$M^\times_{cat} + h^\bullet \leftrightarrow M^\bullet_{cat} \qquad \Rightarrow \qquad K_+ = \frac{c_{sp+}}{c_h c_{cat^\circ}} \qquad (2.3.17)$$

where $M^\bullet_{cat}$ is a small polaron consisting of a hole *trapped* on a cation and c_{sp+} is the concentration of *positively charged* small polarons.

(iii) For $c_h \sim c_e$ (i.e., general case), in the absence of electron-hole recombination,

$$2M^\times_{cat} + h^\bullet + e' \leftrightarrow M^\bullet_{cat} + M'_{cat} \qquad \Rightarrow \qquad K_{sp} = K_- K_+ K_i = \frac{c_{sp-} c_{sp+}}{c_{cat^\circ}^2} \qquad (2.3.18)$$

Mass Balance. Since some of the cations participate in forming small polarons, they are consequently distributed between two valence states. Hence, a *mass balance* equation must be invoked to fulfill the requirement of conservation of the number of cations (i.e., to keep track of the cations).

---

[6] In typical perovskites, small polarons are formed almost exclusively on B-site cations.

$$c_{cat^o} + c_{sp-} + c_{sp+} = c_{cat} \qquad (2.3.19)$$

where c_{cat} is the total concentration of all (*charged* and *uncharged*) cations.

Charge Balance. As discussed in Chapter 1 (see Eq. (1.1)), MIECs are assumed to be electrically neutral. Accordingly, a charge balance equation may be written for each MIEC family as follows:

Fluorites:

$$c_e + c_A + 2c_{O_i} = 2c_{V_O} + c_h \qquad (2.3.20)$$

where c_A is the concentration of the acceptor dopant (M'_A).

Perovskites:

$$c_e + c_A + 3c_{V_{A/B}} = 2c_{V_O} + c_h \qquad (2.3.21)$$

where $c_{V_{A/B}}$ is the total concentration of A-site and B-site cation vacancies.

A summary of all the defect equations and charge balances is given in Table 2-2 for easy reference.

2.3.2 Relationships among Equilibrium Constants

The defect equations are not all independent and a number of useful relationships between the various defect species in the system of defect equations may be generated. These relationships serve three purposes. Firstly, they reduce the number of equilibrium constants to be determined experimentally. This is very advantageous from an experimental and practical standpoint because obtaining values for the equilibrium constants are quite difficult. In addition, they serve as a helpful check for consistency by

Table 2-2. Summary of defect equations for fluorites and perovskites

	Fluorites	Perovskites
e'-$h\bullet$ Formation	$K_i = c_e c_h$	
External Equilibria		
Low P_{O_2}	$K_r = c_{V_O} c_e^2 P^{\frac{1}{2}}$	
Intermediate P_{O_2}	$K_m = c_{V_O}^{-1} c_h^2 P^{-\frac{1}{2}}$	
High P_{O_2}	$K_h = c_{O_i} c_h^2 P^{-\frac{1}{2}}$	$K_{h_A} = c_{V_A} c_h^3 P^{-\frac{3}{4}}$
		$K_{h_B} = c_{V_B} c_h^3 P^{-\frac{3}{4}}$
		$K_h = c_{V_A} c_{V_B} c_h^6 P^{-\frac{3}{2}}$
Internal Disorder	$K_f = c_{V_O} c_{O_i}$	$K_{s_A} = c_{V_O}^3 c_{V_A}^2$
		$K_{s_B} = c_{V_O}^3 c_{V_B}^2$
		$K_s = c_{V_O}^3 c_{V_A} c_{V_B}$
Doping	$M_2O_3 \xrightarrow{AO_2} 2M'_A + V_O^{\bullet\bullet} + 3O_O^{\times}$	$2MO \xrightarrow{ABO_3} 2M'_A + V_O^{\bullet\bullet} + 2O_O^{\times}$
		$MO \xrightarrow{ABO_3} M'_A + h^{\bullet} + O_O^{\times}$
		$AMO_3 \xrightarrow{ABO_3} A_A^{\times} + M_B^{\times} + 3O_O^{\times}$
Small Polarons		
$c_h \ll c_e$	$K_- = c_{sp-} c_e^{-1} c_{cat}^{-1}$	
$c_e \ll c_h$	$K_+ = c_{sp+} c_h^{-1} c_{cat}^{-1}$	
General	$K_{sp} = K_- K_+ K_i = c_{sp-} c_{sp+} c_{cat}^{-2}$	
Mass Balance	$c_{cat} + c_{sp-} + c_{sp+} = c_{cat}$	
Charge Balance	$c_e + c_A + 2c_{O_i} = 2c_{V_O} + c_h$	$c_e + c_A + 3c_{V_{A/B}} = 2c_{V_O} + c_h$

limiting the arbitrariness by which values can be assigned to the constants in mathematical models. Finally, they illustrate the interdependence of the defect equations (and equilibrium constant) and, in so doing, add some physical insight into the mechanics of defect formation. Finally, these relationships also help to simplify some of the equations derived later on.

Multiplying the mass action expressions in Eq. (2.3.2) (low P_{O_2}) and Eq. (2.3.3) (intermediate P_{O_2}) yields Eq. (2.3.1), i.e.,

$$K_m K_r = K_i^2 \qquad (2.3.22)$$

This equation shows that a knowledge of two of the equilibrium constants allows the calculation of a third. Moreover, the relationship implies that the rate of the external reactions given in Eqs. (2.3.2) and (2.3.3) is limited by the ability of the MIEC to produce electronic species. Hence, MIECs with high K_i readily incorporate oxygen atoms (high K_m) or vacancies (high K_r) into their lattices. This has relevance in choice of MIEC as an anode (high K_r), cathode (high K_m) or electrolyte (low K_i). For anodes, which operate on the fuel/reducing side (low P_{O_2}) of a solid oxide fuel cell (SOFC) or electrocatalytic reactor, an ability to incorporate oxygen vacancies (release oxygen atoms) readily is desired. Hence, one would choose an MIEC with a high K_r. Conversely, for cathodes, which operate on the air/oxidizing side (high P_{O_2}) of a SOFC or electrocatalytic reactor, an ability to incorporate oxygen atoms readily is desired and an MIEC with a large K_m should be chosen. For efficient operation, SOFCs and electrocatalytic reactors require an electrolyte that is predominantly ionic, hence an MIEC with a low K_i would be suitable. While this doesn't represent ground breaking research, it does demonstrate how the choice of a material could be driven by knowledge rather than trial and error.

The principle is repeated when dividing Eq. (2.3.4) by Eq. (2.3.3) which yields Eq. (2.3.7), i.e.,

$$K_h = K_f K_m = K_f K_i^2 K_r^{-1} \qquad (2.3.23)$$

This equation shows that the ability of an MIEC to incorporate oxygen interstitials and vacancies, is determined by its capacity to generate electron-hole pairs and support anti-Frenkel disorder (oxygen vacancy-interstitial pairs).

Similarly, dividing the square of Eqs. (2.3.5) through (2.3.7) by the cube of Eq. (2.3.3) yields Eq. (2.3.9) through (2.3.11), i.e.,

$$K_h^2 = K_s K_m^3 = K_s K_i^6 K_r^{-3} \qquad (2.3.24)$$

Eq. (2.3.24) is analogous to Eq. (2.3.23) and yields the same information but, in this case, for perovskites. Finally, Eq. (2.3.5) divided by Eq. (2.3.6) is equal to Eq. (2.3.9) divided by Eq. (2.3.10), i.e.,

$$\frac{K_{h_A}}{K_{h_B}} = \frac{K_{s_A}}{K_{s_B}} \qquad (2.3.25)$$

Like Eq. (2.3.24), this relationship shows that the external disorder is related to the internal disorder, but it also shows that the site possessing greater internal disorder (larger K_s) is also more reactive at the interface (larger K_h).

2.3.3 Relationships between Small Polaron Concentrations

In this section, the relationships between small polarons, host cations and electronic (electrons and holes) carriers are investigated first. Then the relationship between negatively and positively charged small polarons is probed. All relations developed in this section apply to both fluorites and perovskites.

For $c_h \ll c_e$ (and therefore $c_{sp^+} \ll c_{sp^-}$) Eq. (2.3.19) reduces to:

$$c_{cat^\circ} + c_{sp-} \approx c_{cat} \qquad (2.3.26)$$

Therefore, combining Eqs. (2.3.16) and (2.3.26) and $K_- = K_+ = 1/c_{cat}$ (see Appendix A for further details) for $c_h \ll c_e$ yields:

$$c_{sp-} \approx \frac{c_e}{1 + c_e K_-} = \frac{c_e c_{cat}}{c_e + c_{cat}} \tag{2.3.27}$$

Likewise, for $c_e \ll c_h$ (and therefore $c_{sp-} \ll c_{sp+}$) Eq. (2.3.19) reduces to:

$$c_{cat^o} + c_{sp+} \approx c_{cat} \tag{2.3.28}$$

Therefore, combining Eqs. (2.3.17) and (2.3.28) and $K_- = K_+ = 1/c_{cat}$ (see Appendix A) for $c_e \ll c_h$ yields:

$$c_{sp+} = \frac{c_h}{1 + c_h K_+} = \frac{c_h c_{cat}}{c_h + c_{cat}} \tag{2.3.29}$$

Eqs. (2.3.27) and (2.3.29) show that the concentration of small polarons depends on the total number of available sites and the number of electrons or holes. Though readily apparent, this is not a trivial point because Eqs. (2.3.27) and (2.3.29) also show that at large c_e or c_h, $c_{sp-} \approx c_{cat}$ or $c_{sp+} \approx c_{cat}$ respectively. This implies that there is a limit to the number of small polarons formed. The mechanism of electronic conduction has long been assumed to be small polaron "hopping" [25, 26]. However, when the concentration of electronic carriers approaches the concentration *host* sites (i.e., when $c_e \geq \sim c_{cat}$ or $c_h \geq \sim c_{cat}$), excess electrons and holes become *itinerant* (i.e., not localized) in nature. It is essential to determine the role of these *itinerant* electrons and holes. Do they participate in conduction by an alternate ("non-hopping") mechanism? Do they play a role in the formation of defect associates? The first question is beyond the scope and focus of this work. However, an attempt is made to address the latter question in the case study on ceria in section 2.4.

To explore the relationship between negatively and positively charged small polarons, Eqs. (2.3.18) may be substituted into Eqs. (2.3.19) to eliminate c_{cat}°—given $K_- = K_+ = 1/c_{cat}$ (see Appendix A)—with the result

$$c_{sp+} c_{sp-} c_{cat}^2 = \left(c_{cat} - c_{sp-} - c_{sp+} \right)^2 K_i \qquad (2.3.30)$$

Eq. (2.3.30) is a quadratic equation whose only meaningful solution is:

$$c_{sp+} = c_{cat} - \left(1 - \frac{c_{cat}^2}{2 K_i} \right) c_{sp-} + \frac{c_{cat}^2}{2 K_i} \sqrt{ \left(1 - \frac{4 K_i}{c_{cat}^2} \right) c_{sp-}^2 + \frac{4 K_i}{c_{cat}} c_{sp-} } \qquad (2.3.31a)$$

if c_{sp+} is the dependent variable, or

$$c_{sp-} = c_{cat} - \left(1 - \frac{c_{cat}^2}{2 K_i} \right) c_{sp+} + \frac{c_{cat}^2}{2 K_i} \sqrt{ \left(1 - \frac{4 K_i}{c_{cat}^2} \right) c_{sp+}^2 + \frac{4 K_i}{c_{cat}} c_{sp-} } \qquad (2.3.31b)$$

if c_{sp-} is the dependent variable. These formulae relate c_{sp-} to c_{sp+} and is potentially more useful than either Eqs. (2.3.19) or (2.3.30) since they contain only one variable. Additionally, since the term under the square root in each case must be ≥ 0 to obtain real and meaningful values for c_{sp-} and c_{sp+}, then

$$c_{sp-} \geq \frac{c_{cat}}{1 - \frac{1}{4} c_{cat}^2 K_i^{-1}}$$

and

$$c_{sp+} \geq \frac{c_{cat}}{1 - \frac{1}{4} c_{cat}^2 K_i^{-1}}$$

These inequalities serve as lower limits for c_{sp-} and c_{sp+}. Moreover, they show that for large K_i (i.e., for $4K_i \gg c_{cat}^2$) the concentration of small polarons will be larger than c_{cat}. As discussed earlier, this isn't physically possible. Hence the real importance of this result is that it further reinforces the need to account for the effect and behaviour of the extra, *itinerant*, electronic charge carriers.

Finally, since the number of small polarons formed is limited to the total number of available and amenable cations, then to account for cases where $c_e \geq c_{cat}$ or $c_h \geq c_{cat}$, the following relationships are defined:

$$c_e = c_{e>} + c_{sp-} \qquad (2.3.32)$$

and

$$c_h = c_{h>} + c_{sp+} \qquad (2.3.33)$$

where $c_{e>}$ and $c_{h>}$ are the concentration of *itinerant* electrons and holes respectively. Thus, when $c_{e>} \ll c_{sp-}$ or $c_{h>} \ll c_{sp+}$ (i.e., $c_e \ll c_{cat}$ or $c_h \ll c_{cat}$) $c_e \approx c_{sp-}$ and $c_h \approx c_{sp+}$ (i.e., all the electronic defects exist as small polarons).

2.3.4 Modeling the Functional Dependence of Defect Concentration on P_{O_2}

Now that the defect equations have been summarized for fluorite and perovskite MIECs, they can be put to use to obtain the functional dependence of defect concentrations on P_{O_2}. As mentioned in the introduction to this chapter, the traditional method of solving the system of defect equations and the charge balance equation yields analytically unsolvable polynomial equations, hence the need to model the system instead. In this section, models are developed for the functional dependence of defect concentrations on oxygen partial pressure in the three P_{O_2} regimes defined in Eqs. (2.3.2) through (2.3.6). The expressions are subsequently combined to yield a general expression

for each defect that spans the entire P_{O_2} range. Additionally, because they are the most important, only three of the defect species, $V_O^{\bullet\bullet}$, e' and $h^\bullet$, are featured in deriving the models. The other defect species are not ignored, however, since their functionality may be obtained from the other through the defect equations.

Low (reducing) P_{O_2}. The first region to be considered is *low* P_{O_2}, where

$$c_{O_i}, c_{V_{A/B}} \ll c_e, c_A$$

and

$$c_h \ll c_{V_O}$$

Therefore, in this region the charge balances for fluorites—Eq. (2.3.20)—and perovskites—Eq. (2.3.21)—both reduce to:

$$c_e + c_A = 2c_{V_O} \tag{2.3.34}$$

Combining Eqs. (2.3.2) and (2.3.34) yields:

$$K_r^{\frac{1}{2}} c_{V_O}^{-\frac{1}{2}} P^{-\frac{1}{4}} + c_A = 2c_{V_O} \tag{2.3.35}$$

which when differentiated with respect to c_{V_O}—noting that $dK_r/dc_{V_O} = 0$ since K_r and all the other equilibrium constants are functions of temperature only—gives:

$$-\frac{dP}{dc_{V_O}} = 8c_{V_O}^{\frac{1}{2}} K_r^{-\frac{1}{2}} P^{\frac{5}{4}} + 2\frac{P}{c_{V_O}} \tag{2.3.36a}$$

For $K_r \ll 16c_{V_O}^3 P^{\frac{1}{2}}$—i.e., $8c_{V_O}^{\frac{1}{2}} K_r^{-\frac{1}{2}} P^{\frac{5}{4}} \gg 2Pc_{V_O}^{-1}$—Eq. (2.3.36a) reduces to:

$$\frac{dP}{dc_{V_O}} \approx -8c_{V_O}^{\frac{1}{2}} K_r^{-\frac{1}{2}} P^{\frac{5}{4}} \tag{2.3.36b}$$

In the *low* P_{O_2} region typically $2c_{V_O} \geq c_A$ and $c_A \sim 10^{27}$ m^{-3}. However, since c_{V_O} and P are both variables, the validity of the simplification may be assessed for a given c_{V_O} and P. An example of such an assessment is given later, in the case study on ceria.

Eqs. (2.3.2) and (2.3.34) show that (in the *low* P_{O_2} region) as $P \rightarrow 0$

$$2c_{V_O} = c_e \qquad \text{and} \qquad c_{V_O}, c_e \gg c_A$$

Conversely, as $P \rightarrow \infty$

$$2c_{V_O} = c_A \qquad \text{and} \qquad c_{V_O}, c_A \gg c_e$$

where "$P \rightarrow \infty$" corresponds to P approaching the upper limit of the *low* P_{O_2} region. The lower limit (boundary) for c_{V_O} may be incorporated as a boundary condition for Eq. (2.3.36b) and the first-order separable differential equation may be solved by integration

$$K_r^{\frac{1}{2}} \int_{\infty}^{P} P^{-\frac{5}{4}} \cdot dP = -8 \int_{\frac{1}{2}c_A}^{c_{V_O}} c_{V_O}^{\frac{1}{2}} \cdot dc_{V_O}$$

with the result

$$c_{V_O}(P) = \left[\frac{3}{4} K_r^{\frac{1}{2}} P^{-\frac{1}{4}} + \left(\frac{1}{2} c_A \right)^{\frac{3}{2}} \right]^{\frac{2}{3}} \tag{2.3.37}$$

Substituting this expression for $c_V(P)$ into Eq. (2.3.2) yields:

$$c_e(P) = K_r^{\frac{1}{2}} P^{-\frac{1}{4}} \left[\frac{3}{4} K_r^{\frac{1}{2}} P^{-\frac{1}{4}} + \left(\frac{1}{2} c_A \right)^{\frac{3}{2}} \right]^{-\frac{1}{3}} \tag{2.3.38}$$

and substituting Eqs. (2.3.22) and (2.3.38) into Eq. (2.3.1) gives:

$$c_h(P) = K_m^{\frac{1}{2}} P^{\frac{1}{4}} \left[\frac{3}{4} K_r^{\frac{1}{2}} P^{-\frac{1}{4}} + \left(\frac{1}{2} c_A \right)^{\frac{3}{2}} \right]^{\frac{1}{3}} \qquad (2.3.39)$$

Similarly, relations for the other defects (c_{O_i}, $c_{V_{A/B}}$), in the *low* P_{O_2} region, may be obtained by appropriately substituting one or a combination of Eqs. (2.3.37) through (2.3.39) into Eqs. (2.3.4) through (2.3.11). These relations are given in Appendix B.

Intermediate P_{O_2}. The next region under consideration is *intermediate* P_{O_2}, where

$$c_{O_i}, c_{V_{A/B}}, c_e \ll c_A$$

In other words, the level of doping is sufficiently high that c_{O_i}, $c_{V_{A/B}}$ and c_e are suppressed in this P_{O_2} region. Again, this is typical of MIECs used in the applications discussed in Chapter 1. In these conditions, the charge balances for fluorites—Eq. (2.3.20)—and perovskites—Eq. (2.3.21)—both reduce to:

$$c_A = 2c_{V_O} + c_h \qquad (2.3.40)$$

Eqs. (2.3.3) and (2.3.40) may be combined directly (eliminating c_{V_O}) to produce a quadratic equation in terms of c_h

$$K_m \left(c_A - c_h \right) P^{\frac{1}{2}} = 2c_h^2$$

whose only meaningful solution is:

$$c_h(P) = \frac{1}{4} \left(\sqrt{8 c_A K_m P^{\frac{1}{2}} + K_m^2 P} - K_m P^{\frac{1}{2}} \right) \qquad (2.3.41)$$

which, when combined with Eqs. (2.3.1), (2.3.2) and (2.3.22), yields:

$$c_e(P) = 4 K_r^{\frac{1}{2}} \left(\sqrt{8 c_A P^{\frac{1}{2}} + K_m P} - K_m^{\frac{1}{2}} P^{\frac{1}{2}} \right)^{-1} \tag{2.3.42}$$

and

$$c_{V_O}(P) = \frac{1}{16} \left[\sqrt{K_m P^{\frac{1}{2}} + 8 c_A} - K_m^{\frac{1}{2}} P^{\frac{1}{4}} \right]^2 \tag{2.3.43}$$

Again, relations for the other defects (c_{O_i}, $c_{V_{A/B}}$), in the *intermediate* P_{O_2} region, may be obtained by appropriately substituting one or a combination of Eqs. (2.3.41) through (2.3.43) into Eqs. (2.3.4) through (2.3.11)—see Appendix B.

High (Oxidizing) P_{O_2}. The final region to be discussed is *high* P_{O_2}, where

$$c_e \ll c_A, c_{O_i}, c_{V_{A/B}}$$

and

$$c_{V_O} \ll c_h$$

In these conditions the charge balance for fluorites—from Eq. (2.3.20)—reduces to:

$$c_A + 2 c_{O_i} = c_h \tag{2.3.44}$$

Similarly, the charge balance for perovskites—from Eq. (2.3.21)—reduces to:

$$c_A + 3 c_{V_{A/B}} = c_h \tag{2.3.45}$$

In a treatment analogous to that for the *low* P_{O_2} region, Eqs. (2.3.4) and (2.3.44) may be combined, for fluorites, to give:

$$c_A + 2K_h c_h^{-2} P^{\frac{1}{2}} = c_h \qquad (2.3.46)$$

which when differentiated with respect to c_h—noting that $dK_h/dc_h = 0$—gives:

$$\frac{dP}{dc_h} = c_h^2 P^{\frac{1}{2}} K_h^{-1} + \frac{4P}{c_h} \qquad (2.3.47a)$$

For $K_h \ll \frac{1}{4} c_h^3 P^{-\frac{1}{2}}$—i.e., $c_h^2 P^{\frac{1}{2}} K_h^{-1} \gg 4Pc_h^{-1}$—Eq. (2.3.47a) reduces to:

$$\frac{dP}{dc_h} \approx c_h^2 P^{\frac{1}{2}} K_h^{-1} \qquad (2.3.47b)$$

Eqs. (2.3.4) and (2.3.44) show that (in the *high* P_{O_2} region) as $P \to 0$

$$c_h = c_A \qquad \text{and} \qquad c_h, c_A \gg c_{O_i}$$

where "$P \to 0$" corresponds to P approaching the lower limit of the *high* P_{O_2} region. Conversely, as $P \to \infty$

$$c_h = 2c_{O_i} \qquad \text{and} \qquad c_h, c_{O_i} \gg c_A$$

The lower limit (boundary) for c_h may be incorporated as a boundary condition for Eq. (2.3.47b) and the first-order separable differential equation may be solved by integration

$$K_h \int_0^P P^{-\frac{1}{2}} \cdot dP = \int_{c_A}^{c_h} c_h^2 \cdot dc_h$$

with the result

$$c_h(P) = \left(6 K_h P^{\frac{1}{2}} + c_A^3 \right)^{\frac{1}{3}} \tag{2.3.48}$$

which when substituted in Eqs. (2.3.1) and (2.3.3) yields:

$$c_e(P) = K_i \left[6 K_h P^{\frac{1}{2}} + c_A^3 \right]^{-\frac{1}{3}} \tag{2.3.49}$$

and

$$c_{V_O}(P) = K_m^{-1} P^{-\frac{1}{2}} \left[6 K_h P^{\frac{1}{2}} + c_A^3 \right]^{\frac{2}{3}} \tag{2.3.50}$$

Similarly, for perovskites, Eqs. (2.3.5), (2.3.6) and (2.3.45) may be combined with the result:

$$c_A + 3 K_{h^*} c_h^{-3} P^{\frac{3}{4}} = c_h \tag{2.3.51}$$

where

$$K_{h^*} = K_{h_A} + K_{h_B}$$

Differentiating Eq. (2.3.51) with respect to c_h yields:

$$\frac{\mathrm{d}P}{\mathrm{d}c_h} = \frac{4}{9} P^{\frac{1}{4}} c_h^3 K_{h^*}^{-1} + \frac{4P}{c_h} \tag{2.3.52a}$$

For $K_{h^*} << \frac{1}{9} P^{-\frac{3}{4}} c_h^4$ —i.e., $\frac{4}{9} P^{\frac{1}{4}} c_h^3 K_{h^*}^{-1} >> 4 P c_h^{-1}$—Eq. (2.3.52a) reduces to:

$$\frac{\mathrm{d}P}{\mathrm{d}c_h} \approx \frac{4}{9} P^{\frac{1}{4}} c_h^3 K_{h^*}^{-1}$$

(2.3.52b)

Eqs. (2.3.5), (2.3.6) and (2.3.45) show that (in the *high* P_{O_2} region) as $P \to 0$

$$c_h = c_A \qquad \text{and} \qquad c_h, c_A \gg c_{V_{A/B}}$$

where "$P \to 0$" corresponds to P approaching the lower limit of the *high* P_{O_2} region. Conversely, as $P \to \infty$

$$c_h = 3c_{V_{A/B}} \qquad \text{and} \qquad c_h, c_{V_{A/B}} \gg c_A$$

The lower limit (boundary) for p may be incorporated as a boundary condition for Eq. (2.3.47b) and the first-order separable differential equation may be solved by integration

$$9 K_{h^*} \int_0^P P^{-\frac{1}{4}} \cdot \mathrm{d}P = 4 \int_{c_A}^{c_h} c_h^3 \cdot \mathrm{d}c_h$$

with the result

$$c_h(P) = \left(12 K_{h^*} P^{\frac{3}{4}} + c_A^4 \right)^{\frac{1}{4}}$$

(2.3.53)

which when substituted in Eqs. (2.3.1) and (2.3.3) yields:

$$c_e(P) = K_i \left[12 K_{h^*} P^{\frac{3}{4}} + c_A^4 \right]^{-\frac{1}{4}}$$

(2.3.54)

and

$$c_{V_O}(P) = K_m^{-1} P^{-\frac{1}{2}} \left[12 K_{h^*} P^{\frac{3}{4}} + c_A^4 \right]^{\frac{1}{2}} \tag{2.3.55}$$

As before, relations for the other defects (c_{O_i}, $c_{V_{A/B}}$) in the *high* P_{O_2} region—for either the fluorite or the perovskite structure—may be obtained by substituting one or a combination of Eqs. (2.3.48) through (2.3.50) or Eq. (2.3.53) through (2.3.55) into Eqs. (2.3.1) through (2.3.11)—see Appendix B.

2.3.5 Generalized Equations for Defect Concentration Dependence on P_{O_2}

In this section, generalized equations for the functional dependence of defect concentration on P_{O_2} are assembled from the region specific equations derived in the preceding sections. To obtain these general expressions, the representative expressions for each defect, in each region, are *carefully* combined. The challenge here is to avoid errors caused by the convergence of each defect concentration-P_{O_2} equation to identical values at the boundaries between the P_{O_2} regions. As an example, to get $c_{V_O}(P)$ over the complete range of P_{O_2} requires the summation of Eqs. (2.3.37), (2.3.43) and (2.3.50) (or (2.3.55)). However, Eqs. (2.3.37) and (2.3.43) both converge to $c_A/2$ at the boundary between *low* and *intermediate* P_{O_2} regions. Therefore, to avoid duplication, $c_A/2$ must be subtracted from the sum. Similarly, since Eqs. (2.3.43) and (2.3.50) (or (2.3.55)) both converge to $c_A^2 K_m^{-1} P^{-\frac{1}{2}}$ at the boundary between the *intermediate* and *high* P_{O_2} regions, then $c_A^2 K_m^{-1} P^{-\frac{1}{2}}$ must also be subtracted to avoid duplication. This produces for fluorites,

$$c_{V_O} = \left[\left(\frac{\frac{1}{16} K_m}{P^{-\frac{1}{2}}} + \frac{c_A}{2} \right)^{\frac{1}{2}} - \frac{\frac{1}{4} K_m^{\frac{1}{2}}}{P^{-\frac{1}{4}}} \right]^2 + \left[\frac{3 K_f^{\frac{1}{2}}}{4 P^{\frac{1}{4}}} + \left(\frac{c_A}{2} \right)^{\frac{3}{2}} \right]^{\frac{2}{3}} + \frac{\left[\frac{6 K_h}{P^{-\frac{1}{2}}} + c_A^3 \right]^{\frac{2}{3}} - c_A^2}{K_m P^{\frac{1}{2}}} - \frac{c_A}{2} \tag{2.3.56}$$

and for perovskites,

$$c_{V_O} = \left[\left(\frac{1}{16}\frac{K_m}{P^{-\frac{1}{2}}} + \frac{c_A}{2}\right)^{\frac{1}{2}} - \frac{\frac{1}{4}K_m^{\frac{1}{2}}}{P^{-\frac{1}{4}}}\right]^2 + \left[\frac{3K_r^{\frac{1}{2}}}{4P^{\frac{1}{4}}} + \left(\frac{c_A}{2}\right)^{\frac{3}{2}}\right]^{\frac{2}{3}} + \frac{\left(\frac{12K_h}{P^{-\frac{3}{2}}} + c_A^4\right)^{\frac{1}{2}} - c_A^2}{K_m P^{\frac{1}{2}}} - \frac{c_A}{2} \quad (2.3.57)$$

With similar arguments, expressions for all the defects over the complete range of P_{O_2} may be derived, $c_e(P)$ and $c_h(P)$ are given below for fluorites,

$$c_e = \frac{K_r^{\frac{1}{2}} P^{-\frac{1}{4}}}{\left[\frac{3K_r^{\frac{1}{2}}}{4P^{\frac{1}{4}}} + \left(\frac{c_A}{2}\right)^{\frac{3}{2}}\right]^{\frac{1}{3}}} + \frac{4K_r^{\frac{1}{2}}}{\sqrt{\frac{8c_A}{P^{-\frac{1}{2}}} + \frac{K_m}{P^{-1}}} - \frac{K_m^{\frac{1}{2}}}{P^{-\frac{1}{2}}}} + \frac{K_i}{\left(\frac{6K_h}{P^{-\frac{1}{2}}} + c_A^3\right)^{\frac{1}{3}}} - \frac{K_i}{c_A} - \frac{K_r^{\frac{1}{2}}c_A}{2P^{\frac{1}{4}}} \quad (2.3.58)$$

$$c_h = \frac{\left[\frac{3K_r^{\frac{1}{2}}}{4P^{\frac{1}{4}}} + \left(\frac{c_A}{2}\right)^{\frac{3}{2}}\right]^{\frac{1}{3}}}{K_m^{-\frac{1}{2}}P^{-\frac{1}{4}}} + \frac{\sqrt{\frac{c_A K_m}{\frac{1}{8}P^{-\frac{1}{2}}} + \frac{K_m^2}{P^{-1}}} - \frac{K_m}{P^{-\frac{1}{2}}}}{4} + \left(\frac{6K_h}{P^{-\frac{1}{2}}} + c_A^3\right)^{\frac{1}{3}} - c_A - \frac{2P^{\frac{1}{4}}}{K_m^{-\frac{1}{2}}c_A} \quad (2.3.59)$$

and perovskites,

$$c_e = \frac{K_r^{\frac{1}{2}} P^{-\frac{1}{4}}}{\left[\frac{3K_r^{\frac{1}{2}}}{4P^{\frac{1}{4}}} + \left(\frac{c_A}{2}\right)^{\frac{3}{2}}\right]^{\frac{1}{3}}} + \frac{4K_r^{\frac{1}{2}}}{\sqrt{\frac{8c_A}{P^{-\frac{1}{2}}} + \frac{K_m}{P^{-1}}} - \frac{K_m^{\frac{1}{2}}}{P^{-\frac{1}{2}}}} + \frac{K_i}{\left(\frac{12K_h}{P^{-\frac{3}{4}}} + c_A^4\right)^{\frac{1}{4}}} - \frac{K_i}{c_A} - \frac{K_r^{\frac{1}{2}}c_A}{2P^{\frac{1}{4}}} \quad (2.3.60)$$

$$c_h = \frac{\left[\frac{3K_r^{\frac{1}{2}}}{4P^{\frac{1}{4}}} + \left(\frac{c_A}{2}\right)^{\frac{3}{2}}\right]^{\frac{1}{3}}}{K_m^{-\frac{1}{2}}P^{-\frac{1}{4}}} + \sqrt{\frac{c_A K_m}{2P^{-\frac{1}{2}}} + \frac{\frac{1}{16}K_m^2}{P^{-1}}} - \frac{\frac{1}{4}K_m}{P^{-\frac{1}{2}}} + \left(\frac{12K_h}{P^{-\frac{3}{4}}} + c_A^4\right)^{\frac{1}{4}} - c_A - \frac{2P^{\frac{1}{4}}}{K_m^{-\frac{1}{2}}c_A} \quad (2.3.61)$$

As before, relations for the other defects (c_{O_i}, $c_{V_{A/B}}$)—in either the fluorite or the perovskite structure—may be obtained in a similar fashion (see Appendix B).

2.3.6 Results and Discussion

In this section, the expressions derived above for the functional dependence of defect concentration on P_{O_2} are examined. Plots of defect concentration versus P_{O_2} are generated from Eqs. (2.3.56) to (2.3.61) and are compared with the predictions of the Brouwer approach [14].

The physical soundness of Eqs. (2.3.56) through (2.3.61) may be ascertained by examining if $c_{V_O}(P)$, $c_e(P)$ and $c_h(P) > 0$. Regrettably, this is not always the case because Eqs. (2.3.56) through (2.3.61) return negative values of $c_{V_O}(P)$, $c_e(P)$ and $c_h(P)$ when: (a) the values of the mass action constants do not conform to the constraints of Eqs. (2.3.22) through (2.3.25) and (b) at the very low or high P_{O_2}. The first criteria for failure is rather obvious since any violation of the constraints in Eqs. (2.3.22) through (2.3.25) changes the entire system of defect equations on which the model is based. The second criteria is a result of having to subtract shared boundary values to avoid duplication when the equations of each representative P_{O_2} region (*low*, *intermediate* and *high*) is summed—as discussed earlier for the derivation of Eqs. (2.3.56) through (2.3.61). As the number of regions (*low*, *intermediate* or *high*) that are modeled decreases, Eqs. (2.3.56) through (2.3.61) are less likely to produce negative values because the subtractive terms drop out. For example, expressions for any single region (*low*, *intermediate* or *high*) have no singularities at all. Indeed, many MIECs find application only in one or two regions at most and extreme values of P_{O_2} are typically not accessible experimentally. Therefore, this deficiency is minimal for most practical applications.

Figures 2-3 and 2-4 show plots of defect concentration versus P_{O_2}—called defect equilibrium diagrams (DEDs)—for a typical fluorite MIEC (Figure 2-3) and a typical perovskite MIEC (Figure 2-4). The plots may be divided into four regions. In Region I
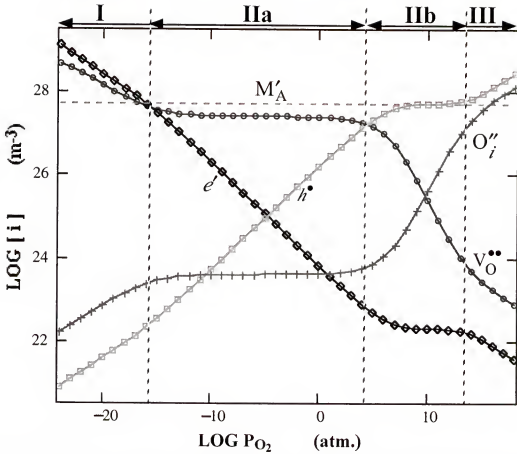
Figure 2-3. Defect concentration dependence on P_{O_2} for a fluorite-structured MIEC ($K_r = 10^{75}$ m^{-9}atm$^{1/2}$, $K_m = 10^{25}$ m^{-3}atm$^{-1/2}$ and $K_h = 10^{76}$ m^{-9}atm$^{-1/2}$).

oxygen vacancies and electrons dominate. In Region III, either oxygen interstitials and electron holes (fluorites) or cation vacancies and electron holes (perovskites) dominate. Between these two regions is Region II, where defect species that are enhanced by the acceptor dopant dominate. This region may further be subdivided into Region IIa where vacancies dominate and Region IIb where electron holes dominate. If the MIEC were donor-doped, Region IIb would be dominated by oxygen interstitials (fluorites) or cation vacancies (perovskites) and Region IIa by electrons.

The width (in terms of P_{O_2}) of Region IIa—called the electrolytic region—is critical to the performance of SOFCs and electrocatalytic reactors. For these applications it is desirable that Region IIa be as wide as possible so that the MIEC is predominantly an
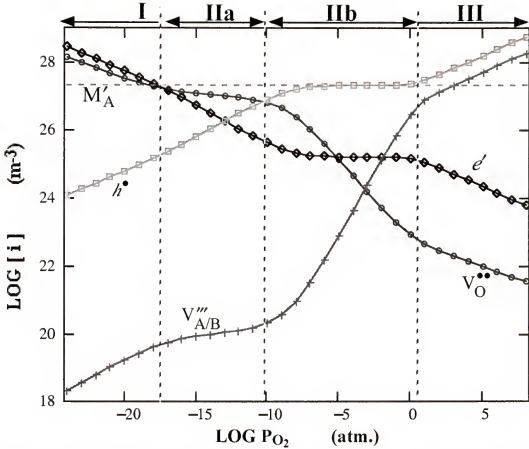
Figure 2-4. Defect concentration dependence on P_{O_2} for a perovskite-structured MIEC ($K_r = 10^{73}$ m^{-9}atm$^{1/2}$, $K_m = 10^{32}$ m^{-3}atm$^{-1/2}$ and $K_h = 10^{109}$ m^{-9}atm$^{-1/2}$).

ionic conductor (i.e., an electrolyte). Conversely, MIECs used in membrane or electrode applications, where *high* electronic conductivity is required, often have Region IIb (sometimes called the semiconducting region) as the wider region. Of the MIECs of interest, those with the fluorite structure typically have a wider Region IIa than the perovskites (one notable exception being LaGaO$_3$), which typically have a wider Region IIb. This circumstance is attributable, in part, to the perovskites' more complex structure and their higher metal to oxygen ratio.

From the system of defect equations in Eqs. (2.3.1) through (2.3.21) proportionality relationships, summarized in Table 2-3, may be deduced, using the Brouwer approach [14], for the dominant defects in each region. The fact that these relationships are retained

Table 2-3. Proportionality relationships between (dominant) defect concentrations and P_{O_2} for each Brouwer regime [14].

	Region I	Region IIa	Region IIb	Region III
Fluorites	$c_e, c_{V_O} \propto P^{-1/6}$	$c_e \propto P^{-1/4}$	$c_{O_i} \propto P^{1/2}$	$c_h, c_{O_i} \propto P^{1/6}$
Perovskites	$c_e, c_{V_O} \propto P^{-1/6}$	$c_e \propto P^{-1/4}$	$c_{V_{A/B}} \propto P^{3/4}$	$c_h, c_{V_{A/B}} \propto P^{3/16}$

in the equations from the model is a testament to their accuracy. However, it is also important to emphasize the differences between the Brouwer [14] approach and the one presented here. In essence, the Brouwer [14] approach reduces the charge balance expression—Eq. (2.3.20) or Eq. (2.3.21)—to a pair of defects that dominate in the region (Brouwer regime) under consideration. This strategy is successful over much of a given region but fails near the boundary between two regions. The failure is due to the presence of non-negligible concentrations of a third defect species in the neighbourhood of each boundary—see Figures 2-3 and 2-4.

Conversely, the new approach presented in this chapter is successful because for a region (i.e., effectively two Brouwer regimes) it reduces the charge balance expression—Eq. (2.3.20) or Eq. (2.3.21)—to a triad, rather than a pair, of dominant defects, see Table 2-4. Consequently, the resulting expressions are continuous across the interface found in that region. Obviously, the best solution would be to model the whole DED without dividing it into regimes or regions. Nevertheless, the model is still quite useful because, in any practical application, most MIECs reside in only one or two regions. For example, for a typical P_{O_2} range (10^{-22} atm. $< P_{O_2} < 1$ atm.) stabilized zirconia and stabilized bismuth oxide[7] operate exclusively in region IIa. Conversely, in that same P_{O_2} range, acceptor-doped ceria typically operates in regions I and IIa. Likewise, $La_{1-x}Sr_xCo_{1-y}Fe_yO_{3-\delta}$[8] operates either in regions IIa and IIb or regions IIb and III.

---

[7] Generally, bismuth oxide decomposes at $P_{O_2} < \sim 10^{-13}$ atm. at 600 °C.

[8] Generally, $La_{1-x}Sr_xCo_{1-y}Fe_yO_{3-\delta}$ decomposes at $P_{O_2} < \sim 10^{-14}$ atm.

Table 2-4. Comparison between the dominant defects pairs of the Brouwer approach [14] and the dominant defect triads of the present model.

Brouwer Regimes	Dominant Defect Pairs	Charge Balance	Modeled Brouwer Regimes	Dominant Defect Triads	Charge Balance
Region I	e', $V_O^{\bullet\bullet}$	$c_e = 2c_{V_O}$	I & IIa	e', $V_O^{\bullet\bullet}$, M_A'	$c_e + c_A = 2c_{V_O}$
Region IIa	$V_O^{\bullet\bullet}$, M_A'	$2c_{V_O} = c_A$	IIa & IIb	$V_O^{\bullet\bullet}$, M_A', $h^\bullet$	$c_A = 2c_{V_O} + c_h$
Region IIb	M_A', $h^\bullet$	$c_h = c_A$	IIb & III (Fluorites)	M_A', $h^\bullet$, O_i''	$c_A + 2c_{O_i} = c_h$
Region III (Fluorites)	$h^\bullet$, O_i''	$c_h = 2c_{O_i}$	IIb & III (Perovskites)	M_A', $h^\bullet$, $V_{A,B}'''$	$c_A + 3c_{V_{A/B}} = c_h$
Region III (Perovskites)	$h^\bullet$, $V_{A,B}'''$	$c_h = 3c_{V_{A,B}}$			

In summary, the Brouwer approach [14] gives suitable results for the functional dependence of defect concentration on P_{O_2} if the MIEC operates in only one Brouwer regime. However, if the MIEC operates in more than one Brouwer regime, the functional dependence of defect concentration on P_{O_2} is better described by the expressions developed in this chapter.

Figures 2-5 and 2-6 compare the concentration of electronic defects—from Eqs. (2.3.58) and (2.3.60)—with the concentration of small polarons in fluorites and perovskites using Eqs. (2.3.27) and (2.3.29). The plots show that as c_e gets larger, eventually $c_{sp-} < c_e$ which, as argued earlier, is a consequence of the small polaron concentration being limited by the number of available cation sites. Many perovskite MIECs of interest become unstable when $c_{sp-} > c_{sp+}$ [27, 28], hence the intersection of the c_{sp-} and c_{sp+} curves may be viewed as a stability boundary for such MIECs.

Figures 2-7 and 2-8 are plots of the non-stoichiometry of a fluorite MIEC (given by 2-δ) and the non-stoichiometry of a perovskite MIEC (given by 3-δ) respectively. For a fluorite MIEC, the non-stoichiometry is given by:
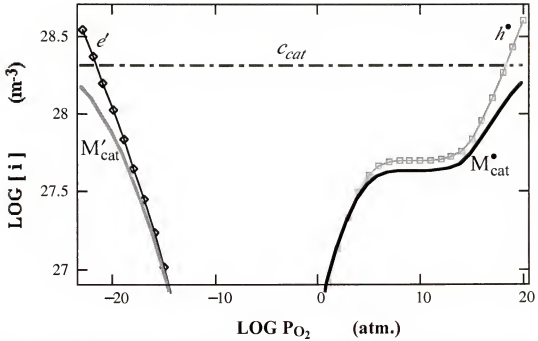
Figure 2-5. Small polaron concentration dependence on P_{O_2} for a fluorite-structured MIEC ($K_r = 10^{75}$ m^{-9}atm$^{1/2}$, $K_m = 10^{25}$ m^{-3}atm$^{-1/2}$, $K_h = 10^{76}$ m^{-9}atm$^{-1/2}$).
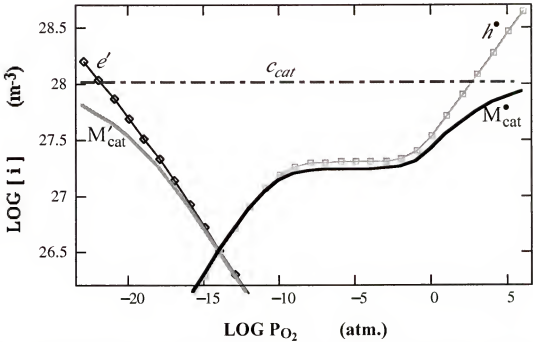
Figure 2-6. Small polaron concentration dependence on P_{O_2} for a perovskite-structured MIEC ($K_r = 10^{73}$ m^{-9}atm$^{1/2}$, $K_m = 10^{32}$ m^{-3}atm$^{-1/2}$, $K_h = 10^{109}$ m^{-9}atm$^{-1/2}$).
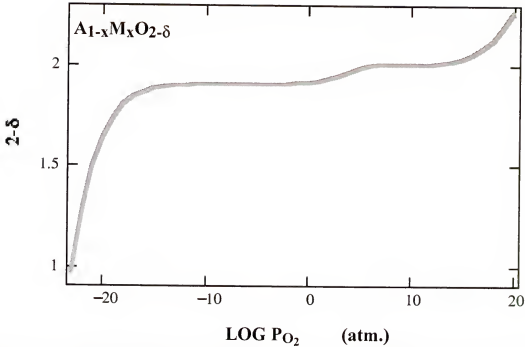
Figure 2-7. Variation of non-stoichiometry with P_{O_2} for a fluorite-structured MIEC ($K_r = 10^{75}$ m⁻⁹atm$^{1/2}$, $K_m = 10^{25}$ m⁻³atm$^{-1/2}$ and $K_h = 10^{76}$ m⁻⁹atm$^{-1/2}$).

$$2 - \delta = 2 \frac{c_{O_O} - c_{V_O} + c_{O_i}}{c_{O_O}} \qquad (2.3.62)$$

where c_{O_O} is the concentration of oxygen atoms in oxygen sites. Similarly, for a perovskite MIEC, the non-stoichiometry is given by:

$$3 - \delta = 3 \frac{c_{O_O} - c_{V_O} + \frac{2}{3} c_{V_{A/B}}}{c_{O_O}} \qquad (2.3.63)$$

In Figure 2-7 two plateaus are observed, the first corresponds to the electrolytic region of the MIEC where the concentration of vacancies, and hence δ, is independent of P_{O_2}—see Figure 2-3. The second plateau corresponds to the semiconducting region where the concentration of holes is independent of P_{O_2}. This plateau occurs because in this region both the vacancy and interstitial concentrations are very small in comparison to the concentration of holes—see Figure 2-3. Consequently, during the second plateau $\delta = 0$
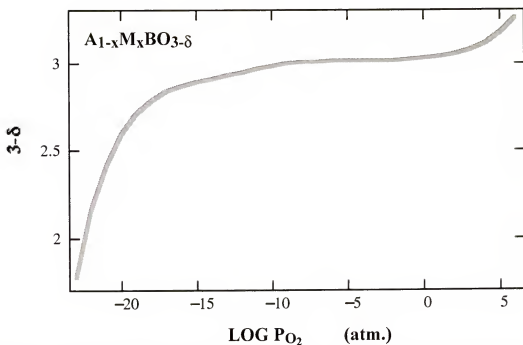
Figure 2-8. Variation of non-stoichiometry with P_{O_2} for a perovskite-structured MIEC ($K_r = 10^{73}$ m^{-9}atm$^{1/2}$, $K_m = 10^{32}$ m^{-3}atm$^{-1/2}$ and $K_h = 10^{109}$ m^{-9}atm$^{-1/2}$).

(i.e., ionic defects, due to the external equilibria or internal disorder, are at a minimum in the MIEC).

In Figure 2-8 only one plateau is observed and it corresponds to the semiconducting or stoichiometric region where $\delta = 0$—see Figure 2-4. An electrolytic region is absent since the perovskite modeled has none—see Figure 2-4.

Now that the functional dependence of defect concentration on P_{O_2} has been modeled generally for perovskite and fluorite oxides, the remainder of the chapter is devoted to demonstrating the usefulness of these models, beyond "mere academic interest".

2.4   Case Study: Acceptor-Doped Ceria

This section consists of a case study of acceptor-doped ceria—specifically samaria-doped ceria (SDC) or gadolinia-doped ceria (GDC)—in an attempt to demonstrate how the models developed in the previous section may be put to use to yield previously

inaccessible information about MIECs. Hence, in this section, determining values for relevant thermodynamic constants, isobaric conductivity, *Wagnerian* flux and defect association is discussed. Ceria has been studied extensively [7, 8, 29, 30] for its catalytic activity as well as its potential for use in SOFCs. While it has found successful application as a catalyst it has not yet been successfully put to use as an electrolyte in a fuel cell. The main hindrance has been its proclivity for electronic conduction, which mitigates its voltage and power output. Recently however some researchers [32 - 35] have found ways by which this problem may be minimized enough to make ceria more viable as an SOFC electrolyte. Consequently, it has become even more important to have a better understanding of the material, to have better data for the relevant material constants and to be able to predict its performance.

2.4.1 Functional Dependence of Defect Concentration on P_{O_2}

SDC and GDC have the fluorite structure, therefore the equilibrium reactions that are applicable to fluorites, given in Eqs. (2.3.1) through (2.3.21), are sufficient to completely describe its defect equilibria. In those expressions, cerium atoms (Ce^{4+}) sitting on the metal/cation sublattice serve as the host for samarium (Sm^{3+}) or gadolinium (Gd^{3+}) cations that constitute the acceptor dopant. *Negatively charged* small polarons consist of electrons *trapped* on a cerium atom—effectively Ce^{3+}—since samaria and gadolinia support only one valence state[9]. *Positively charged* small polarons in acceptor-doped ceria are ignored because of Ce^{5+}, Sm^{4+} and Gd^{4+} are energetically unfavorable. Again, the constraints imposed by small polaron formation are typically ignored when examining the defect equilibria (i.e., it is assumed that $c_e \approx c_{sp-}$). However, since the population of small polarons cannot exceed that of the cations present in the lattice, if there are more electrons than the number of cations, they must be of the *itinerant* variety. Nonetheless, the usual approach is followed hereafter, and c_{sp-} is not included in the defect equations

---

[9] $Sm^{3+} + e^- \rightarrow Sm^{2+}$ is possible but energetically unfavorable in comparison to $Ce^{4+} + e^- \rightarrow Ce^{3+}$.

Table 2-5. Values of the constants used in the numerical solution of SDC's defect equations

Constants	Values from literature	Values used in model	Comments
K_r (m^{-9}atm.$^{1/2}$)	1.4×10^{70}	10^{75}	Reported value [36, 37] is for undoped ceria, doped ceria has a higher K_r [38].
K_f (m^{-6})	1.8×10^{42}	10^{42}	Literature value [39] is for (Ce$_{0.999}$U$_{0.001}$O$_{2-\delta}$)
K_i (m^{-6}K^3)	4.2×10^{26}	10^{26}	Literature value [40] is for undoped ceria
K_- (m^3)	n.a.	$1/c_{cat}$	See Appendix A
c_{cat} (m^{-3})	n.a.	8×10^{27}	
c_A (m^{-3})	n.a.	2×10^{27}	

or (initially) in the numerical solutions. After calculating c_e, c_{sp-} is obtained through Eq. (2.3.27) and is separated from c_e in the DEDs.

As explained in the preceding section, the system of defect equations in Eqs. (2.3.1) through (2.3.21) should, in principle, enable the determination of the defect concentration-P_{O_2} relationships for each defect type. However, reducing that system of simultaneous equations to a single equation produces a fourth-order non-trivial polynomial (when the variable is concentration). Alternatively, by making reasonable simplifications, a cubic equation may be obtained, which has at least one real root if all the coefficients in the equation are real. However, the roots of this cubic equation are not useful because they modulate between being real or complex depending on the P_{O_2} value. Therefore, any analytical expression so derived is limited to a narrow range of P_{O_2}. To avoid such restrictions, the DED must be obtained through numerical methods or by modeling. The values of the equilibrium constants for SDC's defect equilibria, c_A and c_{cat} are provided in Table 2-5. They are approximate values used solely for obtaining a numerical solution and to verify the model. K_r, c_A and c_{cat} are substituted later by more appropriate values, after the determination of K_r from experiment is discussed in ensuing sections.
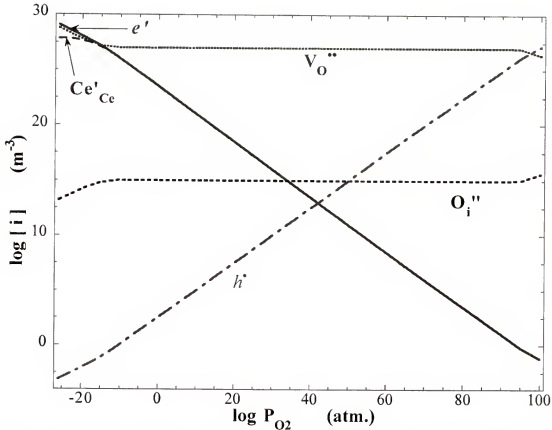
Figure 2-9. Defect equilibrium diagram of SDC obtained through numerical solution of its defect equations—given in Eqs. (2.3.1) to (2.3.21) and (2.4.1) to (2.4.7).

The results of the numerical solution are plotted in Figures 2-9 and 2-10. Figure 2-9 shows that for $P_{O_2} < \sim 10^{70}$ atm., c_{O_i} and c_h are several orders of magnitude smaller than c_{V_O}, c_e and c_A. Therefore, in this region, Eq. (2.3.20) effectively reduces to:

$$c_e + c_A \approx 2c_{V_O} \qquad (2.4.1)$$

Figure 2-9 also shows that the electrolytic region for SDC extends over a range of P_{O_2}'s from $\sim 10^{90}$ atm. to $\sim 10^{-10}$ atm. and that prohibitively high P_{O_2}'s are necessary to observe p-type conduction. Mixed ionic-electronic conductors such as SDC are typically used in P_{O_2}'s between 0.21 and 10^{-22} atm. and Figure 2-10 shows that SDC begins to display significantly mixed conduction for $P_{O_2} < 10^{-15}$ atm. In this region c_{V_O} is no longer
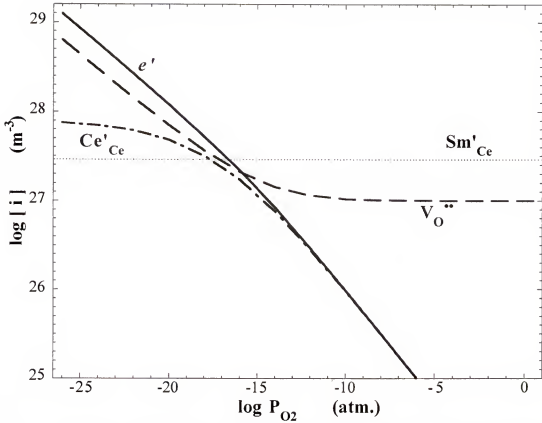
Figure 2-10. Defect equilibrium diagram of SDC in the *region of interest* (reduced from Figure 2-9) obtained through numerical solution of its defect equations—given in Eqs. (2.3.1) to (2.3.21) and (2.4.1) to (2.4.7).

approximately constant (i.e., independent of pressure). Clearly, assuming a constant c_{V_O} across the mixed conducting region is misleading and gives incorrect results in models [41, 42] in which this assumption is made. Finally, over most of the DED (Figure 2-9) $c_e \approx c_{sp-}$ ($c_{e>} \approx 0$) except at very low P_{O_2} (Figure 2-10) when $c_e > c_{sp-}$ ($c_{e>} > 0$).

As mentioned earlier, it is important, for proper description of associated phenomena, to be able to determine analytically the defect distribution in MIECs as a function of P_{O_2}. However, a complete solution of the system of defect equations, giving defect concentration as a function of oxygen partial pressure, is not yet available. Hence, one set of equations from the model presented in section 2.3 may be used to provide an analytical expression for the functional dependence of defect concentration on P_{O_2}. In addition, Eqs. (2.3. 37) and (2.3.38) should be appropriate since acceptor-doped ceria

finds application in the range 10^{-22} atm. $< P_{O_2} < 0.21$ atm., which corresponds to its *low* P_{O_2} region, as defined previously (i.e., corresponding to Regions I and IIa, the low to intermediate Brouwer regimes). That is,

$$c_{V_O}(P) = \left[\tfrac{3}{4} K_r^{\frac{1}{2}} P^{-\frac{1}{4}} + \left(\tfrac{1}{2} c_A\right)^{\frac{3}{2}} \right]^{\frac{2}{3}} \tag{2.4.2}$$

and

$$c_e(P) = K_r^{\frac{1}{2}} P^{-\frac{1}{4}} \left[\tfrac{3}{4} K_r^{\frac{1}{2}} P^{-\frac{1}{4}} + \left(\tfrac{1}{2} c_A\right)^{\frac{3}{2}} \right]^{-\frac{1}{3}} \tag{2.4.3}$$

$c_{sp-}(P)$ may be obtained by substituting Eq. (2.4.3) into Eq. (2.3.27) with the result:

$$c_{sp-}(P) = \frac{K_- c_{cat} K_r^{\frac{1}{2}} P^{-\frac{1}{4}} \left[\tfrac{3}{4} K_r^{\frac{1}{2}} P^{-\frac{1}{4}} + \left(\tfrac{1}{2} c_A\right)^{\frac{3}{2}} \right]^{-\frac{1}{3}}}{1 + K_- K_r^{\frac{1}{2}} P^{-\frac{1}{4}} \left[\tfrac{3}{4} K_r^{\frac{1}{2}} P^{-\frac{1}{4}} + \left(\tfrac{1}{2} c_A\right)^{\frac{3}{2}} \right]^{-\frac{1}{3}}} \tag{2.4.4}$$

Relations for the concentration of holes and oxygen interstitials, in the *region of interest*, as a function of oxygen partial pressure may be obtained in a similar fashion as discussed in the previous section. These results are not given, however, since the concentration holes and oxygen interstitials of are negligibly small for SDC in the *region of interest*, as shown in Figures 2-9 and 2-10.

The verity of Eqs. (2.4.2) through (2.4.4) depends on whether the simplifying condition stipulated in section 2.3.4, i.e., $K_r << 16 c_{V_O}^3 P^{\frac{1}{2}}$, is applicable. Comfortingly, this constraint is satisfied for all P_{O_2}'s in the *region of interest*. Eqs. (2.4.2) through (2.4.4) are plotted in Figure 2-11 along with the numerical solution of the defect equations for the relevant defect species and Porat and Tuller's [11] equation (for P_{O_2} as a function of defect concentration) in Eq. (2.2.2); the latter for independent verification of the
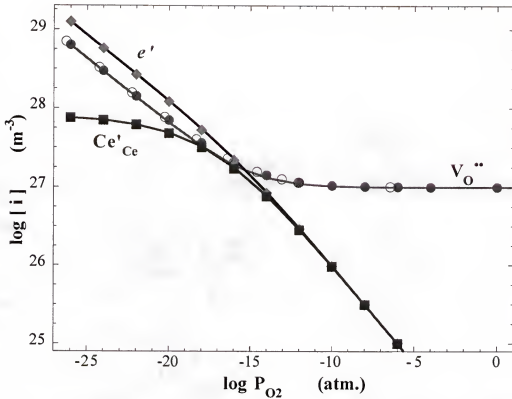
Figure 2-11. Comparison of SDC's DED obtained numerically (solid symbols), from the model (lines), and from Porat and Tuller [11] (open symbols).

results. The observed close fit demonstrates the validity and accuracy of the model in describing the defect equilibria of the aforementioned defect species in the *region of interest*, i.e., from ambient atmospheric to reducing conditions (< 10^{-15} atm.).

2.4.2 Evaluating the Magnitude of the Equilibrium Constant, K_r

In the equations developed in the preceding section, for the functional dependence of defect concentration on oxygen partial pressure, the knowledge of two material constants, c_A and K_r are required. c_A is determined by the amount of acceptor dopant used in the fabrication of the MIEC. K_r, however, must be deduced from values obtained from experiment. In this section, three possible ways of evaluating K_r are examined.

Estimation of K_r from reduction of ceria to cerium (III) oxide. Some sense of the approximate value of K_r may be deduced by considering the reduction of ceria to cerium

(III) oxide which may be written as:

$$2CeO_2 \leftrightarrow Ce_2O_3 + \tfrac{1}{2}O_2 \qquad \Rightarrow \qquad K_t = a_{Ce_2O_3}\, a_{O_2}^{\frac{1}{2}}\, a_{CeO_2}^{-2} = \exp\left(-\frac{\Delta G_t}{RT}\right) \quad (2.4.5a)$$

or

$$2Ce_{Ce}^{\times} + 4O_O^{\times} \leftrightarrow 2Ce_{Ce}^{\times} + 3O_O^{\times} + \tfrac{1}{2}O_2 \qquad \Rightarrow \qquad K_t = \frac{P^{\frac{1}{2}}}{c_{O_O} P_{ref}^{\frac{1}{2}}} \quad (2.4.5b)$$
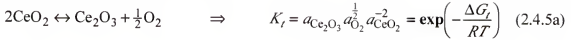
where a is the activity of the chemical species, K_t is the equilibrium constant and ΔG_t is the free energy for the reaction. However, since ceria may be represented as $Ce_{Ce}^{\times} + 2O_O^{\times}$, then, as a first approximation, Eq. (2.4.5) may be rewritten as:

$$2Ce_{Ce}^{\times} + 4O_O^{\times} \leftrightarrow 2Ce_{Ce}' + 3O_O^{\times} + V_O^{\bullet\bullet} + \tfrac{1}{2}O_2 \Rightarrow K_t^* = \frac{c_{sp-}^2\, c_{V_O}\, P^{\frac{1}{2}}}{c_{O_O}\, c_{cat^\circ}^2\, P_{ref}^{\frac{1}{2}}} = \exp\left(\frac{-\Delta G_t^*}{RT}\right) (2.4.6)$$
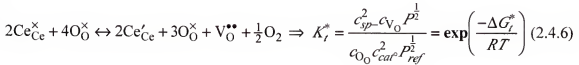
where K_t^* is the equilibrium constant and ΔG_t^* is the Gibbs' free energy for the reaction.

ΔG_t^* includes the enthalpy of vacancy formation as well as the entropy change in the ceria lattice hence it is unlikely that the reactions in Eqs. (2.4.5) and (2.4.6) are truly equivalent. That is, $\Delta G_t^* \neq \Delta G_t$ is a reasonable expectation. Therefore one may write,

$$\Delta G_t^* = \Delta G_t - RT\ln\theta \qquad \Rightarrow \qquad K_t^*\theta = K_t \qquad (2.4.7)$$

where θ ($\theta > 0$) is a dimensionless correction term to account for the free energy difference between the transformation of CeO_2 to $CeO_{2-\delta}$ and CeO_2 to Ce_2O_3. Hence, combining Eqs. (2.3.2), (2.4.6) and (2.4.7) (for $c_e \ll c_{cat}$ such that $c_e = c_{sp-}$ and $c_{cat^\circ} \approx c_{cat}$) yields:

$$K_r\theta = K_f c_{cat^\circ}^2 c_{O_O} P_{ref}^{\frac{1}{2}} \qquad \Rightarrow \qquad \log K_r = \log\left(K_f c_{O_O} c_{cat^\circ}^2 P_{ref}^{\frac{1}{2}}\right) - \log\theta \qquad (2.4.8)$$

K_r may now be deduced from Eq. (2.4.15b) by substituting values for P_{ref}, c_{cat°, c_{O_O} and K_t, which may be obtained from thermodynamic tables. Thus for $P_{ref} = 1$ atm, $c_{cat} \approx 2 \times 10^{28}$ atoms/m^3, $c_A = 0.5 \times 10^{28}$ atoms/m^3—SDC lattice constant = 0.544 nm [29]—$c_{O_O} \approx 4.75 \times 10^{28}$ atoms/m^3 and log (K_t) = -11.595 at 1073 K [43], yields

$$K_r\theta = 10^{73.7} \text{ m}^{-9}\text{atm.}^{1/2}$$

or

$$\log K_r = 73.7 - \log \theta$$

If log θ can be quantified, or is small enough (i.e., $\theta \approx 1$) to be ignored, then this approach provides a good estimate of K_r. Without more rigorous thermodynamic analysis, it is difficult to ascertain the true magnitude of θ, but at the very least, this calculation should give some idea of the magnitude of K_r.

Estimation of K_r from *open-circuit* voltage. In this section, a method is developed for calculating K_r from measurement of the *open-circuit* voltage, Φ_{oc}, across an MIEC of thickness L, which is given by[10]:

$$\Phi_{oc} = \int_{\mu_{O_2}^{s=0}}^{\mu_{O_2}^{s=L}} \frac{\sigma_V}{\sigma_V + \sigma_e} \cdot \frac{\mathrm{d}\mu_{O_2}}{4F} = \frac{RT}{4F}\int_{P_0}^{P_L} \frac{\mathrm{d}\ln P}{1 + \Theta K_r^{\frac{1}{2}} P^{-\frac{1}{4}}\left[\frac{3}{4} K_r^{\frac{1}{2}} P^{-\frac{1}{4}} + \left(\frac{1}{2} c_A\right)^{\frac{3}{2}}\right]^{-1}} \qquad (2.4.9)$$

where σ_V is the oxygen vacancy conductivity and

$$\Theta = \frac{z_e^2 D_e}{z_V^2 D_V} \qquad (2.4.10)$$

---

[10] This expression will be derived formally in chapter 3.

D is diffusivity and μ is the chemical potential which, for the species i, is given by:

$$\mu_i = RT\ln a_i \approx \underbrace{RT\ln P_i}_{\text{gaseous species}} \approx \underbrace{RT\ln c_i}_{\text{condensed species}} \quad (2.4.11)$$

Integrating Eq.(2.4.9) yields

$$\Phi_{oc} = \frac{RT}{4F}\ln\frac{P_L}{P_0} - \frac{RT}{F}\ln\frac{\left(\frac{3}{4}+\Theta\right)K_r^{\frac{1}{2}}P_0^{-\frac{1}{4}} + \left(\frac{1}{2}c_A\right)^{\frac{3}{2}}}{\left(\frac{3}{4}+\Theta\right)K_r^{\frac{1}{2}}P_L^{-\frac{1}{4}} + \left(\frac{1}{2}c_A\right)^{\frac{3}{2}}}$$

$$= \Phi_{th} - \frac{RT}{F}\ln\frac{\left(\frac{3}{4}+\Theta\right)K_r^{\frac{1}{2}}P_0^{-\frac{1}{4}} + \left(\frac{1}{2}c_A\right)^{\frac{3}{2}}}{\left(\frac{3}{4}+\Theta\right)K_r^{\frac{1}{2}}P_L^{-\frac{1}{4}} + \left(\frac{1}{2}c_A\right)^{\frac{3}{2}}} \quad (2.4.12a)$$

which may be rearranged to give

$$K_r^{\frac{1}{2}} = \frac{\left(\frac{1}{2}c_A\right)^{\frac{3}{2}}}{\frac{3}{4}+\Theta} \cdot \frac{1 - \left(\frac{P_L}{P_0}\right)^{-\frac{1}{4}\left(1-\frac{\Phi_{oc}}{\Phi_{th}}\right)}}{P_0^{-\frac{1}{4}}\left(\frac{P_L}{P_0}\right)^{-\frac{1}{4}\left(1-\frac{\Phi_{oc}}{\Phi_{th}}\right)} - P_L^{-\frac{1}{4}}} \quad (2.4.12b)$$

where Φ_{th} is the theoretical (Nernst) potential,

In principle, Eq. (2.4.12) allows K_r to be determined from measurements of Θ and Φ_{oc} for a given P_0 and P_L. However, Φ_{oc} may need to be corrected for electrode effects which alter true oxygen activity seen by the electrolyte at each interface. Furthermore, as Steele [7] points out, values for D_e, and hence Θ, are difficult to obtain from experiment. And values available in the literature are inconsistent. Gödickemeier *et al.* [44, 45] modeled and evaluated the overpotentials for various electrodes on a SDC electrolyte. From their data for a $La_{0.84}Sr_{0.16}CoO_3$ cathode and a $Ni-Ce_{0.9}Ca_{0.1}O_{1.9-\delta}$ cermet anode on an SDC electrolyte, values of $\Phi_{oc} \approx 800$ mV ($\Phi_{oc} \approx 740$ mV when corrected for electrode overpotentials [44, 45]) and $\Phi_{th} \approx 941$ mV for $P_L = 0.21$ atm. and $P_0 \approx 4 \times 10^{-19}$

Table 2-6. Calculated values of Θ and K_r for SDC from the *uncorrected* Φ_{oc} data of Gödickemeier *et al.* [44, 45].

$\Theta = D_e/4D_V$	K_r (m^{-9}atm.$^{1/2}$)	$\ln K_r$ [ln (m^{-9}atm.$^{1/2}$)]
0.1	1.9×10^{74}	171.0
1	4.4×10^{73}	169.6
10	1.2×10^{72}	165.9
100	1.3×10^{70}	161.4
1000	1.3×10^{68}	156.9

atm. at 800 ^{0}C were obtained. K_r is calculated for various values of Θ, from Eq. (2.4.12), using *uncorrected* and *corrected* (for electrode overpotential) data from Gödickemeier *et al.* [44, 45] and the results are shown in Tables 2-6 and 2-7 respectively.

Two significant and related features of Eq. (2.4.12) are of particular interest. Firstly, for given values of t_{ion}, c_A, P_L and P_0, the term $K_r(3 + 4\Theta)^2$ is a constant

$$K_r(3+4\Theta)^2 = 2c_A^3 \cdot \left[\frac{1-\left(\dfrac{P_L}{P_0}\right)^{-\frac{1}{4}\left(1-\frac{\Phi_{oc}}{\Phi_{th}}\right)}}{P_0^{-\frac{1}{4}}\left(\dfrac{P_L}{P_0}\right)^{-\frac{1}{4}\left(1-\frac{\Phi_{oc}}{\Phi_{th}}\right)} - P_L^{-\frac{1}{4}}} \right]^2 \equiv \textbf{constant} \qquad (2.4.12c)$$

and therefore, because of its formulation, K_r decreases as Θ increases. Secondly, if $\Phi_{oc} = \Phi_{th}$ (the perfect electrolyte) K_r—and K_i, see Eq. (2.3.22)—is zero, i.e., there are no *available* electrons in the MIEC. These results may be understood by considering Eq. (2.3.2) which shows that the exchange of oxygen atoms across the gas-MIEC interface requires the supply or consumption of *available* electrons to or from the surface. The MIEC can fulfill this requirement in two ways. One way is by the production of electrons, which depends on the size of the MIEC's band gap which in turn determines the magnitude of K_I—and therefore K_r (see Eqs. (2.3.1), (2.3.2) and (2.3.22)).

Table 2-7. Calculated values of Θ and K_r for SDC from the *corrected* Φ_{oc} data of
Gödickemeier *et al.* [44, 45].

$\Theta = D_e/4D_V$	K_r (m^{-9}atm.$^{1/2}$)	$\ln K_r$ [ln (m^{-9}atm.$^{1/2}$)]
0.1	8.7 x 10^{74}	172.6
1	2.1 x 10^{74}	171.1
10	5.5 x 10^{72}	167.5
100	6.2 x 10^{70}	163.0
1000	6.3 x 10^{68}	158.4

Alternatively (or in conjunction), the supply of electrons to the interface may be controlled by the speed at which electrons (relative to oxygen vacancies) arrive to, or depart from the interface, i.e., by the magnitude of D_e—and therefore Θ. Hence K_r and Θ (or $K_r(3 + 4\Theta)^2$) may be considered as measures of the ability of the MIEC to sustain electron fluxes through the gas-MIEC interface during oxygen exchange. Accordingly, it is difficult to separate K_r and D_e in experiments which measure properties that are dependent on both defect concentration (K_r) and diffusivity (Θ or D_e), e.g., conductivity and transference number measurements.

In agreement with $K_r(3 + 4\Theta)^2$ being a constant—see Tables 2-6 and 2-7—Θ is small when K_r is large and vice versa. In addition, $\ln K_r$ (ln K_r = -$\Delta G_r/k_BT$, where ΔG_r is the Gibbs' free energy associated with the reaction in Eq. (2.3.2))[11] doesn't change much even when Θ varies over ~2 orders of magnitude. From the preceding discussion, this result may indicate that the oxygen exchange process is limited by the ability of the SDC to produce electrons (i.e., its band gap) rather than the relative speed (i.e., Θ) they are supplied to, or consumed from, the interface.

---

11   In the strictest sense K_r should be dimensionless when used for the calculation of ΔG_r. However, the validity of the analyses presented is not lost since the additional term(s) required to make K_r dimensionless constitute a constant. That is, in Eq. (2.3.2), ln K_r = -$\Delta G_r/k_BT$ + ln ϑ, where ϑ is a unit bearing constant.

Estimation of K_r from thermogravimetry. Although the estimations of K_r in the sections above are useful, K_r is most suitably determined from thermogravimetric experiments, which may be designed to give the weight change of an MIEC sample (and hence the concentration of defects) as a function of P_{O_2} [46]. However, it is usually very difficult to get accurate and reproducible data from thermogravimetric experiments because of the high sensitivity required to detect very small changes in the mass of the specimen [12]. Recently, Kobayashi *et al.* [47] determined the oxygen/metal (c_{O_O}/c_{cat}) atom ratios for SDC for various temperatures and pressures. The vacancy concentration is related to the c_{O_O}/c_{cat} ratio as follows:

$$c_{V_O} = c_{cat}\left(2 - c_{O_O}/c_{cat}\right) \qquad (2.4.13)$$

Substituting Eq. (2.4.13) into Eq. (2.4.2) and rearranging it yields:

$$K_r^{\frac{1}{2}} = \tfrac{4}{3}P^{\frac{1}{4}}c_{V_O}^{\frac{3}{2}} - \tfrac{4}{3}P^{\frac{1}{4}}\left(\tfrac{1}{2}c_A\right)^{\frac{3}{2}} = \tfrac{4}{3}P^{\frac{1}{4}}\left[c_{cat}\left(2 - c_{O_O}/c_{cat}\right)\right]^{\frac{3}{2}} - \tfrac{4}{3}P^{\frac{1}{4}}\left(\tfrac{1}{2}c_A\right)^{\frac{3}{2}} \qquad (2.4.14)$$

K_r is calculated for c_{O_O}/c_{cat} ratios in the range 0.186 to 0.189 at 800 °C where $c_{cat} = 2.5 \times 10^{28}$ m^{-3}—SDC lattice constant = 0.544 nm [29]—and $c_A = 0.2c_{cat}$ using Eq. (2.4.14); the results are shown in Table 2-8. The values calculated for K_r are narrowly distributed and so the standard deviation of the data set (an admittedly small population) for $\ln K_r$[12] is 0.263 [ln (m^{-9}atm.$^{1/2}$)] which is < 0.2% in the worst case. The average value of K_r[12] in Table 2-8 is 9.97 $\times$ 10^{71} m^{-9}atm.$^{1/2}$.

Summary. All three methods that were used to calculate/estimate the magnitude of K_r show remarkable agreement (especially for ~1 < Θ < ~10). Specifically, the results obtained from each method (using $\Theta = 10$) are < 5% apart for $\ln(K_r)$, which is well within experimental error. Such unanimity alludes to the correctness of the approaches—and,

---

[12] The geometric mean and variance were required to calculate the standard deviation in the K_r values.

Table 2-8. Calculated values of K_r for SDC from thermogravimetry data of Kobayashi *et al*. [47].

c_{O_O}/c_{cat}	$\log P_{O_2}$ [ln (atm.)]	K_r (m^{-9}atm.$^{1/2}$)	$\ln K_r$ (m^{-9}atm.$^{1/2}$)
1.86	-20.5	6.732×10^{71}	165.390
1.87	-19.5	1.149×10^{72}	165.925
1.88	-18.75	1.159×10^{72}	165.934
1.89	-17.55	1.102×10^{72}	165.883

therefore the model. Admittedly, in each case, the error analysis of the experimental data was not reported. In their absence confidence in the actual data, and any results educed from it, diminishes. Nevertheless, obtaining such similar results from such disparate sources and methods is, at the very least, reassuring. The magnitude of K_r is revisited briefly in Chapter 3 where yet another method is applied to evaluate it. As will become increasingly clear (if not already so) through the remainder of this manuscript, K_r is a critical constant and it is worth the effort to find reliable ways of determining its value accurately.

Finally, by comparing the formalism used for the thermodynamic estimation of K_r, Eq. (2.4.8), with that used in the estimation from OCV measurements, Eq. (2.4.12), one may surmise that θ is a measure of the availability of electrons for the reaction in Eq. (2.3.2). That is, θ is related to Θ. Through (at this point, tenuous) extrapolation one may further deduce that as $\theta \to 1$, Eq. (2.4.5) becomes more favourable than Eq. (2.3.2), i.e., cerium (IV) oxide will decompose to cerium (III) oxide rather than become non-stoichiometric. Conversely, as $\theta \to 0$ Eq. (2.4.5) is less favourable and departures from stoichiometry (within thermodynamic limits) are sustainable in cerium (IV) oxide.

To support this assertion, the complicated processes involved in the reaction in Eq. (2.3.2) may be divided into simpler parts by setting up a simple kinetic scheme described

in the equations below[13]:

Step 1 $\qquad \frac{1}{2}O_2 \leftrightarrow O_{ads}$ $\qquad$ (2.4.15)

Step 2 $\qquad O_{ads} + e^- \leftrightarrow O^-_{ads}$ $\qquad$ (2.4.16)

Step 3 $\qquad O^-_{ads} + e^- \leftrightarrow O^{2-}_{ads}$ $\qquad$ (2.4.17)

Step 4 $\qquad O^{2-}_{ads} + V^{\bullet\bullet}_O \leftrightarrow O^\times_O$ $\qquad$ (2.4.18)
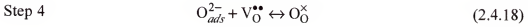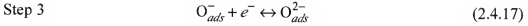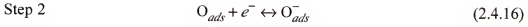
where the subscript "*ads*" refers to species adsorbed on the surface of the sample. In this scheme, oxygen molecules in the gas phase adsorb on the surface of the sample (Step 1)—generally at the triple phase, gas-conductor-MIEC, boundary. Electrons then diffuse from the conduction band of the MIEC or the electrode where they react with (Steps 2 and 3) the adsorbed oxygen species. Finally, the ionized oxygen species reacts with a vacancy thereby being incorporated into the lattice (Step 4). Typically, Step 1 occurs at the surface, Step 4 in the near surface layer and Steps 2 and 3 at or near the surface of the MIEC. For simplification, the sequence outlined in Eqs. (2.4.15) through (2.4.18) may be summarized as

$$V^{\bullet\bullet}_O + 2e' + \frac{1}{2}O_2 \leftrightarrow \left(V^{\bullet\bullet}_O \circ O^{2-}_{ads}\right) \leftrightarrow O^\times_O \qquad (2.4.19)$$
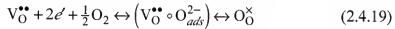
where oxygen vacancies and ionized oxygen atoms diffuse in the near surface layer where they meet adsorbed oxygen atoms to form an *encounter group*, $\left(V^{\bullet\bullet}_O \circ O^{2-}_{ads}\right)$, which later reacts to form the final product, $O^\times_O$. For the formation of the *encounter group* one may write

---

13 The actual scheme may vary from one MIEC to the other but the one presented here is generally applicable [54].

$$V_O^{\bullet\bullet} + 2e' + \tfrac{1}{2}O_2 \rightarrow \left(V_O^{\bullet\bullet} \circ O_{ads}^{2-}\right) \qquad \Rightarrow \qquad v = \kappa_D c_V c_e^2 P^{\frac{1}{2}} \qquad (2.4.20)$$
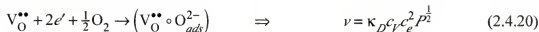
where v is the reaction rate, κ is the rate constant for the reaction and the subscript D signifies diffusion. Conceptually, the *encounter group* can break up without reacting or its constituents may react to form the final product, $O_O^\times$. Assuming that either reaction is pseudo-first-order, then

$$\left(V_O^{\bullet\bullet} \circ O_{ads}^{2-}\right) \rightarrow V_O^{\bullet\bullet} + 2e' + \tfrac{1}{2}O_2 \qquad \Rightarrow \qquad v = \kappa_D' c_{O^*} \qquad (2.4.21)$$
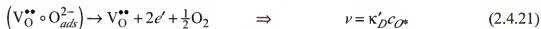
where c_{O^*} is the concentration of the *encounter group*, and

$$\left(V_O^{\bullet\bullet} \circ O_{ads}^{2-}\right) \rightarrow O_O^\times \qquad \Rightarrow \qquad v = \kappa_a c_{O^*} \qquad (2.4.22)$$
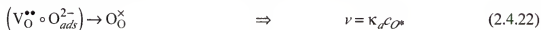
At steady-state the net rate of change of c_{O^*} is given by:

$$\frac{dc_{O^*}}{dt} = 0 = \kappa_D c_V c_e^2 P^{\frac{1}{2}} - \kappa_D' c_{O^*} - \kappa_a' c_{O^*} \qquad (2.4.23)$$

which may be rearranged to yield:

$$c_{O^*} = \frac{\kappa_D}{\kappa_D' + \kappa_a} c_V c_e^2 P^{\frac{1}{2}} \qquad (2.4.24)$$

The overall rate law for the formation of the final product, $O_O^\times$ is therefore

$$\frac{dc_O}{dt} = \kappa_a c_{O^*} = \frac{\kappa_a \kappa_D}{\kappa_D' + \kappa_a} c_V c_e^2 P^{\frac{1}{2}} = \kappa_r c_V c_e^2 P^{\frac{1}{2}} \qquad (2.4.25)$$

where

$$\kappa_r = \frac{\kappa_a \kappa_D}{\kappa'_D + \kappa_a} \qquad (2.4.26)$$

Furthermore, by definition (also see Eq. (2.4.1)):

$$\frac{1}{K_r} = \frac{\kappa_r}{\kappa'_r} = \frac{\kappa_a \kappa_D}{\kappa'_D + \kappa_a} \cdot \frac{1}{\kappa'_r} \qquad (2.4.27)$$

If the *encounter group* is much more likely react to form $O_O^\times$ rather than break up without reacting then—by comparing Eqs. (2.4.21) and (2.4.22)—$\kappa_a \gg \kappa'_D$ and Eq. (2.4.25) reduces to

$$K_r \approx \frac{\kappa'_r}{\kappa_D} \qquad (2.4.28)$$

or

$$\log K_r = \log \kappa'_r - \log \kappa_D \qquad (2.4.29)$$

Comparing Eq. (2.4.29) with Eq. (2.4.8) suggests that

$$\theta \sim \kappa_D \qquad (2.4.30)$$

which supports the assertion that θ is indeed related to Θ. This is especially convincing when one considers that for $K_r = 9.97 \times 10^{71}$ m^{-9}atm.$^{1/2}$ (calculated in section 2.4.2.3), $\log \Theta \approx 1.4$ (calculated from Eq. (2.4.12)) and the difference between that K_r value and the one calculated in section 2.4.2.1 (i.e., $\log \theta$) is ~ 1.3.

The overall picture is that the ability of the MIEC to exchange oxygen with an external gas phase is dependent on how rapidly oxygen vacancies and ionized oxygen

atoms diffuse through the near surface layer of the MIEC. Finally, it can be shown [48] that

$$\kappa_D = 4\pi\left(r_V + r_{ads}\right)\left(D_V + D_{ads}\right) \qquad (2.4.31)$$

where r is the ionic radius of the species and the subscript "ads" refers to the adsorbed O^{2-} ion.

2.4.3 Transport Properties: Conductivity, Transference Number and Flux

Conductivity and transference number. Having earlier derived expressions for the functional dependence of defect concentrations on oxygen potential in SDC, expressions for the defect conductivity and ionic transference number of an MIEC may now be obtained. The conductivity of the MIEC with respect to vacancies and electrons is given by:

$$\sigma_V(P) = |z_V|Fu_V c_{V_O}(P) \qquad (2.4.32)$$

and

$$\sigma_e(P) = |z_e|Fu_e c_e(P) \qquad (2.4.33)$$

where u is mobility (for the ith defect $u_i = |z_i|D_i/k_BT$). The total conductivity, σ_{tot}, of an MIEC is the sum of the conductivities of all the charge carriers and, for SDC (in Regions I and IIa), is given by the sum of Eqs (2.4.32) and (2.4.33), i.e.,

$$\sigma_{tot}(P) = \sigma_V(P) + \sigma_e(P) = |z_V|Fu_V c_{V_O}(P) + |z_e|Fu_e c_e(P) \qquad (2.4.34)$$

The ionic transference number t_{ion} may be defined as the ratio of the ionic conductivity (which is σ_V for the MIECs of interest) to the total conductivity and is given

by:

$$t_{ion}(P) = \frac{\sigma_I(P)}{\sigma_{tot}(P)} = \frac{|z_V|Fu_V c_{V_O}(P)}{|z_V|Fu_V c_{V_O}(P) + |z_e|Fu_e c_e(P)} \tag{2.4.35}$$

Substituting Eqs. (2.4.2) and (2.4.3) into Eqs. (2.4.34) and (2.4.35) yields

$$\sigma_{tot}(P) = |z_V|Fu_V\left[\tfrac{3}{4}K_r^{\frac{1}{2}}P^{-\frac{1}{4}} + \left(\tfrac{1}{2}c_A\right)^{\frac{3}{2}}\right]^{\frac{2}{3}} + |z_e|Fu_e K_r^{\frac{1}{2}}P^{-\frac{1}{4}}\left[\tfrac{3}{4}K_r^{\frac{1}{2}}P^{-\frac{1}{4}} + \left(\tfrac{1}{2}c_A\right)^{\frac{3}{2}}\right]^{-\frac{1}{3}} \tag{2.4.36}$$

and, with a little rearranging,

$$t_{ion}(P) = \left\{1 + \Theta K_r^{\frac{1}{2}}P^{-\frac{1}{4}}\left[\tfrac{3}{4}K_r^{\frac{1}{2}}P^{-\frac{1}{4}} + \left(\tfrac{1}{2}c_A\right)^{\frac{3}{2}}\right]^{-1}\right\}^{-1} \tag{2.4.37}$$

Figure 2-12 shows a comparison of σ versus P_{O_2} as predicted by Eq. (2.4.36) with experimental data from Eguchi *et al.* [49]. The value of u_V used (9.2×10^{-8} m^{2}V^{-1}s^{-1}) for the plot was taken from the data of Eguchi *et al.* [49]. For K_r, the geometric mean of the values (which is equivalent to the standard mean of the ΔG_r values) computed in section 2.4.2 was used. u_e was adjusted to get the best fit of Eq. (2.4.36) which yielded $u_e = 2.5 \times 10^{-6}$ m^{2}V^{-1}s^{-1} ($\Theta \approx 138$). This result is in good agreement with values for similar systems reported in the literature [7, 8, 50]. It should be noted, however, that there is considerable spread in the values of u_e reported for SDC in the literature. This point was reinforced in recent reviews by Steele [7] and Mogensen *et al.* [8]. The transference number, as given by Eq. (2.4.37), is also plotted in Figure 2-12 as a function of pressure using the same values used to fit Eq. (2.4.36) to the σ versus P_{O_2} data of Eguchi *et al.* [49]. The trend shown is typical of such plots [51, 52].
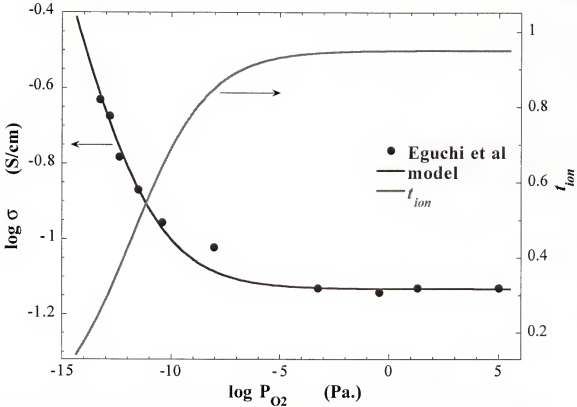
Figure 2-12. Modeled σ(P) fitted to experimental data from Eguchi *et al.* [49] for SDC.

Flux. Some time ago, Wagner [53] developed a theory for the oxidation of metals that depends on the ability of oxygen ions to migrate through the oxide layer on the surface of the metal to get to the metal surface underneath. Since any oxide layer may loosely be characterized as an MIEC, Wagner's theory has been extended to oxygen permeation in MIECs [54 - 56]. Thus Wagner's equation, is used to determine the *open-circuit* flux of oxygen through an MIEC as a function of the P_{O_2} (P_0 and P_L) on each side of the MIEC. Typically, Wagner's equation [53] is solved by making simplifying assumptions for the functional dependences of $\sigma_V(P)$ and/or $\sigma_e(P)$. The most prevalent assumptions are that (a) σ_V is constant and $\sigma_e(P)$ may be represented by a Brouwer [14] type equation and/or (b) $\sigma_V(P) \ll \sigma_e(P)$. Both assumptions are appropriate for solid electrolytes such as stabilized zirconia and bismuth oxide. However, they are unsuitable for many other MIECs of technical interest, such as SDC, because $\sigma_V(P)$ is not constant
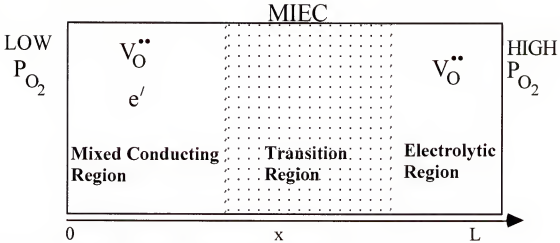
Figure 2-13. An oxide MIEC in an arbitrary P_{O_2} gradient

in the range $P_0 < P < P_L$, for typical values of P_0 and P_L. The second assumption may be suitable for some MIECs operating outside the electrolytic region. It is inapplicable, however, if the MIEC is electrolytic for a part of the range $P_0 < P < P_L$. Samaria-doped ceria, for example, becomes an electrolyte for $P_{O_2} > \sim 10^{-7}$ atm. and $\sigma_V(P) > \sigma_e(P)$. Additionally, as was discussed earlier in section 2.2.1, the Brouwer [14] equations are applicable within a single Brouwer region. However, depending on the values of P_L and P_0 the MIEC may span more than one Brouwer region, as depicted in Figure 2-13, and thereby invalidate both assumptions.

Earlier, expressions were derived for $\sigma_V(P)$ and $\sigma_e(P)$ in the *region of interest*—Eqs. (2.4.32) and (2.4.33). Hence, Wagner's equation [53] may now be solved without the simplifying assumptions described above. Wagner's equation [53] is given by:

$$j_{O_2} = -\frac{RT}{4^2 F^2 L} \cdot \int_{P_0}^{P_L} \frac{\sigma_V(P)\sigma_e(P)}{\sigma_V(P) + \sigma_e(P)} \cdot \frac{dP}{P} \qquad (2.4.38)$$

where j_{O_2} is the oxygen flux, and P_0 and P_L are the P_{O_2} 's at $x = 0$ and $x = L$ respectively. For SDC Eqs. (2.4.32) and (2.4.33) are substituted (with $z_V = 2$ and $z_e = -1$) into Wagner's equation with the result:

$$j_{O_2} = \frac{D_v \Omega^2}{\left(1 + \frac{4}{3}\Theta\right)L} \left\{ \frac{c_{V_O}(P)}{2\Omega^2} - \frac{1}{6}\ln\frac{c_{V_O}(P) - \Omega\sqrt{c_{V_O}(P)} + \Omega^2}{\left(\sqrt{c_{V_O}(P)} + \Omega\right)^2} - \frac{1}{\sqrt{3}}\tan^{-1}\frac{2\sqrt{c_{V_O}(P)} - \Omega}{\Omega\sqrt{3}} \right\}\Bigg|_{P_0}^{P_L}$$

(2.4.39)

where

$$\Omega^3 = -\frac{\frac{4}{3}\Theta}{1 + \frac{4}{3}\Theta}\left(\frac{1}{2}c_A\right)^{\frac{3}{2}}$$
(2.4.40)

The oxygen flux, as described by Eq. (2.4.39), is plotted in Figure 2-14, for $L = 1$ mm, as a function of P_{O_2} (a) with the oxidizing side of the MIEC at a constant P_{O_2} of 0.21 atm. while varying the P_{O_2} of the reducing side and (b) with the reducing side of the MIEC at a constant P_{O_2} of 10^{-20} atm. while varying the P_{O_2} of the oxidizing side. For case (a) there is essentially no flux until the P_{O_2} on the reducing side is less than ~10^{-15} atm. This corresponds exactly with the onset of electronic conduction (see Figure 2-12) due to the increase in the concentration of electrons (see Figures 2-9 through 2-11). For case (b) there is always some flux except when $P_L = P_0$ because the fuel side P_{O_2} is maintained at 10^{-20} atm. where the electronic conduction is high. The flux reaches a maximum at ~10^{-12} atm. and it becomes independent of the increasing P_{O_2} on the oxidizing side for $P_{O_2} > $ ~10^{-12} atm. again coinciding with the decrease in electronic conductivity. A sign (direction) change is also observed for case (b) when the varying P_{O_2} (initially greater) falls below the value of the fixed P_{O_2} (10^{-20} atm.)—i.e., to the left of the vertical line in Figure 2-14—causing the driving force for oxygen flux, the oxygen chemical potential gradient, to reverse direction. A corresponding directional change would have been observed in case (a) when the variable P_{O_2} goes above the value of the fixed P_{O_2} (0.21 atm.), if SDC had significant hole conductivity.
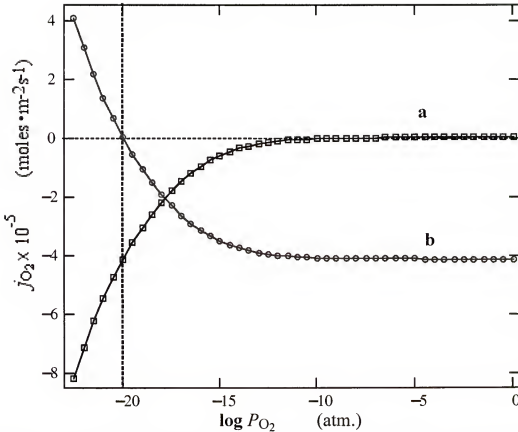
Figure 2-14. Oxygen flux, $j_{O_2}(P)$, through a 1 mm thick MIEC, keeping a constant P_{O_2} on (a) the oxidizing side (0.21 atm.) and (b) the reducing side (10^{-20} atm.) while varying the P_{O_2} on the other side of the MIEC.

2.4.4 Defect Association

Thus far the impact of defect associates in our discussion has been neglected. As the concentration of ionic defects increases, so does the likelihood of the formation of defect associates. There are numerous possible defect associates but this discussion is limited to three types because they seem to be the most likely ones [57, 58].

Oxygen vacancies in SDC form the defect associate $\left(\text{Sm}'_{\text{Ce}} \circ \text{V}^{\bullet\bullet}_{\text{O}} \circ \text{Sm}'_{\text{Ce}} \right)^{\times}$ at low temperatures [58]. At sufficiently high temperatures, oxygen vacancies have enough energy to break free from these defect associates and participate in the conduction of charge. Still, it is reported [57, 58] that (under isothermal conditions) as the total concentration of oxygen vacancies increases with decreasing P_{O_2}, so does the concentration of associated oxygen vacancies. If this is true, then it seems reasonable

therefore that those defect associates whose formation is a function of P_{O_2} are different from the variety mentioned above. Therefore, it is likely that the P_{O_2} dependent defect associates are caused by the presence of Ce'_{Ce} defects. The possible defect association reactions discussed and their corresponding mass-action relations may be summarized as follows:

$$2Sm'_{Ce} + V_O^{\bullet\bullet} \leftrightarrow \left(Sm'_{Ce} \circ V_O^{\bullet\bullet} \circ Sm'_{Ce}\right)^{\times} \qquad \Rightarrow \qquad K_1 = \frac{c_{d1}}{c_A^2 c_{V_O}} \qquad (2.4.41)$$

$$Ce'_{Ce} + Sm'_{Ce} + V_O^{\bullet\bullet} \leftrightarrow \left(Ce'_{Ce} \circ V_O^{\bullet\bullet} \circ Sm'_{Ce}\right)^{\times} \qquad \Rightarrow \qquad K_2 = \frac{c_{d2}}{c_{sp} c_A c_{V_O}} \qquad (2.4.42)$$

and

$$2Ce'_{Ce} + V_O^{\bullet\bullet} \leftrightarrow \left(Ce'_{Ce} \circ V_O^{\bullet\bullet} \circ Ce'_{Ce}\right)^{\times} \qquad \Rightarrow \qquad K_3 = \frac{c_{d3}}{c_{sp}^2 c_{V_O}} \qquad (2.4.43)$$
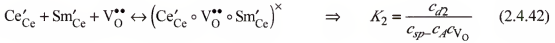
where c_{d1}, c_{d2} and c_{d3} are the concentrations of the defect associates $\left(Sm'_{Ce} \circ V_O^{\bullet\bullet} \circ Sm'_{Ce}\right)^{\times}$, $\left(Ce'_{Ce} \circ V_O^{\bullet\bullet} \circ Sm'_{Ce}\right)^{\times}$ and $\left(Ce'_{Ce} \circ V_O^{\bullet\bullet} \circ Ce'_{Ce}\right)^{\times}$ respectively. For the formation of the $\left(Sm'_{Ce} \circ V_O^{\bullet\bullet} \circ Sm'_{Ce}\right)^{\times}$ defect associate to occur, two Sm'_{Ce} defects must be present in the same unit cell. For moderate dopant concentrations ($< \sim 30\%$) the probability of having two Sm'_{Ce} defects in a unit cell is small for a well mixed (uniformly distributed) solid solution. Though the probability increases with dopant concentration typically phase segregation (and/or transformation) will occur before it becomes significant. Accordingly, the formation of the defect associate of $\left(Sm'_{Ce} \circ V_O^{\bullet\bullet} \circ Sm'_{Ce}\right)^{\times}$ is primarily dependent on the dopant concentration as evidenced by the c_A^2 term in Eq. (2.4.41). At the other end of the spectrum, the formation of the $\left(Ce'_{Ce} \circ V_O^{\bullet\bullet} \circ Ce'_{Ce}\right)^{\times}$ defect associate is dependent on the presence of small polarons, Ce'_{Ce}, in the lattice. Unlike the dopant, however, the concentration of the small polarons is dependent on P_{O_2}.

Moreover, if cations are readily available (i.e., $c_e \ll c_{cat}$) small polarons and oxygen vacancies are formed concurrently in the external equilibrium reaction (Eqs. (2.3.2) and (2.3.16)). Consequently, the likelihood of finding two Ce'_{Ce} defects in a unit cell increases as the P_{O_2} decreases. This strong dependence on P_{O_2} is evidenced by the c_{sp-}^2 term in Eq. (2.4.43). The driving force behind the formation of the $\left(Ce'_{Ce} \circ V_O^{\bullet\bullet} \circ Sm'_{Ce}\right)^\times$ defect associate falls in between these two extremes.

Combining Eqs. (2.3.2), (2.3.16) and (2.4.41) through (2.4.43) yields:

$$c_{d1} = K_1 c_A^2 c_{V_O} \tag{2.4.44}$$

$$c_{d2} = K_2 c_{sp-} c_A c_{V_O} = K_2 c_{V_O} c_e c_A \left(1 + \frac{c_e}{c_{cat}}\right)^{-1} \tag{2.4.45}$$

and

$$c_{d3} = K_3 c_{sp-}^2 c_{V_O} = K_3 c_{V_O} c_e^2 \left(1 + \frac{c_e}{c_{cat}}\right)^{-2} \tag{2.4.46}$$

Since there is one vacancy per defect associate, the sum of Eqs. (2.4.44) through (2.4.46) can be subtracted from Eq. (2.4.2) to get the reduced oxygen vacancy concentration, $c_{V_O}^{red}$, as follows:

$$\begin{aligned}
c_{V_O}^{red} &= c_{V_O} - c_{d1} - c_{d2} - c_{d3} \\
&= c_{V_O} \left[1 - K_1 c_A^2 - K_2 c_e c_A \left(1 + \frac{c_e}{c_{cat}}\right)^{-1} - K_3 c_e^2 \left(1 + \frac{c_e}{c_{cat}}\right)^{-2}\right] \tag{2.4.47}
\end{aligned}$$

Similarly, since the $\left(Ce'_{Ce} \circ V_O^{\bullet\bullet} \circ Sm'_{Ce}\right)^\times$ and $\left(Ce'_{Ce} \circ V_O^{\bullet\bullet} \circ Ce'_{Ce}\right)^\times$ defect associates have one and two small polarons respectively, the reduced small polaron concentration, c_{sp-}^{red}, is given by

$$c_{sp-}^{red} = c_{sp-} - c_{d2} - 2c_{d3} = c_{sp-}\left(1 - K_2 c_A c_{V_O} - 2K_3 c_{V_O} c_e \left(1 + \frac{c_e}{c_{cat}}\right)^{-1}\right) \qquad (2.4.48)$$

In Figures 2-15 and 2-16, $c_{V_O}^{red}$ and c_{sp-}^{red} are plotted and compared with previous results for c_{V_O} and c_{sp-} (Eqs. (2.4.2) and (2.4.4)) respectively). Presently, experimental values for K_1, K_2 and K_3 are not available. Therefore, given the constraints

$$K_1 c_A^2 + K_2 c_A c_e \left(1 + \frac{c_e}{c_{cat}}\right)^{-1} + K_3 c_e^2 \left(1 + \frac{c_e}{c_{cat}}\right)^{-2} \leq 1$$

and

$$K_2 c_A c_{V_O} + 2K_3 c_{V_O} c_e \left(1 + \frac{c_e}{c_{cat}}\right)^{-1} \leq 1$$

(i.e., $c_{V_O}^{red}$ and c_{sp-}^{red} can not be negative) the values used for K_1, K_2 and K_3, (separately in Figure 2-15 and together in Figure 2-16) were chosen to depict extreme conditions. Here extreme conditions are considered to be when the concentrations of the defect associates are plentiful but unassociated oxygen vacancies still exist. As expected, Figures 2-15a and 2-15b show that the formation of the $\left(Sm'_{Ce} \circ V_O^{\bullet\bullet} \circ Sm'_{Ce}\right)^\times$ defect associate is directly proportional to c_{V_O}, which is a consequence of its dependence on c_{V_O} and c_A. Similarly, Figures 2-15b, 2-15c and 2-16b show that c_{d2} and c_{d3} are both dependent on P_{O_2}; c_{d3} more so than c_{d2}. In these plots one observes a rapid decline in the concentration of oxygen vacancies and small polarons just outside the electrolytic region of SDC. This behaviour was observed experimentally by Schneider et al. [57] and (as mentioned earlier) is in accordance with the formulation of the corresponding defect associates. Additionally, a comparison of Figures 2-15a through 2-15c and 2-16b shows that the $\left(Sm'_{Ce} \circ V_O^{\bullet\bullet} \circ Sm'_{Ce}\right)^\times$ defect associate dominates at high P_{O_2} while the
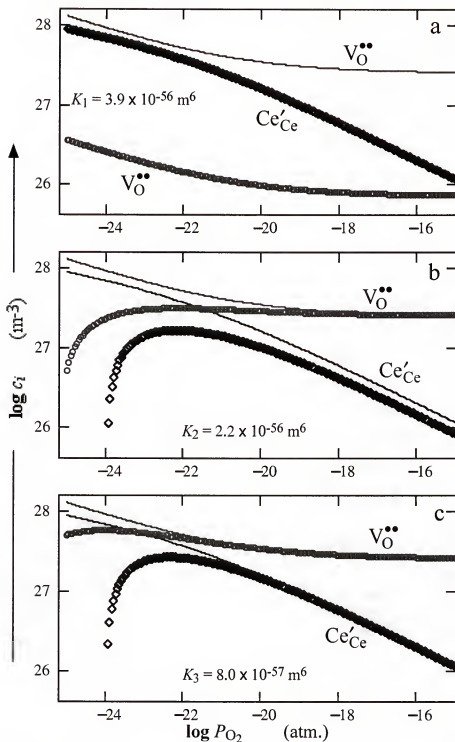
Figure 2-15. Dependence of c_{V_O} (o) and c_{sp-} (◊) on P_{O_2} with (symbols) and without (lines) the effect of defect association. Shown is the effect of the sole formation of (a) c_{d1}, (b) c_{d2} and (c) c_{d3}.
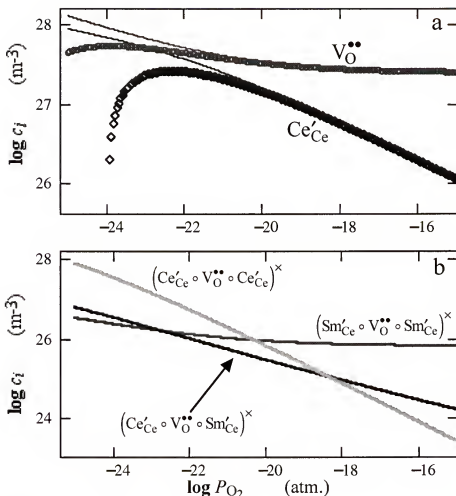
Figure 2-16. Oxygen partial pressure dependence of (a) c_{V_O} (o) and c_{sp-} ($\Diamond$) with (symbols) and without (lines) the effect of defect association and (b) c_{d1}, c_{d2} and c_{d3} for $K_1 = 10^{-57}$ m^6, $K_2 = 1.1 \times 10^{-57}$ m^6 and $K_3 = 7.6 \times 10^{-57}$ m^6.

$\left(Ce'_{Ce} \circ V^{\bullet\bullet}_O \circ Ce'_{Ce}\right)^\times$ defect associate dominates at low P_{O_2}. As discussed earlier, when all the defect associates described above are present and at moderate dopant concentrations, one may expect $c_{d1} \ll c_{d2} \ll c_{d3}$ ($K_1 < K_2 < K_3$). This is depicted in Figure 2-16a.

Figure 2-17 shows the effect of K_r on the formation of defect associates. The effective value of K_r (which is a measure of how easily oxygen is exchanged between an oxide MIEC and a gaseous environment) may be increased by dispersing fine particles of a catalytic material (such as a metal) on the surface of an oxide MIEC. In practice, this is
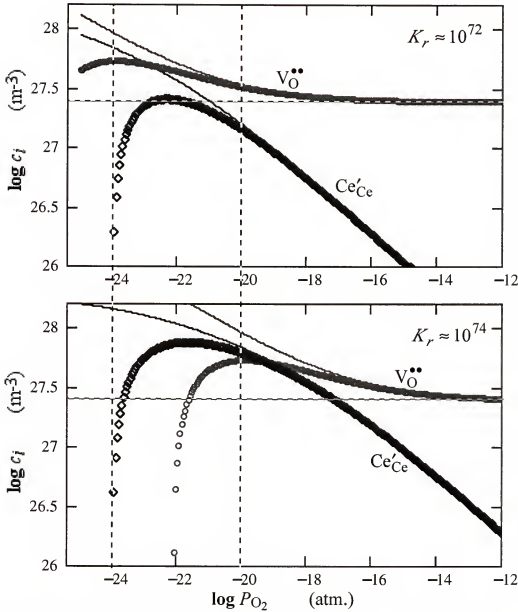
Figure 2-17. Effect of K_r on the formation of defect associates. P_{O_2} dependence of c_{V_O} (o) and c_{sp-} (◊) with (symbols) and without (lines) the effect of defect association for (a) $K_r = 10^{72}$ m^{-9}atm.$^{1/2}$ and (b) $K_r = 10^{74}$ m^{-9}atm.$^{1/2}$. In each case, $K_1 = 10^{-57}$ m^6, $K_2 = 1.1 \times 10^{-57}$ m^6 and $K_3 = 7.6 \times 10^{-57}$ m^6.

often done to enhance the oxidation rate of fuels used in SOFCs and membrane reactors. Moreover, a similar effect may arise from the presence of porous metal electrodes on an SOFC. Figure 2-17 shows that an increase in K_r results in the formation of more defects overall and more defect associates. The increase in defect associates, however, is much

greater than the net increase in defects. This is evidenced in a more rapid decline in $c_{V_O^{\cdot\cdot}}^{red}$ and c_{sp}^{red} when K_r is increased from 10^{72} m^{-9}atm.$^{1/2}$ to 10^{74} m^{-9}atm.$^{1/2}$. Thus, despite the increase in total defect concentration, the number of unassociated defects is less. As one may imagine, this result has potential ramifications on the measured properties and performance of MIECs and will be discussed in greater detail in chapter 3.

2.5 Summary

In this chapter, models were developed to describe, through analytically derived formulae, the functional dependence of defect concentration and conductivity on P_{O_2} in MIECs with the fluorite and perovskite structures. The results of models agreed with the predictions of the Brouwer approach [14] but unlike the Brouwer models there is no discontinuity between the Brouwer regimes.

To demonstrate the applicability of the models a case study was done for SDC. The accuracy of the model was confirmed through its ability to fit the numerically obtained DED for SDC as well as experimental data [49] for log σ versus log P_{O_2}. Additionally, methodologies were proposed for the determination of K_r—the most critical constant— from experiment as well as a thermodynamic argument. Subsequently, an exact, assumption free, solution to Wagner's equation [53] was provided by way of the modeled conductivity expressions. Finally, simple defect association reactions were proposed and their effect on the defect concentration was examined. The results were similar to what has been observed experimentally by other researchers [57].

CHAPTER 3
SPATIAL DISTRIBUTION AND TRANSPORT OF DEFECTS IN OXIDE MIXED
IONIC-ELECTRONIC CONDUCTORS

3.1 Introduction

In this chapter, the spatial distribution and transport of defects are modeled for MIECs in an oxygen potential gradient. The only mobile ionic defects considered are oxygen vacancies since in typical partial pressures of oxygen, P_{O_2} (~10^{-25} atm. to ~1 atm.)[14] : (a) the concentrations of oxygen interstitials are usually negligible in fluorites and (b) cation vacancies, if present, are usually immobile in perovskites. The MIECs are further divided into n-type and p-type where, for n-type MIECs

$$c_e \gg c_h$$

and, therefore

$$R_e \ll R_h$$

where c is concentration, R is electrical resistance and the subscripts "e" and "h" refer to the electrons and holes. Similarly, for p-type MIECs

$$c_h \gg c_e$$

and, therefore,

---

[14]   Typically, this P_{O_2} range corresponds to the *low* P_{O_2} region, defined in section 2.3.4, for n-type MIECs and the *intermediate* P_{O_2} region for p-type MIECs.

$$R_h \ll R_e$$

No distinction is made in this chapter between small polarons and itinerant electrons as defined in Chapter 2.

It is possible for c_e and c_h to be of comparable magnitude however this is unusual because most MIECs of interest cannot stably support both types of electronic defects. For example, the p-type MIECs based on $LaMnO_3$, $LaCoO_3$ and Bi_2O_3 become unstable and decompose at low P_{O_2} when the magnitudes of c_e and c_h approach each other. In ceria and zirconia based MIECs c_h becomes appreciable only at very high P_{O_2}, which is presently outside practical application. Consequently, MIECs usually do not display both n-type and p-type behaviour simultaneously (i.e., in the same region, see Figures 2-3 and 2-4) and so it is safe to restrict the discussion to only n-type and p-type MIECs.

This chapter also examines the effect of assuming the electric field across the MIEC is independent of position. Many researchers [41, 42, 59, 60] have made this assumption to simplify their models. However, that assumption is not necessarily true and should be made with caution.

The effect of boundary conditions is also explored. Previous researchers have assumed, again for convenience, that the boundary values of the defect concentrations are independent of an externally applied potential. In effect, they proposed that a change in the voltage across the MIEC only affects the spatial distribution of defects inside the MIEC while leaving the boundary conditions intact. This is not possible, however, since one cannot keep the activities of *all* the reacting chemical species constant while changing the potential at the interface.

Finally, the effect of defect associates is neglected in the development of the models in this chapter. This is somewhat unjustified but at this point it is unavoidable because presently there is neither consensus on the mechanism of their formation nor their prevalence. Some solace is taken in the knowledge that most other researchers also neglect

the effect of defect associates. However, that doesn't minimize its potential impact on the models.

The next section reviews previous models. That is followed by a discussion of the general equations and boundary conditions used in the development of the models. Subsequently, the spatial distribution and transport of defects are modeled for *n*-type and *p*-type MIECs. The model tries to address the concerns raised above and, hopefully, avoid any other pitfalls.

3.2   Review of Previous Models

Choudhury and Patterson. The work of Choudury and Patterson [61] is an extension of Wagner's [53] work on ambipolar diffusion in metals during oxidation. In their attempt to determine the spatial distribution and flux of defects in an MIEC, Choudhury and Patterson start out with the following version of Fick's first law:

$$\nabla \tilde{\mu}_{el} = \frac{1}{z_i \xi} \cdot \frac{\sigma_{ion}}{\sigma_{ion} - \frac{I_{ion}}{I_{el}} \sigma_{el}} \nabla \mu_{X_\xi} \tag{3.2.1}$$

where $\tilde{\mu}$ is the electrochemical potential, I is current, z is charge equivalence, σ is conductivity; μ_{X_ξ} is the chemical potential of the permeating gas, X_ξ; ξ is the number of atoms associated with the standard state of the permeating gas, X_ξ; and the subscripts "*ion*" and "*el*" refer to ionic and electronic (electrons and holes) respectively. By assuming that the ratio of the ionic and electronic currents is constant, Choudhury and Patterson derived, from their model, expressions for the steady state current supplied to an external circuit, I_{ext}, by an MIEC:

$$I_{ext} = -\frac{S}{2z_i FL} \int_{\mu_{X_2'}}^{\mu_{X_\xi}} \frac{(1+r)\sigma_{ion}\sigma_{el}}{r\sigma_{el} - \sigma_{ion}} \cdot d\mu_{X_2} \tag{3.2.3}$$

and voltage developed by the MIEC, Φ_T

$$\Phi_T = \frac{1}{2z_i F} \int_{\mu_{X_2'}}^{\mu_{X_2''}} \frac{\sigma_{ion}}{r\sigma_{el} - \sigma_{ion}} \cdot d\mu_{X_2} \qquad (3.2.2)$$

where F is Faradays constant, S is the cross-sectional area of the MIEC, L is the length of the MIEC (') and (") are superscripts referring to conditions on either side of the MIEC.

Choudhury and Patterson [61] correctly noted, that the integrals may be evaluated explicitly only if the functional dependences of σ_{ion} and σ_{el} on μ_{X_2} are known and the values of $\mu_{X_2'}$, $\mu_{X_2''}$ and r are specified. Additionally, they noted that such information was available for only a few solid electrolytes. Finally, they demonstrated the usefulness of their model by using empirically deduced dependencies for σ_{ion} and σ_{el} on P_{X_2} for typical values of $\mu_{X_2'}$, $\mu_{X_2''}$ and r. It is this need for analytically, rather than empirically, obtained functional dependences of σ_{ion} and σ_{el} on μ_{X_2} that is addressed in this chapter.

Riess. Riess [41, 59] uses a strategy similar to that of Choudhury and Patterson [61] to develop his model for the spatial distribution and flux of defects in an MIEC. Instead of developing integral equations for describing the current-voltage relations as Choudhury and Patterson [61] did, Riess [41, 59] used differential equations to derive his models for defect distribution and current-voltage relations. However, as Näfe [62] showed later, Riess' approach [41, 59] is more restrictive and less general than that of Choudhury and Patterson [61]. In fact, Näfe [62] was able to show that Riess' [41, 59] results were a special limiting case of the more general formalism derived by Choudhury and Patterson [61].

To describe the flux of ions (which, in this case, would be the oxygen vacancies), Riess [41, 59] uses the Nernst-Planck expression,

$$j_{ion} = -\frac{u_V c_V}{z_V q} \nabla \left(\mu_V^0 + k_B T \ln \frac{c_V}{c_V^0} + z_V q \phi \right) = -k_B T \frac{u_V}{z_V F} \nabla c_V - u_V c_V \nabla \phi \qquad (3.2.4)$$

where j is flux, q is the elementary charge of an electron, T is temperature, k_B is Boltzmann's constant, c is concentration, ϕ is electric potential, u is mobility and the subscript "V"[15] refers to oxygen vacancies (the ionic species). Riess [41, 59] then makes the assumption that the gradient of the chemical potential of the ions, $\nabla \cdot \mu_i$, is negligible with respect to other chemical potential gradients (which, in this case, would be the electrons or holes). However, this assumption is only valid for the electrolytic region where

$$c_h, c_e \ll c_V$$

and c_{ion} is constant. Outside the electrolytic range, and in low P_{O_2}, it has been shown conclusively (see the case study on ceria in Chapter 2, section 4) that $c_e = 2c_V$ for aliovalently doped ceria (e.g., samaria-doped or gadolinia-doped ceria) and other such MIECs. Consequently, the chemical potentials of the electrons and vacancies are comparable in magnitude in this region. Moreover, since the chemical potential for the ith defect is defined by

$$\mu_i = \mu_i^0 + k_B T \ln \frac{a_i}{a_i^{ref}} = \mu_i^0 + k_B T \ln \frac{c_i}{c_i^{ref}} \tag{3.2.5}$$

then, when $c_e = 2c_V$

$$\nabla \mu_V = k_B T \nabla \ln c_V = k_B T \nabla \ln c_e = \nabla \mu_e \tag{3.2.6}$$

Eq. (3.2.6) shows that assuming $\nabla \mu_V$ to be negligibly small, outside the electrolytic region, with respect to other (i.e., electronic) chemical potential gradients cannot be valid unless $\nabla \mu_e$ is also negligibly small. Furthermore, if $\nabla \cdot \mu_V \approx 0$, then $\nabla c_V = 0$ and c_V is

---

[15] Since oxygen vacancies are the only ionic species under consideration, the sub-subscript used in chapter 2 to identify the lattice site occupied by an ionic defect is dropped.

constant. However, c_V is not constant for aliovalently doped ceria, Riess' focus material [41, 59], in the temperature and pressure range that Riess specifies [42, 59].

Additionally, Riess [41, 59] assumes that the electric field is constant across the MIEC. In other words, Riess [41, 59] assumes that Laplace's equation

$$\nabla^2 \phi = 0 \qquad (3.2.7)$$

applies to the system. This is equivalent to assuming the electric field, $\mathcal{E}$—$\mathcal{E} = -\nabla\phi$—is constant with respect to position in a one-dimensional system and that the potential, ϕ, varies linearly with x. However, Laplace's eqn. is an approximation of the more general Poisson's equation

$$\nabla^2 \phi = -\frac{q}{\varepsilon} \sum_i z_i c_i \qquad (3.2.8)$$

where ε is the permittivity of the medium. While the assumption of local charge neutrality, given by

$$\sum_i z_i c_i \approx 0 \qquad (3.2.9)$$

is usually valid it does not necessarily imply that $\nabla^2 \phi \approx 0$ since the term q/ε may be large enough so that $\nabla^2 \phi$ cannot reasonably be approximated to zero. In other words, the presence of a small number of free charges may have a significant impact on the behaviour of the electric field. Further, discussions on these issues are provided by Liu [63] and Newman [10].

Finally, Riess [41, 59] treats the defect concentrations at the boundaries of the MIEC as independent of the voltage across the MIEC. That is to say Riess assumed that a change in the voltage across the MIEC only affects the spatial distribution of defects

inside the MIEC while the boundary conditions stay the same. This is not possible, however, since one cannot keep the activities of *all* the reacting chemical species constant while changing the potential at the interface.

Liu. Liu [63] has thus far developed the most accurate model for the spatial distribution and flux of defects in MIECs. His model neither assumes a Laplacian distribution of the electric field nor a constant distribution of ionic defects. The problems with Liu's model [63] lie in three areas. The first lies in Liu's [63] definition of the applied potential across the MIEC. Liu's [63] definition doesn't concur with the usual equivalent circuit for an MIEC in a P_{O_2} gradient. This may have been an oversight. The second area of concern regards the constants derived in his model. They are generally intractable and difficult to relate to tangible material properties. Moreover, in some cases they must be obtained from implicit equations and the constants often depended on the very transport properties Liu [63] used them to define. Consequently, Liu's equations [63] are unattractive if not impossible to use. Finally, Liu [63], like Riess [41, 59], failed to address the impact of the applied voltage on the boundary conditions.

3.3   General Equations

3.3.1 Transport Properties and Laws

In this section, definitions of relevant transport properties and transport laws, which serve as the basis for the development of the models, are given. The first transport property of interest is the conductivity of the ith species, σ_i, in the MIEC. It is defined as:

$$\sigma_i = z_i^2 q^2 \frac{D_i}{k_B T} c_i \tag{3.3.1}$$

where D is diffusivity and c is concentration. The total conductivity, σ_{tot}, of the MIEC is then the sum of all the ith conductivities, written as

$$\sigma_{tot} = \sum_i \sigma_i \qquad (3.3.2)$$

A related and useful transport property is the transference number of the kth defect species, t_k,—$k \in \{1, 2,..., i\}$, the set of i defects—which is given by:

$$t_k = \frac{\sigma_k}{\sigma_{tot}} = \frac{\sigma_k}{\sum_i \sigma_i} \qquad (3.3.3)$$

Moreover, the transference number sums to unity:

$$\sum_i t_i = 1 \qquad (3.3.4)$$

In the absence of concentration gradients, the physical meaning of the fraction of current carried by the kth defect species and Ohm's law is valid for the system. This assertion may be proved by substituting Ohm's law,

$$I_i = \frac{\Delta\Phi}{R_i} = \sigma_i S \frac{\Delta\Phi}{L} \qquad (3.3.5a)$$

into Eq. (3.3.3), where I is the current through the MIEC and $\Delta\Phi$ is the potential difference across the MIEC. This chapter, however, is concerned primarily with MIECs in which concentration gradients exist. Therefore, to relate R_i (which is not a function of position) to c_i and σ_i, the concept of an average conductivity (averaged over the total length of the MIEC) is coined. The average conductivity, $\overline{\sigma}_i$, by definition is independent of position and relates to R as follows:

$$R_i = \frac{L}{\overline{\sigma}_i S} \qquad (3.3.6)$$

Since σ_i is a function of position, the transference number will generally be a function of position as well. Therefore, at least for steady state currents that are also independent of the positional variable x, the physical meaning of the transference number no longer represents the fraction of current carried by the kth defect species [10]. Nonetheless, since it is useful to have a gauge of the dominant mode of conduction (ionic, mixed or electronic) in the MIECs, the concept of the *effective* transference number of the kth defect, $\bar{t}_k$, is invoked. This concept has been used before by other researchers [9, 42, 63, 64] and at its kernel is the idea that the *overall* conductivity of the MIEC, with respect to the ith defect, is given by the average conductivity, $\bar{\sigma}_i$, a constant (i.e., it doesn't vary with x). The *effective* transference number is defined as

$$\bar{t}_k = \frac{\bar{\sigma}_k}{\sum_i \bar{\sigma}_i} \tag{3.3.7}$$

and it sums to unity

$$\sum_i \bar{t}_i = 1 \tag{3.3.8}$$

$\bar{t}_k$ is a useful concept but it must be used carefully because average properties, if applied incautiously, may distort the physical reality. The use of $\bar{t}_k$ is reviewed specifically in its application to MIEC fuel cells in *open-circuit* conditions (to be defined later) in section 3.3.3. At that point, the source, character, tolerability and degree of possible distortions are explored.

It now becomes important to define the $\bar{\sigma}_i$ which provides the means for the definition of $\bar{t}_k$. $\bar{\sigma}_i$ may be determined by considering the electrolyte as a series arrangement of infinitesimally thin *slices* of the material of identical cross-sectional area, S. The total resistance, $R_{i_{tot}}$, of such an arrangement, for the ith defect, is given by:

$$R_{i_{tot}} = \sum_{k=1}^{N} R_{i_k} \tag{3.3.9}$$

where N is the number of slices and

$$N = L/\Delta x$$

where Δx is the average thickness of each slice.

For the ith defect, the total resistance is related to $\overline{\sigma}_i$ and is defined as

$$R_{i_{tot}} = \frac{L}{\overline{\sigma}_i S} \tag{3.3.10}$$

Similarly, the resistance of a sufficiently thin—i.e., thin enough to be represented by the local defect conductivity σ_i instead of the average conductivity, $\overline{\sigma}_i$—kth *slice* of the MIEC is

$$R_{i_k} = \frac{\Delta x}{\sigma_{i_k} S} \tag{3.3.11}$$

Combining the definitions in Eqs. (3.3.1), (3.3.10) and (3.3.11) with Eq. (3.3.9) yields

$$\frac{1}{\overline{\sigma}_i} = \sum_{k=1}^{N} \frac{1}{\sigma_{i_k}} \cdot \frac{\Delta x_k}{L} = \frac{k_B T}{z_i^2 q^2 D_i L} \sum_{k=1}^{N} \frac{1}{c_{i_k}} \cdot \Delta x_k \tag{3.3.12}$$

When N is very large—i.e., as $N \to \infty$— $\Delta x \to dx$, and Eq. (3.3.12) becomes:

$$\frac{1}{\overline{\sigma}_i} = \frac{1}{L} \int_0^L \frac{1}{\sigma_i(x)} \cdot dx = \frac{k_B T}{z_i^2 q^2 D_i L} \int_0^L \frac{1}{c_i(x)} \cdot dx \tag{3.3.13}$$

which is the definition of $\overline{\sigma}_i$ that is used in this chapter.

It is important to note that Eqs. (3.3.12) and (3.3.13) imply that $\overline{\sigma}_j$ is smaller than the smallest member of the set of k σ_i's (i.e., $\overline{\sigma}_j \leq \inf\{\sigma_{i_k}\}$)[16]. In other words, the least conductive (smallest c_i) position in the electrolyte serves as an upper bound to the magnitude of $\overline{\sigma}_j$. The significance of this point is illustrated in section 3.6 where the effects of $\Delta\Phi$ on the boundary conditions and defect transport are examined.

The transport laws relevant to this chapter are given in the next three equations. Firstly, the flux density of the ith species, j_i is given by:

$$j_i = -D_i\nabla c_i - z_i D_i c_i f\nabla\phi = -\frac{\sigma_i}{z_i^2 q^2}\nabla\tilde{\mu}_i \tag{3.3.14}$$

where $f = q/k_BT$. The electrochemical potential $\tilde{\mu}$ is given by

$$\tilde{\mu}_i = \mu_i + z_i F\phi = k_B T\ln c_i + z_i q\phi \tag{3.3.15}$$

Secondly, the current density, J, is the sum of the current density contributions of each ith defect species, J_i, and given by:

$$J = \sum_i J_i = q\sum_i z_i j_i \tag{3.3.16}$$

where

$$J_i = qz_i j_i \tag{3.3.17}$$

Finally, the material balance for the ith species may be stated as

$$\frac{\partial c_i}{\partial t} = -\nabla j_i + \Gamma_i \tag{3.3.18a}$$

---

[16] The abbreviation "inf" refers to the infimum, i.e., the greatest lower bound, or the smallest member, of a set.

where t is time and Γ_i, often referred to as *production*, is the rate of the formation of the ith species due to homogenous chemical reactions in the bulk (i.e., not at the electrode surfaces). It is assumed that the system under consideration is at steady state (i.e., $\partial c_i/\partial t = 0$) and that all chemical reactions take place at the electrode surfaces (i.e., $\Gamma_i = 0$). Consequently, Eq. (3.3.18a) reduces to:

$$\nabla j_i = 0 \qquad\qquad (3.3.18b)$$

In other words, j_i is independent of position. Accordingly, J is also independent of position since:

$$\nabla J = \nabla\left(q \sum_i z_i j_i \right) = q \sum_i z_i \nabla j_i = 0 \qquad\qquad (3.3.18c)$$

3.3.2 Current-Voltage Relationships in an SOFC or Electrocatalytic Reactor

The equivalent circuit of a fuel cell with an MIEC membrane is drawn in Figure 3-1 including the directional relationship between the defect fluxes and the distribution of the potential drops in the MIEC. In accordance with the discussion in section 3.1, it is assumed for typical MIECs in fuel cell and/or electrocatalytic applications that the defect species are limited to oxygen vacancies (the ionic species) and electrons and/or holes (the electronic species). Nonetheless, the concepts and models developed hereafter are generally applicable when other defects are present. The fuel cell will be treated as a one-dimensional system, i.e., the defect currents are considered to be flowing only along the x-axis. This approach is typical and acceptable because deviations in current from the x-coordinate may adequately be treated as a change in conductivity since they would constitute a modulation in the mean free path along the x-axis. Generally, defect motion in more than one-dimension is reserved for analysis of surface phenomena. Moreover, some of the effects of multi-dimensional currents may be absorbed by appropriate constants.
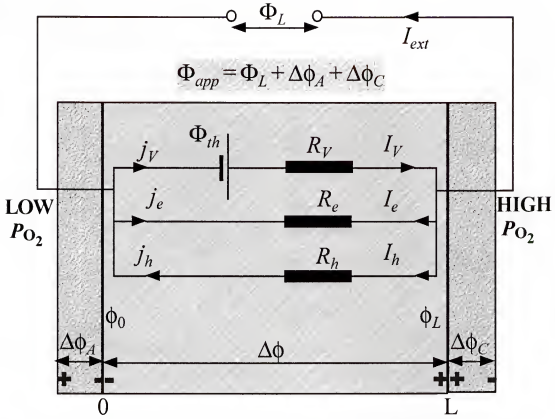
Figure 3-1. Equivalent circuit diagram of an SOFC in *closed-circuit* conditions.

For the one-dimensional system under consideration, Eq. (3.3.18) shows that J is independent of the positional variable, x. In addition, from the equivalent circuit[17], in Figure 3-1, one may deduce that

$$J = \sum_i J_i = \frac{I_{ext}}{S} \qquad (3.3.19)$$

Further circuit analysis of the fuel cell shows that

$$I_{ext} = (J_V + J_e + J_h)S = I_V + I_e + I_h = \frac{\Phi_{th} - \Phi_{app}}{R_V} - \frac{\Phi_{app}}{R_e} - \frac{\Phi_{app}}{R_h} \qquad (3.3.20)$$

---

[17] It is assumed that, except for the variable load (or power source), the resistance of the external circuit — consisting of metal wires and the load (or power source) — is much smaller than the MIEC's electronic resistance.

where Φ_{app} is the applied voltage (from the voltage drop across the load or applied by an external source), Φ_{th} is the theoretical (Nernst) voltage and the subscripts have their usual meaning. Equations (3.3.2), (3.3.6), (3.3.7), (3.3.10) and (3.3.20) may be combined to yield

$$I_{ext} = \frac{\bar{t}_{ion}\Phi_{th} - \left[1 + \left(\frac{1}{R_h} + \frac{1}{R_e}\right)R_V\right]\bar{t}_{ion}\Phi_{app}}{\bar{t}_{ion}R_V}$$

$$= \frac{\Phi_{th} - \left(\frac{1}{R_V} + \frac{1}{R_h} + \frac{1}{R_e}\right)R_V\Phi_{app}}{L}\bar{t}_{ion}S\bar{\sigma}_{tot} \tag{3.3.21}$$

and

$$\Delta\Phi = \bar{t}_{ion}\Phi_{th} - \left(\frac{1}{R_V} - \frac{1}{R_h} + \frac{1}{R_e}\right)R_V\Phi_{app}\bar{t}_{ion} \tag{3.3.22}$$

As depicted in Figure 3-1 (and in later sections), $\Delta\Phi$ is a measure of the resistance being offered by the external circuit to the electrons created by the reactions at the gas/MIEC interface. When $\Delta\Phi = 0$ and $I_{ext} = 0$ the external circuit is "open", i.e., the conductance of the external circuit is zero. Conversely, non-zero values of $\Delta\Phi$ (and I_{ext}) correspond to non-zero conductances for the external circuit and the conductance increases monotonically with the magnitude of $\Delta\Phi$ (and I_{ext}).

Finally, in concurrence with the discussion in section 3.1, the MIECs are now divided into two classes: *n*-type where electrons are the dominant electronic species and *p*-type where holes are dominant. Accordingly, *n*-type MIECs are defined by the charge balance (see Figures 2-3 and 2-4) across Regions I and IIa

$$c_A = z_V c_V + z_e c_e \tag{3.3.23}$$

where the subscript "A" refers to the fixed-valence-acceptor dopant. Similarly, p-type MIECs are defined by (see Figures 2-3 and 2-4) across Regions IIa and IIb

$$c_A = z_V c_V + z_h c_h \tag{3.3.24}$$

In n-type MIECs, $R_h \to \infty$ and Eq. (3.3.21) reduces to

$$I_{ext} = \left(\Phi_{th} - \left(\frac{R_V + R_e}{R_V R_e} \right) R_V \Phi_{app} \right) \frac{\bar{t}_{ion} \overline{\sigma}_{tot}}{L} = \frac{\bar{t}_{ion} \Phi_{th} - \Phi_{app}}{L} \overline{\sigma}_{tot} \tag{3.3.25}$$

Similarly, for p-type MIECs $R_e \to \infty$ and Eq. (3.3.21) reduces to

$$I_{ext} = \left[\Phi_{th} - \left(\frac{R_V + R_h}{R_V R_h} \right) R_V \Phi_{app} \right] \frac{\bar{t}_{ion} \overline{\sigma}_{tot}}{L} = \frac{\bar{t}_{ion} \Phi_{th} - \Phi_{app}}{L} \overline{\sigma}_{tot} \tag{3.3.26}$$

Finally, combining, Eq. (3.3.25) or (3.3.26) with Eq. (3.3.22) yields

$$\Delta \Phi = \bar{t}_{ion} \Phi_{th} - \Phi_{app} \tag{3.3.27}$$

The distinction made here between n-type and p-type MIECs, as defined earlier, is driven primarily by experimental evidence. The models developed in the later are sufficiently general to accommodate any type of MIEC. However, it is desirable, as much as possible, to represent reality.

3.3.3 *Open-circuit* Conditions and Effective Transference Number.

Eqs. (3.3.1), (3.3.2), (3.3.3) and (3.3.14) through (3.3.17) may be combined to give

$$J = -\frac{\sigma_{tot}}{q} \sum_i \frac{t_i}{z_i} \nabla \tilde{\mu}_i \tag{3.3.28}$$

By making use of Eq. (3.3.4), Eq. (3.3.28) may further be manipulated as shown to produce

$$J = -\frac{\sigma_{tot}}{q}\sum_i \frac{t_i}{z_i}\nabla\left(\tilde{\mu}_i - \frac{z_i}{z_j}\tilde{\mu}_j + \frac{z_i}{z_j}\tilde{\mu}_j\right) = -\frac{\sigma_{tot}}{q}\sum_i \frac{t_i}{z_i}\nabla\left(\tilde{\mu}_i - \frac{z_i}{z_j}\tilde{\mu}_j\right) - \frac{\sigma_{tot}}{q}\frac{\nabla\tilde{\mu}_j}{z_j} \quad (3.3.29)$$

For the MIEC system, both Eqs. (2.3.2) and (2.3.3) show that[18]

$$-\frac{1}{2}\nabla\mu_{O_2} = \nabla\mu_V - \frac{z_V}{z_{e,h}}\nabla\mu_{e,h} = \nabla\tilde{\mu}_V - \frac{z_V}{z_{e,h}}\nabla\tilde{\mu}_{e,h} \qquad (3.3.30)$$

Rewriting Eq. (3.3.29) specifically for the MIEC system under consideration—such that species i corresponds to the oxygen vacancies, species j to electrons or holes—and combining it with Eq. (3.3.30) yields

$$J = -\frac{\sigma_{tot}}{q}\sum_i \frac{t_{ion}}{z_V}\left(\nabla\tilde{\mu}_V - \frac{z_V}{z_{e,h}}\nabla\tilde{\mu}_{e,h}\right) - \frac{\sigma_{tot}\nabla\tilde{\mu}_{e,h}}{z_{e,h}q} = \frac{\sigma_{tot}t_{ion}}{2z_Vq}\nabla\mu_{O_2} - \frac{\sigma_{tot}}{z_{e,h}q}\nabla\cdot\tilde{\mu}_{e,h} \quad (3.3.31)$$

where ($t_{ion} = t_V$).

In *open-circuit* conditions $J = I_{ext} = 0$ (i.e., no net current is drawn from the MIEC), $\nabla\phi = 0$ (i.e., there is no charge build up at any point in the MIEC) and $\tilde{\mu}_i = \mu_i$. Hence, Eq. (3.3.31) may be rewritten as

---

[18] It is tacitly assumed here, and elsewhere [54], that the chemical potential of lattice oxygen, $\mu_{O_O^x}$, is constant. The present formulation of the defect equilibrium for the formation and annihilation of vacancies and electrons by the reaction of the MIEC with environmental oxygen, however, is written in terms of the 'virtual' chemical (and electrochemical) potentials of the constituent structure elements. In doing so, one does not properly take into account the so-called site exclusion effect, because the chemical potential of the oxygen vacancy, $V_O^{\bullet\bullet}$, and that of the lattice oxygen, O_O^x, cannot be defined independently from one another. In the present context, it suffices to say that the derived equations are in agreement with those obtained from a more rigorous thermodynamic treatment based upon the 'true' chemical potential for the building unit vacancy, i.e., $(V_O^{\bullet\bullet}-O_O^x)$. Further reading concerning the definition of chemical potentials, may be found in references 10 and 23.

$$2z_V \nabla \mu_{e,h} = z_{e,h} t_{ion} \nabla \mu_{O_2} \qquad (3.3.32)$$

Integrating Eq. (3.3.32) over x yields

$$2z_V \int_0^L \frac{\partial \mu_{e,h}}{\partial x} \cdot \mathrm{d}x = z_{e,h} \int_0^L t_{ion} \frac{\partial \mu_{O_2}}{\partial x} \cdot \mathrm{d}x \qquad (3.3.33)$$

By definition [10] the *open-circuit* potential across the fuel cell, Φ_{oc} (where Φ_{oc} is the value of Φ_{app} in *open-circuit* conditions), is defined as

$$\Phi_{oc} = \frac{1}{z_{e,h}q} \int_{\mu_{e,h}(x=0)}^{\mu_{e,h}(x=L)} \mathrm{d}\mu_{e,h} \qquad (3.3.34)$$

Additionally, in the development thus far, the chemical potential of the species depends only on the concentrations hence Eq. (3.3.33) becomes

$$\Phi_{oc} = \frac{1}{z_{e,h}q} \int_{\mu_{e,h}(x=0)}^{\mu_{e,h}(x=L)} \mathrm{d}\mu_{e,h} = \frac{1}{2z_V q} \int_0^L t_{ion} \frac{\mathrm{d}\mu_{O_2}}{\mathrm{d}x} \cdot \mathrm{d}x \qquad (3.3.35)$$

Eq. (3.3.35) serves as a working definition of Φ_{oc}.

To illustrate how the use of $\bar{t}_{ion}$ may distort the physical picture of how Φ_{oc} is produced, consider also that under *open-circuit* conditions, as Figure 3-1 shows, that—since $I_{ext} = 0$—$I_e = I_V = I$ (n-type) or $I_h = I_V = I$ (p-type). Therefore, in *open-circuit* conditions Eq. (3.3.7), when combined with Eq. (3.3.10), reduces to

$$\bar{t}_{ion} \equiv \bar{t}_V = \frac{\overline{\sigma}_V}{\overline{\sigma}_V + \overline{\sigma}_{e,h}} = \frac{R_{e,h}I}{R_V I + R_{e,h}I} = \frac{\Phi_{oc}}{\Phi_{th}} \qquad (3.3.36)$$

where Φ_{oc} is the *open-circuit* potential, i.e., the value of Φ_{app} in *open-circuit* conditions. (Note that this approximation is only applicable when one electronic species dominates.)

Equations (3.3.36) and (3.3.3) cannot both be correct unless they are equivalent to each other. In general, the equations concur if, and only if, $t_{ion} \equiv \bar{t}_{ion}$ (i.e., t_{ion} is independent of x) which in turn is true only in the absence of concentration gradients as discussed in section 3.3.1. Nonetheless, the use of Eq. (3.3.36) pervades the literature, irrespective of the MIEC in consideration. The primary reason for the inaccuracy of Eq. (3.3.36) is that the use of an average property, $\bar{t}_{ion}$, implies that variations in the *chemical* field is due only to $\nabla \cdot \mu_{O_2}$. It is more reasonable, however, that the topology of the field is affected by variations in the relative conductivity of the defect species. An analogy may be drawn to the way a varying frictional force modifies the work done by a body moving in a gravitational field. Similarly, to evaluate the work done by an atom vibrating in a lattice one needs to know how both the attractive and repulsive forces vary with position. Averaging either force causes a loss of information as well as a misrepresentation of the true behaviour of the atom. Accordingly, the size of the error incurred by using of Eq. (3.3.36), depends solely on how much information is lost by assuming that t_{ion} is independent of x, i.e., the extent of the concentration gradients. Nevertheless, $\bar{t}_{ion}$ is still useful as an indicator of the presence of concentration gradients in MIECs and accordingly their suitability for use as a fuel cell, but its meaning must be interpreted with care.

In rest of the chapter, the equations listed in this section are used to generate expressions for the spatial distribution of defects in n-type and p-type MIECs. First, like Riess [41, 59], it is assumed that the electric field in the MIEC is Laplacian (i.e., $\nabla^2 \phi = 0$). Subsequently, that assumption is relaxed and its effect on the spatial distribution of defects in the MIEC is explored in sections 3.7 and 3.8.

3.4. Modeling Defect Distribution and Transport in MIECs by Assuming a Linear Electric Field ($\nabla^2 \Phi = 0$): The Linear Potential Model

In this section, expressions for the spatial distribution of charges in an acceptor-doped oxide MIEC are derived by assuming that the system satisfies Laplace's equation:

$\nabla^2\phi = 0$ (i.e., the electric field $\nabla\phi$, is a constant). Those expressions are then substituted into the relevant transport equations and definitions to obtain relationships for transport properties, flux and current.

3.4.1 General Development of the Model

To obtain an expression for $c_V(x)$ Eqs. (3.3.14), (3.3.16), (3.3.17), (3.3.24) and (3.3.25) are combined to eliminate c_V with the result:

$$z_{e,h}\left(D_{e,h} - D_V\right)\nabla c_{e,h} + z_{e,h}\left(z_{e,h}D_{e,h} - z_V D_V\right)\nabla\phi\, c_{e,h} + z_V D_V c_A \nabla\phi + \frac{J}{q} = 0 \quad (3.4.1)$$

Since Eq. (3.3.18) shows that J is independent of x, and it is assumed that $\nabla\phi$ is a constant, the differential equation in Eq. (3.4.1) has the solution:

$$c_{e,h}(x) = \frac{B\exp(-\beta/\nabla\phi x) - \left(z_V D_V c_A q/\nabla\phi + J\right)}{z_{e,h}\left(z_{e,h}D_{e,h} - z_V D_V\right)q/\nabla\phi} \quad (3.4.2a)$$

where

$$\beta = \frac{z_V D_V - z_{e,h}D_{e,h}}{D_V - D_{e,h}}$$

and B is an integration constant. Applying the boundary conditions:

$$\text{at } x = 0,\ c_i = c_{i_0} \qquad \text{and} \qquad \text{at } x = L,\ c_i = c_{i_L}$$

(where $i = V, e, h$) to Eq. (3.4.2a) yields

$$c_{e,h}(x) = \frac{c_{e,h_L} - c_{e,h_0}\exp(-\beta/\nabla\phi L) - \left(c_{e,h_L} - c_{e,h_0}\right)\exp(-\beta/\nabla\phi x)}{1 - \exp(-\beta/\nabla\phi L)} \quad (3.4.2b)$$

For a Laplacian potential, $\nabla\phi$ is a constant,—see Figure 3-1—therefore $\nabla\phi = (\phi_L - \phi_0)/L$ $= -\Delta\Phi/L$ and Eq. (3.4.2) may be written as

$$c_{e,h}(x) = \frac{c_{e,h_L} - c_{e,h_0}\exp(\beta/\Delta\Phi) - \left(c_{e,h_L} - c_{e,h_0}\right)\exp\left(\beta/\frac{\Delta\Phi}{L}x\right)}{1 - \exp(\beta/\Delta\Phi)} \qquad (3.4.2c)$$

Eq. (3.4.2c) may now be substituted into Eq. (3.4.24) or (3.4.24) with the result:

$$c_V(x) = \frac{c_{V_L} - c_{V_0}\exp(\beta/\Delta\Phi) + \left(c_{V_0} - c_{V_L}\right)\exp\left(\beta/\frac{\Delta\Phi}{L}x\right)}{1 - \exp(\beta/\Delta\Phi)} \qquad (3.4.3)$$

It is noted here that the boundary values c_{i_0} and c_{i_L} ($i = V, e, h$) used in this section are set by the defect equilibrium equations for the MIEC. These boundary values are discussed in detail section 3.5.

Now that an expression for the spatial distribution of defects, $c_i(x)$, has been procured, all properties that depend on it and/or $\nabla c_i(x)$ may now be obtained. The most significant ones are derived in the remainder of this section.

Combining Eqs. (3.3.14) and (3.4.2), yields for the flux density of electronic defects:

$$j_{e,h} = \frac{D_{e,h}/\Delta\Phi\left[\left(\frac{\beta}{z_{e,h}} - 1\right)\left(c_{e,h_L} - c_{e,h_0}\right)\exp\left(\beta/\frac{\Delta\Phi}{L}x\right) + c_{e,h_L} - c_{e,h_0}\exp(\beta/\Delta\Phi)\right]}{z_{e,h}L\left[1 - \exp(\beta/\Delta\Phi)\right]} \qquad (3.4.4a)$$

It is immediately apparent that this expression suggests, in contradiction to Eq. (3.3.18), that flux is a function of position unless $z_{e,h} = \beta$ or $c_{e,h_L} = c_{e,h_0}$. However, as stated earlier, all chemical reactions are assumed to take place at the electrode surfaces (i.e., $\Gamma_i = 0$) and so flux must be independent of position. This discrepancy is a direct consequence of assuming a Laplacian potential (i.e., $\nabla\phi$ is a constant). That assumption denies the

potential the freedom to compensate for changes in the defect concentration gradients by adjusting its value. Nevertheless, the discrepancy is resolvable in the limiting case that $D_{e,h} \gg D_V$ and thereby $\beta \approx -1$ for n-type and $\beta \approx 1$ for p-type MIECs. If this is true (and fortunately it usually is), then the flux density of the electronic defects is independent of position and Eq. (3.4.4a) reduces to

$$j_{e,h} = z_{e,h} D_{e,h} f \cdot \frac{\Delta \Phi}{L} \cdot \left[\frac{c_{e,h_L} - c_{e,h_0} \exp\left(z_{e,h} / \Delta \Phi\right)}{1 - \exp\left(z_{e,h} / \Delta \Phi\right)} \right] \tag{3.4.4b}$$

Eq. (3.4.4b) may then be combined with Eqs. (3.3.14), (3.3.16), (3.3.17), (3.3.24), (3.3.25) and (3.4.2) to give

$$j_V = z_V D_V f \cdot \frac{\Delta \Phi}{L} \cdot \left[\frac{c_{V_L} - c_{V_0} \exp\left(z_{e,h} / \Delta \Phi\right)}{1 - \exp\left(z_{e,h} / \Delta \Phi\right)} \right] \tag{3.4.5}$$

To obtain the average conductivity of the MIEC, Eq. (3.4.5) is substituted into Eq. (3.3.13) which is then integrated with the result:

$$\overline{\sigma}_i = z_i^2 q D_i \beta f^2 \Delta \Phi \frac{c_{i_L} - c_{i_0} \exp(\beta / \Delta \Phi)}{\left[1 - \exp(\beta / \Delta \Phi)\right]\left(\ln \dfrac{c_{i_0}}{c_{i_L}} + \beta / \Delta \Phi \right)} \tag{3.4.6}$$

($i = V, e, h$). This expression for $\overline{\sigma}_i$ may then be substituted into Eq. (3.3.7) to obtain:

$$\overline{t}_{ion} = \left(1 + \frac{z_{e,h}^2 D_{e,h}}{z_V^2 D_V} \cdot \frac{c_{e,h_L} - c_{e,h_0} \exp(\beta / \Delta \Phi)}{c_{V_L} - c_{V_0} \exp(\beta / \Delta \Phi)} \cdot \frac{\ln \dfrac{c_{V_0}}{c_{V_L}} + \beta / \Delta \Phi}{\ln \dfrac{c_{e,h_0}}{c_{e,h_L}} + \beta / \Delta \Phi} \right)^{-1} \tag{3.4.7}$$

The equations derived in the section are sufficient to describe the transport properties of defects in *n*-type and *p*-type MIECs except for the special case of ambipolar diffusion, which is addressed in the immediately following section. Additionally, the boundary defect concentrations have yet to be discussed re their dependence on $\Delta\Phi$. This dependence is explored in section 3.5.

3.4.2 Ambipolar Diffusion in *Open-Circuit* Conditions

Defect transport in *open-circuit* conditions—$J = 0$, $\nabla\phi = 0$ ($\Delta\Phi = 0$) and $\nabla c_i \neq 0$—is crucially different, see Figure 3-2, from defect transport in *closed-circuit* conditions—$J \neq 0$ and $\nabla\phi \neq 0$. In *closed-circuit* conditions the defect mobilities are independent of each other because $J \neq 0$ and there is a net transport of charge across the MIEC. In *open-circuit* conditions, however, $J = 0$ and there is no net transport of charge across the MIEC. The absence of net charge transport implies that the charge carrying species must diffuse simultaneously in a ratio that fulfills the requirement of zero charge transport (i.e., the defect mobilities are no longer independent of each other). This phenomenon is known as ambipolar diffusion. The observed ambipolar diffusivity, D_{ambi}, in these conditions represents a compromise between the diffusion coefficient of the electronic and ionic charge carriers. Because of their different diffusion coefficients, the electronic and ionic species tend to separate thereby creating a small charge density that prevents further separation. This charge density also creates a non-uniform potential (called the diffusion potential) which acts to accelerate the typically slower diffusing ions and decelerate the typically faster diffusing electronic defects.

Therefore, for an MIEC in *open-circuit* conditions, Eqs. (3.3.14) and (3.3.18) reduce to

$$j_i = -D_{ambi}\nabla c_i \tag{3.4.8}$$

and
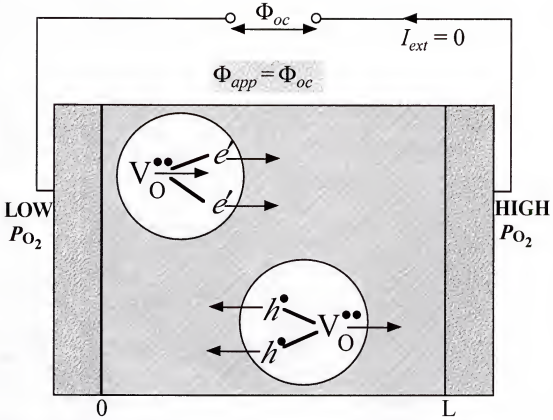
Figure 3-2. Ambipolar defect flux in an SOFC in *open-circuit* conditions.

$$\nabla j_i = 0 = -D_{ambi}\nabla^2 c_i \qquad (3.4.9)$$

Given the usual boundary conditions—at $x = 0$, $c_i = c_{i_0}$ and at $x = L$, $c_i = c_{i_L}$—then the solution of the second-order differential equation in Eq. (3.4.9) is

$$c_i(x) = \left(c_{i_L} - c_{i_0}\right)\frac{x}{L} + c_{i_0} \qquad (3.4.10)$$

In order to procure an expression for j_V in terms of the individual defect diffusivities, consider that since $J = 0$, then Eq. (3.3.14), (3.3.16) and (3.3.17) may be combined to give:

$$F\nabla\phi = -\frac{\sum_i z_i D_i \nabla c_i}{\sum_i z_i^2 D_i c_i} \qquad (3.4.11)$$

which may then be substituted back into Eq. (3.3.14) with the result

$$j_k = -D_k \nabla c_k + z_k D_k c_k \frac{\sum_i z_i D_i \nabla c_i}{\sum_i z_i^2 D_i c_i} = \frac{D_k \nabla c_k \sum_{i \neq k} z_i^2 D_i c_i + z_k D_k c_k \sum_{i \neq k} z_i D_i \nabla c_i}{\sum_i z_i^2 D_i c_i} \quad (3.4.12)$$

Eq. (3.4.12) may be combined with Eq. (3.3.24) and written for the flux of oxygen vacancies, with the result

$$j_V = \frac{z_V z_{e,h} D_V D_{e,h} c_V \nabla c_{e,h} - z_{e,h}^2 D_V D_{e,h} c_{e,h} \nabla c_V}{z_V^2 D_V c_V + z_{e,h}^2 D_{e,h} c_{e,h}} = -\frac{\left(z_V^2 c_V + c_{e,h}\right) D_V D_{e,h}}{z_V^2 D_V c_V + D_{e,h} c_{e,h}} \nabla c_V \quad (3.4.13)$$

Obtaining an expression for j_V in the steady state (i.e., where j_V is a constant, independent of time and position) requires the integration of Eq. (3.4.13)

$$\int_0^L j_V \cdot dx = -D_V D_{e,h} \int_{c_{V_0}}^{c_{V_L}} \frac{z_{e,h}^2 c_{e,h} + z_V^2 c_V}{z_V^2 D_V c_V + z_{e,h}^2 D_{e,h} c_{e,h}} \cdot dc_V$$

which yields

$$j_V = \frac{D_V D_{e,h}}{L} \left[\frac{\left(z_V - z_{e,h}\right)\left(c_{V_0} - c_{V_L}\right)}{z_V D_V - z_{e,h} D_{e,h}} + \frac{z_{e,h}\left(D_{e,h} - D_V\right) c_A}{\left(z_V D_V - z_{e,h} D_{e,h}\right)^2} \ln \frac{z_V^2 D_V c_{V_L} + D_{e,h} c_{e,h_L}}{z_V^2 D_V c_{V_0} + D_{e,h} c_{e,h_0}} \right] \quad (3.4.14)$$

Finally, there is no ambipolar conductivity since the defects are diffusing interdependently as electrically neutral *packets* consisting of one oxygen vacancy and two electronic defects (small polarons) moving in concert. (These *packets* are equivalent to oxygen atoms diffusing through the MIEC.) Thus, there is no true electrical conductivity under *open-circuit* conditions since there is no transport of charged species. Therefore, to obtain an *equivalent* conductivity of the individual species must be treated as if they are

diffusing with their intrinsic diffusion coefficients (i.e., D_V, D_e, and D_h) rather than D_{ambi}. Therefore, substituting, Eq. (3.4.10) into Eq. (3.3.13) and integrating yields, for the average conductivity,

$$\overline{\sigma}_i = z_i^2 q f D_i \cdot \frac{c_{i_L} - c_{i_0}}{\ln c_{i_L} - \ln c_{i_0}} \qquad (3.4.15)$$

which may be substituted into Eqs. (3.3.7) with the result:

$$\overline{t}_{ion} = \left(1 + \frac{2z_{e,h}^2 D_{e,h}}{z_V^2 D_V} \cdot \frac{\ln c_{V_L} - \ln c_{V_0}}{\ln c_{e,h_L} - \ln c_{e,h_0}}\right)^{-1} \qquad (3.4.16)$$

Please note that Eqs. (3.4.10), (3.4.15) and (3.4.16) could also be derived directly from Eqs. (3.4.4), (3.4.6) and (3.4.7) by considering that for small $\Delta\Phi$ (i.e., as $\Delta\Phi \to 0$) the following equality holds: $\exp(y) \approx 1 + y$, for $0 < |y| \ll 1$.

At the risk of stating the obvious, the expressions derived above for the spatial distribution and fluxes of defects in *open-circuit* conditions do not rely on the assumption of a constant electric field (i.e., that Laplace's equation applies to the system). Hence they are generally applicable and are not re-derived in section 3.7 when the spatial distribution of defects in MIECs is modeled without assuming a constant electric field.

3.4.3 Estimating the Magnitude of the Equilibrium Constants K_r and K_m

Combining Eqs. (3.3.1), (3.3.3), (3.3.30) and (3.3.35) and integrating yields

$$\Phi_{oc} = -\frac{k_B T}{z_V q}\left\{\frac{1 - z_V^2 \Theta}{1 - z_{e,h} z_V \Theta} \ln \frac{c_{V_L} + \Theta c_{e,h_L}}{c_{V_0} + \Theta c_{e,h_0}} - \frac{z_V}{z_{e,h}} \ln \frac{c_{e,h_L}}{c_{e,h_0}}\right\} \qquad (3.4.17)$$

where

Table 3-1. Calculated values of Θ and K_r for SDC from the *corrected* Φ_{oc} data of Gödickemeier *et al.* [44, 45].

$\Theta = D_e/4D_V$	K_r (m^{-9}atm.$^{1/2}$) (from Eq. (3.4.17))	K_r (m^{-9}atm.$^{1/2}$) (from Eq. (2.4.18))
0.1	n.a.	8.7×10^{74}
1	6.6×10^{75}	2.1×10^{74}
10	8.1×10^{72}	5.5×10^{72}
24.4	1.2×10^{72}	1×10^{72} *
26.4	1×10^{72}†	8.5×10^{71}
100	6.5×10^{70}	6.2×10^{70}
1000	6.4×10^{68}	6.3×10^{68}

† K_r calculated from thermogravimetric data of Kobayashi *et al.* [47] in section 2.4.2.3

$$\Theta = \frac{z_{e,h}^2 D_{e,h}}{z_V^2 D_V}$$

The form of this equation is very similar to Eq. (2.4.18), and can likewise be used to determine K_r (as in Table 3-1) K_m or other external equilibrium constants as a function of D_e (or Θ) for given environmental conditions (e.g., P_L, P_0, T, etc.). The advantage of using Eq. (3.4.17) rather Eq. (2.4.18) is that Eq. (3.4.17) was derived from $c_i(x)$ instead of $c_i(P_{O_2})$. Eq. (3.4.17) comes from an exact solution of the transport equations in *open-circuit* conditions while Eq. (2.4.18) is a modeled approximation. Hence, there is no error introduced by way of simplifying assumptions in Eq. (3.4.17). Additionally, in suitable environmental conditions (i.e., values of P_L and P_0 that are far from the junctures of the Brouwer [14] regions for a given temperature) the boundary defect concentrations may be obtained using the familiar Brouwer approach [14]. Otherwise, the models developed in Chapter 2 may be used to determine said boundary defect concentrations. Accordingly, Table 3-1, which is essentially a repeat of Table 2-7, shows K_r calculated from Eq. (3.4.17) instead of Eq. (2.4.18) for various values of Θ. As before, the experimental data

(Φ_{oc}, P_L, P_0, T) of Gödickemeier *et al.* [44, 45] for a samaria-doped ceria (SDC) fuel cell, described in section 2.4.2.2, is used in the calculations.

Table 3-1 shows that, for a given $\Theta \geq 1$, the K_r values calculated using Eq. (3.4.17) or Eq. (2.4.18) are very close. For $\Theta \leq 1$ no unique value of K_r is computable from Eq. (3.4.17). Physically, that is a good result since it implies that, for $\Theta \leq 1$ (i.e., $D_e \leq 4D_V$), the main reason $\Phi_{oc} < \Phi_{th}$ (i.e., $\Phi_{oc}/\Phi_{th} < 1$) is the presence of the ionic defect concentration gradient. Finally, the K_r values calculated from Eq. (3.4.17) are always greater than those from Eq. (2.4.18). This trend likely indicates that there is an underestimation of the oxygen vacancy concentration gradient in Eq. (2.4.18), since the difference between the values gets smaller as Θ increases (i.e., as the effect of D_e on Φ_{oc} becomes more significant than the oxygen vacancy concentration gradient).

3.5. Boundary Conditions: Defect Concentrations at the Boundaries

3.5.1 Expressions for the Defect Concentrations at the Boundaries

In this section the boundary conditions that are applicable to MIECs in P_{O_2} gradients are discussed. If the effects of the double layer at the electrode-electrolyte interface may be ignored, then the boundary values of the defect concentrations are set by a combination of the charge balance and the defect equilibrium equation that governs the oxide's equilibrium with the gas phase. For example, c_{V_0}, c_{V_L}, c_{e_0} and c_{e_L}, for n-type MIECs, are set by a combination Eq. (3.3.23) and, in the *low* P_{O_2} region (as defined in section 2.3.4), the defect equilibrium equation:

$$\text{O}_\text{O}^\times \leftrightarrow \text{V}_\text{O}^{\bullet\bullet} + 2e' + \tfrac{1}{2}\text{O}_2 \qquad \Rightarrow \qquad K_r = c_V c_e^2 P^{\frac{1}{2}} \qquad (3.5.1)$$

where K_r is the mass action constant for the reaction. However, from Chapter 2

$$c_V(P) = \left[\tfrac{3}{4} K_r^{\frac{1}{2}} P^{-\frac{1}{4}} + \left(\tfrac{1}{2} c_A \right)^{\frac{3}{2}} \right]^{\frac{2}{3}} \qquad (3.5.2)$$

and

$$c_e(P) = K_r^{\frac{1}{2}} P^{-\frac{1}{4}} \left[\frac{3}{4} K_r^{\frac{1}{2}} P^{-\frac{1}{4}} + \left(\frac{1}{2} c_A \right)^{\frac{3}{2}} \right]^{-\frac{1}{3}} \tag{3.5.3}$$

For p-type MIECs c_{V_0}, c_{V_L}, c_{h_0} and c_{h_L} are set by a combination Eq. (3.3.24) and, in the *intermediate* P_{O_2} region (see section 2.3.4), the defect equilibrium equation:

$$\frac{1}{2}O_2 + V_O^{\bullet\bullet} \leftrightarrow O_O^\times + 2h^\bullet \qquad \Rightarrow \qquad K_m = c_V^{-1} c_h^2 P^{-\frac{1}{2}} \tag{3.5.4}$$

where K_m is the mass action constant for the reaction. Again, from Chapter 2

$$c_V(P) = \frac{1}{16} \left[\left(K_m P^{\frac{1}{2}} + 8c_A \right)^{\frac{1}{2}} - K_m^{\frac{1}{2}} P^{\frac{1}{4}} \right]^2 \tag{3.5.5}$$

and

$$c_h(P) = \frac{1}{4} \left(-K_m P^{\frac{1}{2}} + \sqrt{8c_A K_m P^{\frac{1}{2}} + K_m^2 P} \right) \tag{3.5.6}$$

Therefore, c_{i_0} and c_{i_L} ($i = V, e, h$) may be evaluated from Eqs. (3.5.2), (3.5.3), (3.5.5) and (3.5.6) by substituting appropriate values of K_r, K_m and P_{O_2} at $x = 0$ and $x = L$ respectively.

3.5.2 Effect of Potential Difference on External Equilibrium Constants

Earlier models [41, 42, 59, 63] treated the defect concentration boundary values as independent of Φ_{app}. In other words, those models (tacitly) assumed that the activities/concentrations of all the reacting chemical species at the interface are independent of the potential at the interface. That is incorrect. On the contrary, the
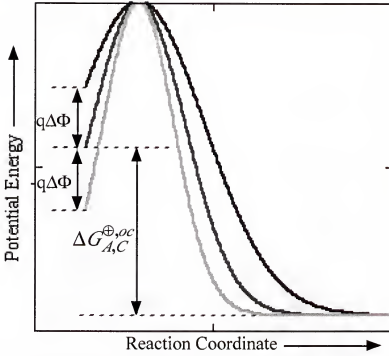
Figure 3-3. Effect of $\Delta\Phi$ on the reaction profile of the external equilibrium reaction between an MIEC and a gas phase.

activities (and therefore concentrations) of a chemical species in an electrochemical cell are controlled by the potential at the interface [10, 48, 65 - 67].

In the presence of an electric field, the total free energy of activation for an electrochemical reaction, $\Delta G^{\oplus}$, is equal to the sum of the chemical free energy of activation, $\Delta G^{\oplus,oc}$ (which occurs at *open-circuit*) and the electrical contribution due to $\Delta\Phi$, see Figure 3-3. Therefore, when an electric potential is applied to the electrode surface of the MIEC, $\Delta G^{\oplus}$ is given by

$$\Delta G_C^{\oplus} = \Delta G_C^{\oplus,oc} - z_{e,h}\alpha q\Delta\Phi \tag{3.5.7}$$

for the cathodic (anodic with respect to holes) reaction and for the anodic reaction (cathodic with respect to holes)

$$\Delta G_A^{\oplus} = \Delta G_A^{\oplus,oc} + z_{e,h}(1-\alpha)q\Delta\Phi \tag{3.5.8}$$

where the superscript "*oc*" refers to *open-circuit* conditions; the subscripts "C" and "A" refer to anodic and cathodic reactions. An anodic reaction may be defined as one that produces an electron, while a cathodic reaction may be defined as one that consumes an electron. In principle both types of reactions occur at the anode and at the cathode. However, as the system departs from equilibrium one or the other reaction becomes more favourable. α is the (apparent) transfer coefficient or symmetry factor and it reports the location of the transition state for the reaction with respect to the outer Helmholtz plane and the inner Helmholtz plane of the double layer [10, 48, 65 - 67]. A more detailed discussion of α is provided by References 10, 48 and 65 - 67. The term $z_{e,h}$ is included in the Eqs. (3.5.7) and (3.5.8) because the way $\Delta\Phi$ interacts with $\Delta G^{\oplus,oc}$ depends the type of electronic charge carriers available (i.e., holes or electrons).

Generally, the rate constant, κ, for an electrochemical reaction is given by

$$\kappa = \kappa^* \exp\left(-\frac{\Delta G}{kT}\right) \qquad (3.5.9)$$

It is in turn related to the equilibrium constant for the reaction, K,—combining Eqs. (3.5.7) through (3.5.9)—as follows

$$K = \frac{\kappa_A}{\kappa_C} = \frac{\kappa_A^* \exp\left(-\dfrac{\Delta G_A^{\oplus}}{kT}\right)}{\kappa_C^* \exp\left(-\dfrac{\Delta G_C^{\oplus}}{kT}\right)} = K^* \exp\left(-\frac{\Delta G_{\text{eq}}^{\oplus,oc} + z_{e,h}q\Delta\Phi}{kT}\right) \qquad (3.5.10a)$$

where

$$K^* = \frac{\kappa_A^*}{\kappa_C^*}$$

and

$$\Delta G_{eq}^{\oplus,oc} = \Delta G_A^{\oplus} - \Delta G_C^{\oplus}$$

and $\Delta G_{eq}^{\oplus,oc}$ is the equilibrium free energy for the reaction. Finally, by making use of Eqs. (3.5.1) and/or (3.5.4), Eq. (3.5.10a) may be rewritten as

$$\Delta \Phi = -\frac{kT \ln \dfrac{K}{K^{*}} + \Delta G_{eq}^{\oplus,oc}}{z_{e,h} q} = -\frac{1}{z_{e,h} q} \left(2\mu_e + \mu_V - \mu_{O_O^\times} - 2\mu_e^{oc} - \mu_V^{oc} + \mu_{O_O^\times}^{oc} \right) \quad (3.5.10b)$$

which shows that $\Delta\Phi$ is nothing more than the surface overpotential [10] for the MIEC.

Applying Eq. (3.5.10) to Eqs. (3.5.1) and (3.5.4) and then substituting in Eq. (3.3.28) yields

$$K_r(\Delta\Phi) = K_r^{*} \exp\left(-\frac{\Delta G_r \pm z_e q \Delta\Phi}{kT} \right) = K_r^{*} \exp\left(-\frac{\Delta G_r \pm z_e q \left(\bar{t}_{ion} \Phi_{th} - \Phi_{app} \right)}{kT} \right) \quad (3.5.11)$$

and

$$K_m(\Delta\Phi) = K_m^{*} \exp\left(-\frac{\Delta G_m \pm z_h q \Delta\Phi}{kT} \right) = K_m^{*} \exp\left(-\frac{\Delta G_m \pm z_h q \left(\bar{t}_{ion} \Phi_{th} - \Phi_{app} \right)}{kT} \right) \quad (3.5.12)$$

where ΔG_r and ΔG_m are the equilibrium free energies for the reactions in Eqs. (3.5.1) and (3.5.4) respectively, and K_r^{*} and K_m^{*} are unit bearing pre-exponential factors. Substituting Eq. (3.5.11) into Eqs. (3.5.2) and (3.5.3) gives, for n-type MIECs,

$$c_V(\Delta\Phi) = \left[\frac{3}{4} \left(K_r^{*} \right)^{\frac{1}{2}} \exp\left(-\frac{\Delta G_r \pm z_e q \Delta\Phi}{2kT} \right) P^{-\frac{1}{4}} + \left(\frac{1}{2} c_A \right)^{\frac{3}{2}} \right]^{\frac{2}{3}} \quad (3.5.13)$$

and

$$c_e(\Delta\Phi) = \frac{\left(K_r^*\right)^{\frac{1}{2}}}{P^{\frac{1}{4}}} \exp\left(-\frac{\Delta G_r \pm z_e q\Delta\Phi}{2kT}\right) \left[\frac{3\left(K_r^*\right)^{\frac{1}{2}}}{4P^{\frac{1}{4}}} \exp\left(-\frac{\Delta G_r \pm z_e q\Delta\Phi}{2kT}\right) + \left(\frac{c_A}{2}\right)^{\frac{3}{2}}\right]^{-\frac{1}{3}} \quad (3.5.14)$$

Similarly, substituting Eq. (3.5.12) into Eqs. (3.5.5) and (3.5.6) gives, for p-type MIECs,

$$c_V(P) = \frac{K_m^*}{16}\left[\left(P^{\frac{1}{2}}\exp\left(-\frac{\Delta G_m \pm z_h q\Delta\Phi}{kT}\right) + \frac{8c_A}{K_m^*}\right)^{\frac{1}{2}} - P^{\frac{1}{4}}\exp\left(-\frac{\Delta G_m \pm z_h q\Delta\Phi}{2kT}\right)\right]^2 \quad (3.5.15)$$

and

$$c_h(P) = \frac{K_m^*}{4}\exp\left(-\frac{\Delta G_m \pm z_h q\Delta\Phi}{kT}\right)\left(\sqrt{\frac{8c_A}{K_m^*}\exp\left(\frac{\Delta G_m \pm z_h q\Delta\Phi}{kT}\right)P^{\frac{1}{2}} + P} - P^{\frac{1}{2}}\right) \quad (3.5.16)$$

The "$\pm$" term is used since the term $z_{e,h}q\Delta\Phi$ adds to, or subtracts from, $\Delta G_{r,m}$ depending on the sign of $\Delta\Phi$ (i.e., the direction of the potential drop) at the interface. When $\Delta\Phi > 0$, electrons are being injected into the interface at $x = 0$, thereby increasing c_e at that interface. Therefore, if P_0 remains constant and c_V is constrained by the charge balance in Eq. (3.3.24), then according to Eq. (3.5.1), K_r must increase. Mathematically this is interpreted as $z_{e,h}q\Delta\Phi$ adding to ΔG_r. Conversely, if P_L remains constant, at $x = L$, $z_{e,h}q\Delta\Phi$ subtracts from ΔG_r when $\Delta\Phi > 0$ because electrons are being consumed (i.e., a decrease in c_e causes c_V and K_r to decrease as well) from that interface. The opposite (carried by the term $z_{e,h}$) trend is observed in p-type MIECs since an injection of electrons corresponds to a decrease in holes (see Eq. 2.3.1). According to Eqs. (3.3.25) and (3.5.4), a decrease in c_h causes an increase in c_V and a decrease in K_m. Consequently, when $\Delta\Phi > 0$, $z_{e,h}q\Delta\Phi$ subtracts from ΔG_m at $x = 0$ and $z_{e,h}q\Delta\Phi$ adds to ΔG_m at $x = L$.

The difference in the way $z_{e,h}q\Delta\Phi$ affects ΔG_r and ΔG_m is further justified by considering Eq. (2.3.22)

$$K_m K_r = K_i^2$$

which shows that if $\Delta\Phi$ is adjusted so that K_r increases for any MIEC then K_m must decrease since K_i does not change[19] (i.e., K_r is inversely proportional to K_m). This argument holds for n-type and p-type MIECs—despite the dominance of one electronic defect and one external equilibrium reaction—because they possess both electronic species and both external equilibrium reactions are possible. Consequently, the impact of $\Delta\Phi$ on n-type MIECs is opposite to p-type MIECs because they are dominated by different equilibria.

Finally, substituting Eqs. (3.5.2), (3.5.3) and (3.5.11)—for n-type MIECs—or (3.5.5), (3.5.6) and (3.5.12)—for p-type MIECs—into Eq. (3.4.7) results in an implicit expression (i.e., $\bar{t}_{ion}$ becomes a function of itself). To circumvent this problem, the spatial distribution and flux of defects are plotted for various values of $\Delta\Phi$ rather than Φ_{app}. Effectively, this allows $K_{r,m}$ to be calculated without first knowing $\bar{t}_{ion}$. $\bar{t}_{ion}$ may then be calculated, from Eqs. (3.4.7) for each $\Delta\Phi$. Finally, each $\bar{t}_{ion}$ calculated in this way may be substituted into Eq. (3.3.28) to determine the corresponding value of Φ_{app}. The results of this procedure are tabulated in Table 3-2 for n-type and p-type MIECs described in the following section. Of course, this procedure is required only if the boundary defect concentrations are considered to be dependent on $\Delta\Phi$. Otherwise, $K_{r,m}$, c_{i_0} and c_{i_L} are constants and the expression for $\bar{t}_{ion}$ is explicit. And $\bar{t}_{ion}$ (as well as the other transport properties) may be calculated as a function of Φ_{app} directly.

3.6. Results and Discussion for the Linear Potential Model

In this section, the results obtained in sections 3.4 and 3.5 for the spatial distribution, conductivity, transference number and flux of defects are plotted for n-type and p-type

---

19   K_i is determined solely by the size of the band gap in the MIEC hence it is independent of Φ_{app}.

Table 3-2. Calculated values of K_r, K_m, $\bar{t}_{ion}$, and Φ_{app} for n-type (SDC) and p-type (ESB) MIECs.

	$\Delta\Phi$ (V)	K_r (m^{-9}atm.$^{1/2}$),		$\bar{t}_{ion}$	Φ_{app} (V)
		$x = 0$	$x = L$		
n-Type	$2\Phi_{th}$	4.6×10^{81}	2.2×10^{62}	1.000	$-\Phi_{th}$
$P_0 = 10^{-20}$ atm.,	Φ_{th}	6.7×10^{76}	1.5×10^{67}	0.999	~ 0
$M = 5 \times 10^{27}$ m^{-3},	0	1.0×10^{72}	1.0×10^{72}	n.a.	Φ_{oc}
$\Phi_{th} = 1.028$ V	$-\Phi_{th}$	1.5×10^{67}	6.7×10^{76}	0.949	$\sim 2\Phi_{th}$
	$-3\Phi_{th}$	3.2×10^{57}	3.1×10^{86}	1.000	$4\Phi_{th}$
		K_m (m^{-3}atm.$^{-1/2}$)			
		$x = 0$	$x = L$		
p-Type	$2\Phi_{th}$	6.9×10^{16}	1.4×10^{30}	1.000	$-\Phi_{th}$
$P_0 = 10^{-13}$ atm.,	Φ_{th}	1.5×10^{20}	6.8×10^{26}	0.998	~ 0
$M = 22 \times 10^{27}$ m^{-3},	0	3.2×10^{23}	3.2×10^{23}	n.a.	Φ_{oc}
$\Phi_{th} = 0.709$ V	$-\Phi_{th}$	6.8×10^{26}	1.5×10^{20}	0.998	$2\Phi_{th}$
	$-3\Phi_{th}$	3.1×10^{33}	3.2×10^{13}	1.000	$4\Phi_{th}$

MIECs. Samaria-doped ceria and erbia-stabilized bismuth oxide (ESB) were chosen as representative n-type and p-type MIECs because they are candidate materials for use as electrolytes in solid oxide fuel cells (SOFCs) and electrocatalytic reactors. Likewise, while the effect of $\Delta\Phi$ on the transport properties of an MIEC, is primarily a concern for fuel cell and electrocatalytic reactor applications. Mixed ionic-electronic conductors used as gas separation membranes (such as LSCF) are typically operated in *open-circuit* conditions only.

For the plots generated in this section, values of $D_V = 4.3 \times 10^{-12}$ m^{2}V^{-1}s^{-1}—obtained from Arrhenius conductivity plots of Eguchi *et al.* [49]—and $K_r(\Delta\Phi = 0) = 9.97 \times 10^{71}$ m^{-9}atm.$^{1/2}$—from fitting the thermogravimetric data of Kobayashi *et al.* [47] in section 2.4.2.3—were used when applying the model to SDC. Substituting these values into Eq.

(3.4.17) gives $D_e = 4.5 \times 10^{-10}$ m^{2}V^{-1}s^{-1} ($\Theta = 26.4$ and $\beta = -1.029$). In addition, it is assumed that $D_I(\text{SDC}) \approx D_I(\text{ESB})$ and $D_e(\text{SDC}) \approx D_h(\text{ESB})$. Substituting these values into Eq. (3.4.17), (3.5.5) and (3.5.6) yields $K_m(\Delta\Phi = 0) = 3.2 \times 10^{23}$ m^{-3}atm.$^{-1/2}$, given $\Phi_{oc}/\Phi_{th} \approx 0.974$ [68, 69]. From data on the lattice parameter of SDC [29] and ESB [68, 69], c_A was calculated to be 5×10^{27} m^{-3} and[20] 22×10^{27} m^{-3} respectively. The environmental conditions for the SOFCs are $T = 1073$ K, $P_L = 0.21$ atm., and for SDC $P_0 = 10^{-20}$ atm., while for ESB and $P_0 = 10^{-13}$ atm.

Previously, the term "*open-circuit*" has been used to describe the state of an MIEC in a P_{O_2} gradient from which no current is being drawn. Other useful terminology for the state of the SOFC is now defined. When $\Phi_{app} = 0$ ($\Delta\Phi = \Phi_{th}$), it implies that the load (i.e., external) resistance (see Figure 3-1) is zero and the SOFC is operating in *short-circuit* conditions. As before, $\Phi_{app} = \Phi_{oc}$ ($\Delta\Phi = 0$) suggests the load resistance is infinitely large ($I_{ext} = 0$) and the SOFC is operating in *open-circuit* conditions. Instances where $\Phi_{app} > \Phi_{oc}$ ($\Delta\Phi < 0$) will be defined as *reverse biased* conditions (i.e., where an external power source is applied to change the magnitude and direction of the defect concentration gradients from that imposed by the values of P_0 and P_L alone). Finally, instances where $\Phi_{app} < 0$ ($\Delta\Phi > \Phi_{th}$) will be defined as *forward biased* conditions (i.e., where an external power source is applied to change the magnitude but not the direction of the defect concentration gradients imposed by the values of P_0 and P_L alone). In *forward* or *reverse bias* the MIEC functions as an electrocatalytic reactor while for $0 < \Phi_{app} < \Phi_{oc}$ the MIEC functions as a fuel cell.

3.6.1 Spatial Distribution of Defects: Defect Concentration Profiles

Figures 3-4 through 3-7 show normalized concentration profiles with *fixed* boundary defect concentrations (BDCs). *Fixed* BDCs imply that K_r and K_m are independent of $\Delta\Phi$ and maintain values corresponding to $K_r(\Delta\Phi = 0)$ and $K_m(\Delta\Phi = 0)$. *Fixed* BDCs further

---

[20]   For ESB the erbium and bismuth cations are treated as aliovalent acceptor "dopants" sitting in a fluorite lattice [70]. A formal development of this approach is presented in Appendix C.
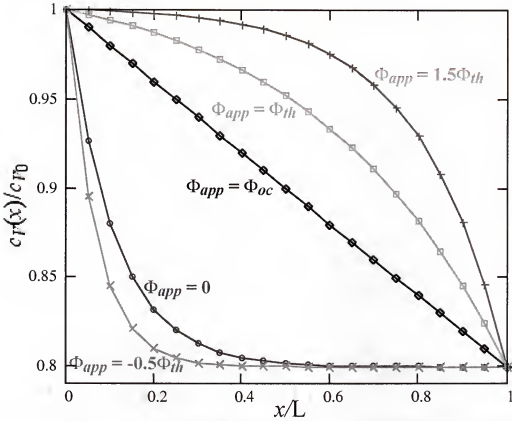
Figure 3-4. Oxygen vacancy concentration profiles in an *n*-type MIEC (SDC) with *fixed* BDCs.

imply that $\Delta\Phi$ is controlling the defect concentrations inside the MIEC, but not at the surface. When *fixed* BDCs are assumed the spatial distribution of defects (and all other transport properties) may be obtained directly from Φ_{app} instead of using $\Delta\Phi$ in the fashion outlined in section 3.5.2.

It is evident from both sets of curves that the concentration profiles are strongly influenced by the operating conditions, i.e., Φ_{app} (or $\Delta\Phi$). Figures 3-5 and 3-7 are similar to those produced by Riess [41, 59] except that here a flat vacancy distribution has not been assumed explicitly. Riess [41, 59] predicts a non-linear distribution of electrons and holes in *open-circuit* conditions (i.e., $\nabla\cdot\phi = 0$, $\Phi_{app} = \Phi_{oc}$). This is incorrect, however, since linear defect concentration gradients arise because $\nabla\cdot\phi = 0$ (see section 3.4.1) under *open-circuit* conditions. It is important to emphasize that this outcome is not due to any simplifying assumption, but is a direct consequence of the fundamental laws of charge
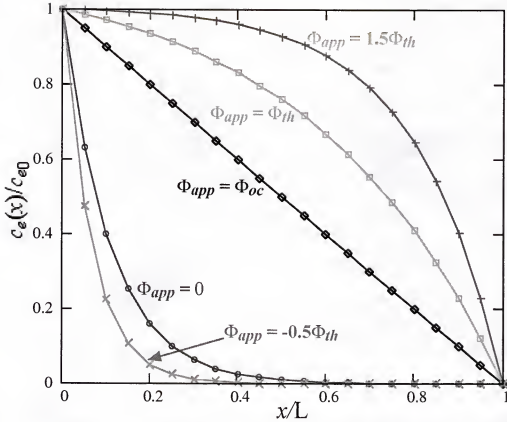
Figure 3-5. Electron concentration profiles in an *n*-type MIEC (SDC) with *fixed* BDCs.

transport as given in Eqs. (3.3.14) through (3.3.18). Liu [63] also produces plots somewhat similar to those in Figures 3-4 and 3-5. However, for *open-circuit* conditions Liu obtains a non-linear vacancy distribution and a linear electron distribution. As with Riess' [41, 59] results, this violates the fundamental transport laws since a non-linear vacancy distribution in *open-circuit* conditions—$J = 0$, $\nabla \phi = 0$—implies $\nabla j_V \neq 0$.

A comparison of Figures 3-4 and 3-5 to Figures 3-6 and 3-7 shows a few differences in the concentration profiles for *n*-type and *p*-type MIECs. First, in accordance with the defect equilibria (see Figures 2-3 and 2-4), the concentrations of oxygen vacancies and electrons are greater at P_0 (low P_{O_2}) than P_L (high P_{O_2}) while the converse is true for the hole concentration. Also, in accordance with the defect equilibria (see Figures 2-3 and 2-4), the oxygen vacancy concentration profiles in *forward* bias are *concave* for the *n*-type and *convex* for the *p*-type MIEC. The trends are reversed for *reverse* bias. In fact, as one
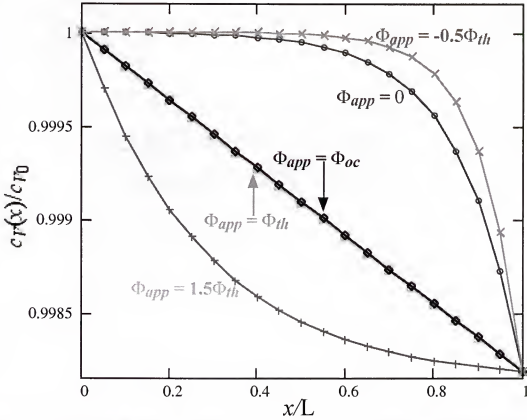
Figure 3-6. Oxygen vacancy concentration profiles in a *p*-type MIEC (ESB) with *fixed* BDCs.

may expect, the defect concentration profiles are similar in form to their counterparts in the DEDs of Figures 2-3 and 2-4, this will become even more evident later in Figures 3-8 and 3-9. Thirdly, because the *p*-type MIEC (ESB) is a good electrolyte ($\Phi_{oc}/\Phi_{th} \approx$ 0.975), one observes, in Figures 3-6 and 3.7, that the concentration profiles for $\Phi_{app} =$ Φ_{th} and $\Phi_{app} = \Phi_{oc}$ coincide. This is in contrast to the *n*-type MIEC (SDC), in Figures 3-4 and 3-5, which is a poorer electrolyte because of its higher electronic conductivity ($\Phi_{oc}/\Phi_{th} \approx 0.785$). For the same reason, the oxygen vacancy concentration gradients are much smaller in ESB than SDC.

Figures 3-8 through 3-11 show the normalized defect concentration profiles with *potential dependent* BDCs, for *n*-type and *p*-type MIECs respectively. The profiles are now plotted for various values of $\Delta\Phi$ rather than Φ_{app} since K_r and K_m, c_{i_0} and c_{i_L} are no longer *fixed*—see sections 3.5.2 and Table 3-2. In contrast to Figures 3-4 through 3-7, the
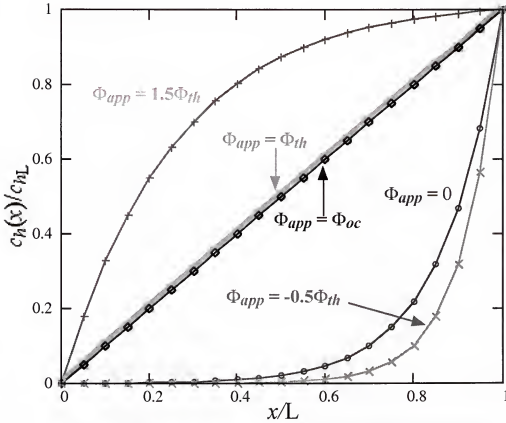
Figure 3-7. Hole concentration profiles in a p-type MIEC (ESB) with *fixed* BDCs.

influence of the operating conditions on the BDCs, as well as the concentration profiles, is evident in Figures 3-8 through 3-11. One observes in the latter plots that the slope of the concentration profile changes in sign as $\Delta\Phi$ passes through the value $-\Phi_{th}$. $\Delta\Phi = -\Phi_{th}$, corresponds to an external power source that has been applied to the MIEC in such a way that it is equal in magnitude, but opposite in sign, to the theoretical (Nernst) potential generated by the MIEC. In other words, the external power source has eliminated the chemical potential gradients of the defect species and, accordingly, a flat defect concentration profile observed. In *reverse bias*, $\Delta\Phi < -\Phi_{th}$, the sign of the concentration gradients is opposite that of the fuel cell mode ($-\Phi_{th} < \Delta\Phi < \Phi_{th}$) or the *forward bias* mode ($\Delta\Phi > \Phi_{th}$). In *reverse bias* the external power source is large enough to overcome the Nernst potential generated by the MIEC and has reversed the concentration gradients originally imposed by P_0 and P_L. These features are not observed with *fixed* BDCs,
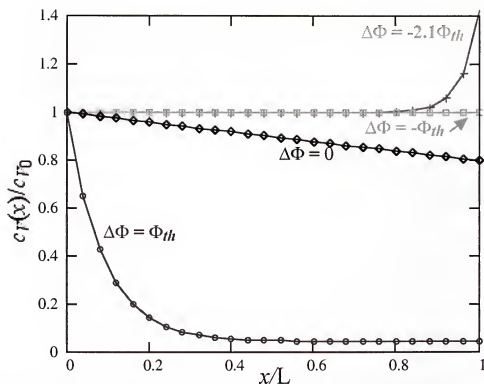
Figure 3-8. Oxygen vacancy concentration profiles in an *n*-type MIEC (SDC) with *potential dependent* BDCs.
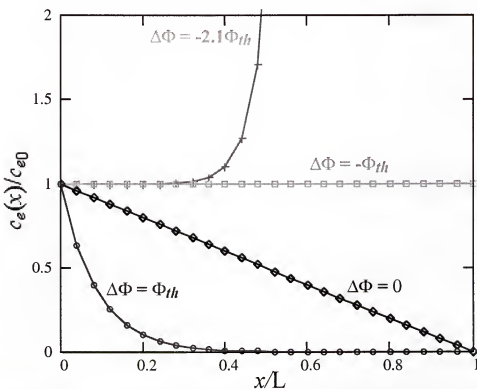

Figure 3-9. Electron concentration profiles in an *n*-type MIEC (SDC) using *potential dependent* BDCs.
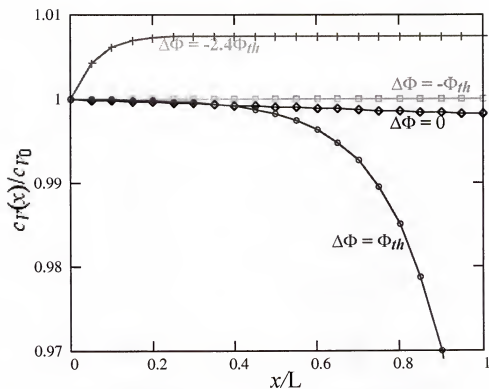
Figure 3-10. Oxygen vacancy concentration profiles in a *p*-type MIEC (ESB) with *potential dependent* BDCs.
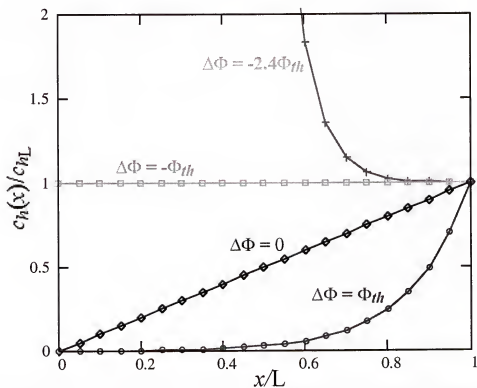

Figure 3-11. Hole concentration profiles in a *p*-type MIEC (ESB) with *potential dependent* BDCs.

which force the concentration gradients to maintain the same sign irrespective of the applied potential.

To emphasize how the applied potential affects the potentials across the MIEC, consider Eqs. (3.3.28) which may be rewritten as follows:

$$\Phi_{app} = \underbrace{\bar{t}_{ion}\Phi_{th}}_{\text{Chemical/Nernstian}} - \underbrace{\Delta\Phi}_{\text{Electrical/Ohmic}} \qquad (3.3.28)$$

This expression shows that Φ_{app} affects (or is affected by) the *chemical* potential difference and the *ohmic* potential difference. When $\Delta\Phi = -\Phi_{th}$ (at which point $\bar{t}_{ion} \approx 1$, see Table 3-2) the *chemical* potential difference is equal to but opposite the *ohmic* potential difference and the defect concentration gradients are eliminated.

Similarly, $\Delta\Phi = 0$ ($\Phi_{app} = \Phi_{oc}$) corresponds to the absence of the electrical component to the potential that is caused by *open-circuit* conditions, $I_{ext} = 0$. Likewise, $\Phi_{app} = 0$ implies that the chemical potential is exactly equal to the electrical potential (i.e., all the available chemical energy is being converted to electrical energy) and therefore the MIEC has been short-circuited.

Figures 3-12 and 3-13 are plots of the defect concentration distribution profiles from a different perspective than shown in Figures 3-8 through 3-11. Figures 3-8 through 3-11 depict the effect of $\Delta\Phi$ on the concentration profiles for a defect type. However, Figures 3-12 and 3-13 contrast the concentration profiles of the mobile defects for a given value of $\Delta\Phi$. As in Figures 3-8 through 3-11, Figures 3-12 and 3-13 show that defect concentration gradients vary in both size and direction as $\Delta\Phi$ changes. One advantage of the representation of the defect concentration profiles in Figures 3-12 and 3-13 is that the change in the character of the MIEC (from mixed ionic-electronic to pure ionic) with position, depending on the value of $\Delta\Phi$, is seen more readily. For $\Delta\Phi = \Phi_{th}$ (*short-circuit*) and $\Delta\Phi = -3\Phi_{th}$ the MIEC is predominantly an electronic conductor near to $x = 0$ and $x = L$ respectively. Conversely, when $\Delta\Phi = -\Phi_{th}$, the MIEC is dominated by ionic
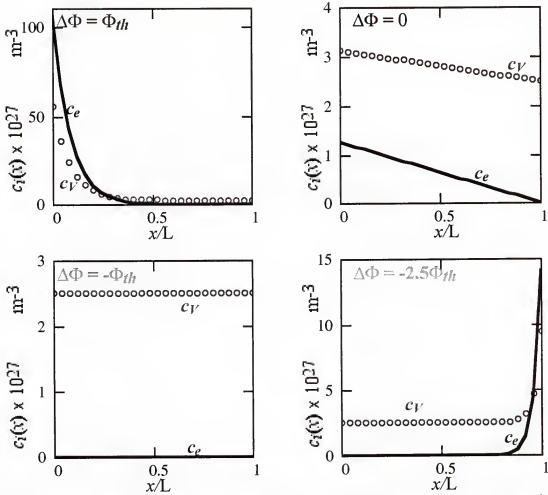
Figure 3-12. Comparison of the spatial distribution of oxygen vacancies and electrons in an *n*-type MIEC (SDC) with *potential dependent* BDCs.

conduction. These features should become even clearer in the next section. Finally, for a given potential it is easier to compare the differences in the defect concentration profiles in Figures 3-12 and 3-13. Hence it is readily observed that the oxygen vacancy concentration profiles are less affected by $\Delta\Phi$ than the profiles of the electronic defects; a consequence of the acceptor doping. In addition, the defect concentration gradients seem to be confined primarily to the near surface areas, rather than being distributed across the entire MIEC.
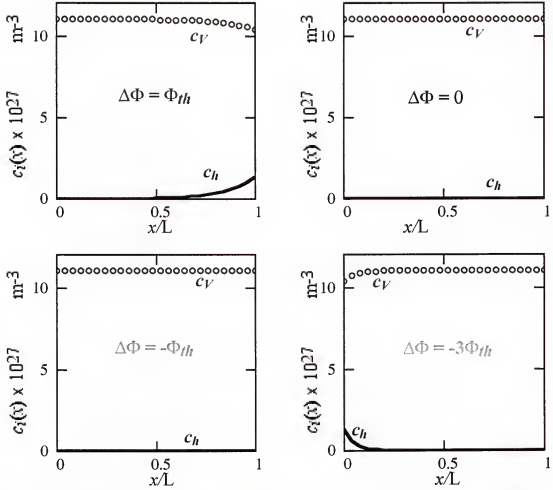
Figure 3-13. Comparison of the spatial distribution of oxygen vacancies and holes in a *p*-type MIEC (ESB) with *potential dependent* BDCs.

3.6.2 Average Defect Conductivity and Effective Ionic Transference Number

Figures 3-14 and 3-15 are plots of $\overline{\sigma}_i$, and $\overline{t}_{ion}$ as functions of $\Delta\Phi$ using *fixed* and *potential dependent* BDCs for *n*-type and *p*-type MIECs respectively from Eqs. (3.4.6) and (3.4.7). The treatment in this section assumes that the materials remain *n*-type or *p*-type irrespective of $\Delta\Phi$. That assumption is not necessarily true, but it is justifiable on two counts. Firstly, most MIECs become unstable in the region of an $n \leftrightarrow p$ transition and secondly the intent here is to show the trends and the legitimacy of using *potential dependent* rather than *fixed* BDCs. Figures 3-14a and 3-15a show that as $\Delta\Phi \to \pm\infty$ $\overline{\sigma}_i$ approaches a constant value with *fixed* BDCs and an approximately constant slope with

Figure 3-14. (a) Average conductivity and (b) effective transference number of an *n*-type MIEC (SDC) with *potential dependent* (—) versus *fixed* (—) BDCs.

potential dependent BDCs. For *n*-type MIECs, Eq. (3.4.6) shows that

$$\lim_{\Delta\Phi\to\infty}\overline{\sigma}_i = z_i^2 D_i q f c_{i_L}$$

and

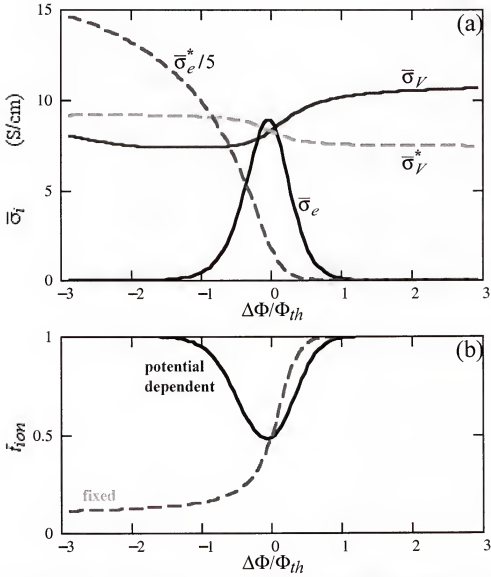$$\lim_{\Delta\Phi\to-\infty}\overline{\sigma}_i = z_i^2 D_i q f c_{i_0}$$
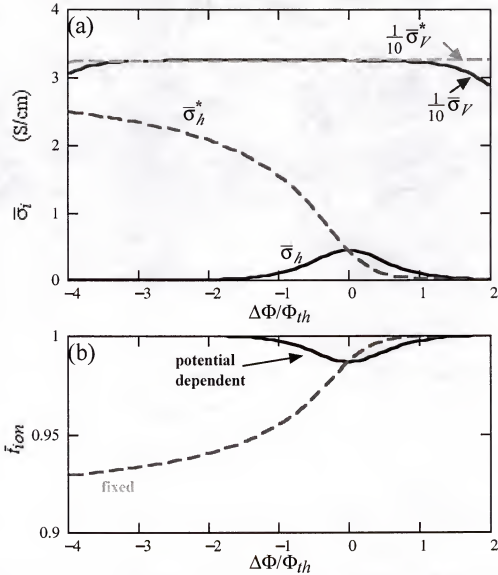
Figure 3-15. (a) Average conductivity and (b) effective transference number of a *p*-type MIEC (ESB) with *potential dependent* (—) versus *fixed* (—) BDCs.

Similarly, for *p*-type MIECs Eq. (3.4.6) shows that

$$\lim_{\Delta\Phi\to\infty}\overline{\sigma}_I = z_i^2 D_i q f c_{i_0}$$

and

$$\lim_{\Delta\Phi\to-\infty}\overline{\sigma}_I = z_i^2 D_i q f c_{i_L}$$

for *p*-type MIECs. Hence, with *fixed* BDCs, $\bar{\sigma}_i$ approaches a constant value. Alternatively, since $\bar{\sigma}_i$ is roughly proportional to the area under the concentration profiles, then that area approaches a constant as $\Delta\Phi \to \pm\infty$ (see Figures 3-4 through 3-7) when the BDCs are *fixed*. Conversely, when *potential dependent* BDCs are used, one must consider Eqs. (3.5.13) through (3.5.16) which show that as $\Delta\Phi \to \infty$

$$c_{V_0} \to \infty, \quad c_{e_0} \to \infty, \quad c_{V_L} \to \tfrac{1}{2}c_A \quad \text{and} \quad c_{e_L} \to 0$$

for *n*-type MIECs and

$$c_{V_0} \to \tfrac{1}{2}c_A, \quad c_{h_0} \to 0, \quad c_{V_L} \to \infty \quad \text{and} \quad c_{h_L} \to c_A$$

for *p*-type MIECs. Similarly, as $\Delta\Phi \to -\infty$

$$c_{V_0} \to \tfrac{1}{2}c_A, \quad c_{e_0} \to 0, \quad c_{V_L} \to \infty \quad \text{and} \quad c_{e_L} \to \infty$$

for *n*-type and

$$c_{V_0} \to \infty, \quad c_{h_0} \to c_A, \quad c_{V_L} \to \tfrac{1}{2}c_A \quad \text{and} \quad c_{h_L} \to 0$$

for *p*-type MIECs. Hence the use of *potential dependent* BDCs predicts that as $\Delta\Phi \to \pm\infty$ $\bar{\sigma}_e$ and $\bar{\sigma}_h$ decrease while $\bar{\sigma}_V$ increases. With *potential dependent* BDCs, the areas under the concentration profiles are allowed to grow or shrink as the attachment points to the vertical axis, c_{i_0} and c_{i_L}, vary with $\Delta\Phi$.

The physical significance of these results may be appreciated by considering what happens when an external circuit is placed across an SOFC/electrocatalytic reactor (initially in *open-circuit* conditions). The introduction of the external circuit provides an alternative path for the electrons to travel through. As the resistance of this external

circuit decreases ($\Delta\Phi \to \Phi_{th}$) more electrons flow through the external circuit than the MIEC. Effectively, this corresponds to a decrease in the $\overline{\sigma}_{e,h}$ which depends on $c_{e,h}$, which is in turn controlled by the operating conditions (i.e., $\Delta\Phi$). In other words, the external load draws electrons or holes from the MIEC by way of the interfacial reactions in Eq. (3.5.1) or (3.5.4) on one side of the MIEC. The electrons or holes are "returned" on the other side of the MIEC, but the effect on the concentration profile leads to a decrease in $\overline{\sigma}_{e,h}$. This effect is probably best observed in Figures 3-12 and 3-13. This behaviour, as shown in Figures 3-14a and 3-15a, is predicted with both *fixed* and *potential dependent* BDCs. The discrepancy between the two approaches shows up in *reverse* and *forward biased* conditions where an external power supply is powering the MIEC. When a power supply[21] is placed across the MIEC it still represents an easier path for the electrons to flow through than the MIEC. However, the external source now driving the interfacial reactions pushes c_{i_0} and c_{i_L} beyond the values attained under fuel cell operation ($0 < \Delta\Phi < \Phi_{th}$). Hence, as $|\Delta\Phi|$ increases, $\overline{\sigma}_{e,h}$ decreases even more. This behaviour is not observed when using *fixed* BDCs, which predict that $\overline{\sigma}_{e,h}$ increases as $\Delta\Phi \to -\infty$.

Similar arguments may be extended for $\overline{\sigma}_V(\Delta\Phi)$ whose behaviour is primarily due to the shape of the oxygen vacancy profile, which remains flat throughout much of the MIEC whereas the profiles of the electronic defects get steeper as $|\Delta\Phi|$ increases. The presence of the acceptor dopant provides a lower limit for the vacancy concentration ($\mathbf{inf}\{c_{V_L}\} = c_A/2$) and shows up as a broadening of the local minimum at $\Delta\Phi = 0$. Finally, a trough is observed for the *n*-type and a shallow, mesa like peak for the *p*-type MIEC. This contrast is due to the external defect equilibrium associated with each MIEC (see Figures 2-3 and 2-4). As $\Delta\Phi \to \infty$, c_{V_L} remains constant (pinned by the acceptor dopant) for the *n*-type MIEC while c_{V_0} increases, thereby expanding the area under the oxygen vacancy concentration profile and hence $\overline{\sigma}_V$. Because of its contrasting defect equilibria,

---

[21] The assumption here is that the power supply has a relatively small internal resistance which is also not a strong function of I_{ext}. This is typical of power supplies applied to electrocatalytic reactors.

the converse is true for the p-type MIEC for which c_{V_0} remains constant (pinned by the acceptor dopant) while c_{V_L} decreases, thereby reducing the area under the oxygen vacancy concentration profile and hence $\bar{\sigma}_{V'}$. As $\Delta\Phi \to -\infty$, the trend is repeated except that c_{V_L} and c_{V_0} swap roles.

Figures 3-14b and 3-15b exhibit the dependence of $\bar{t}_{ion}$ with $\Delta\Phi$. In line with the arguments developed above, they show that $\bar{t}_{ion}$ approaches a minimum as $\Delta\Phi \to 0$ when *potential dependent* BDCs are used. $\Delta\Phi \to 0$ corresponds to an increasingly resistive external circuit, forcing more electrons to travel through the MIEC. Accordingly, as the external circuit becomes less resistive (i.e., as $\Delta\Phi$ moves away from zero) fewer electrons flow through the MIEC and $\bar{t}_{ion}$ increases towards unity since the fraction of current carried by the electrons is decreasing. Conversely, when *fixed* BDCs are used no minimum is observed and $\bar{t}_{ion}$ decreases monotonically in *reverse* bias. This implies that the electronic defects become the dominant means of charge conduction when the MIEC is reverse biased. That is unlikely however, because the external circuit is still more electrically conductive than the MIEC. Moreover, if it was true then MIEC electrocatalytic reactors (oxygen pumps) which, by definition (see section 1.2), operate in reverse bias would be useless or at least extremely inefficient. Electrocatalytic reactors rely on the MIEC having a high $\bar{t}_{ion}$ in reverse bias so that the external power supply can be used to drive oxygen through it. If $\bar{t}_{ion}$ is low, then the power supply drives electrons through the MIEC instead.

3.6.3 Defect Flux Density and Current Density

Figures 3-16 and 3-17 depict the functional dependence of j_i on $\Delta\Phi$ given in Eqs. (3.4.5) for *n*-type and *p*-type MIECs respectively and compare, again, the effects of using *fixed* versus *potential dependent* BDCs. Included in the plots is j_{ambi} from Eq. (3.4.14) which gives perspective on the *closed-circuit* defect flux as compared to *open-circuit* defect flux. The plots are separated into $\Delta\Phi > 0$ (Figures 3-16a, 3-16b, 3-17a and 3-17b)
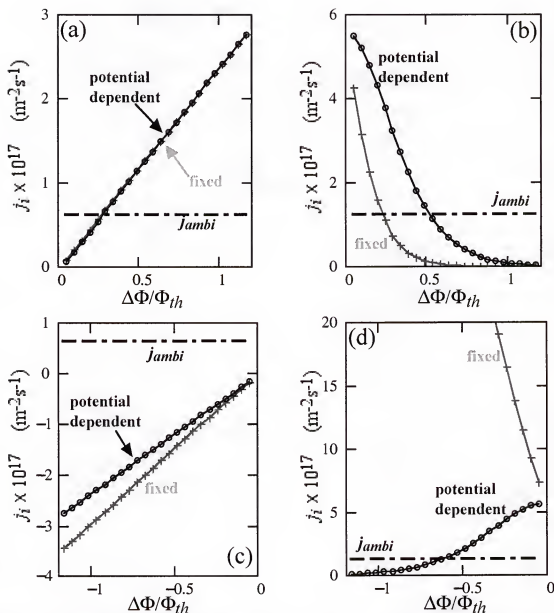
Figure 3-16. Defect flux density in an *n*-type MIEC (SDC). Comparing the effect of using *potential dependent* versus *fixed* BDCs on (a) j_V when $\Delta\Phi > 0$, (b) j_e when $\Delta\Phi > 0$, (c) j_V when $\Delta\Phi < 0$ and (d) j_e when $\Delta\Phi < 0$.
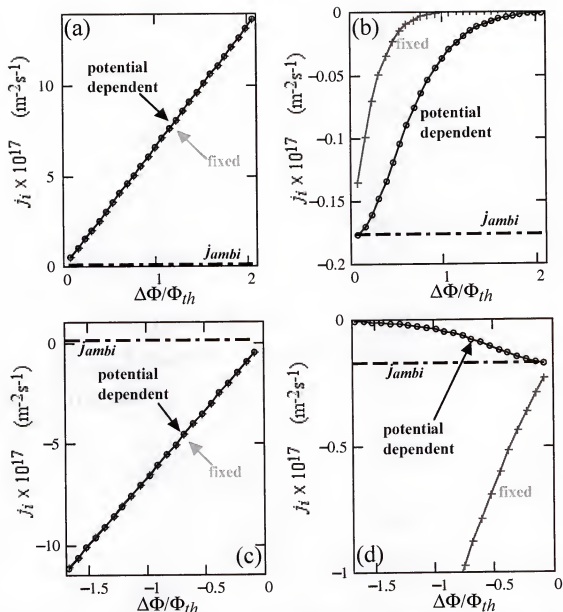
Figure 3-17. Defect flux density in a *p*-type MIEC (ESB). Comparing the effect of using *potential dependent* versus *fixed* BDCs in ESB on (a) j_V when $\Delta\Phi > 0$, (b) j_h when $\Delta\Phi > 0$, (c) j_V when $\Delta\Phi < 0$ and (d) j_h when $\Delta\Phi < 0$.

and $\Delta\Phi < 0$ (Figures 3-16c, 3-16d, 3-17c and 3-17d) to exclude *open-circuit* flux density (when $\Delta\Phi = 0$), which is mechanistically different from *closed-circuit* flux density (when $\Delta\Phi \neq 0$), a point developed earlier in section 3.4.2.

Figures 3-16a, 3-16c, 3-17a and 3-17c show a linear dependence of the oxygen vacancy flux on $\Delta\Phi$ when using *fixed* or *potential dependent* BDCs for both *n*-type and *p*-type MIECs. These results are readily understood by considering that

$$\lim_{\Delta\Phi \to \infty} j_V = z_V D_V \frac{f}{L} \Delta\Phi c_{V_L}$$

and

$$\lim_{\Delta\Phi \to -\infty} j_V = z_V D_V \frac{f}{L} \Delta\Phi c_{V_0}$$

for *n*-type MIECs, and

$$\lim_{\Delta\Phi \to \infty} j_V = z_V D_V \frac{f}{L} \Delta\Phi c_{V_0}$$

and

$$\lim_{\Delta\Phi \to -\infty} j_V = z_V D_V \frac{f}{L} \Delta\Phi c_{V_L}$$

for *p*-type MIECs. Hence, with *fixed* BDCs $j_V \propto \Delta\Phi$, which leads to the aforementioned linear dependence. The linear dependence is maintained when *potential dependent* BDCs are applied because $c_{V_L} \to c_A/2$ as $\Delta\Phi \to \infty$ and $c_{V_0} \to c_A/2$ as $\Delta\Phi \to -\infty$, for *n*-type MIECs; and $c_{V_0} \to c_A/2$ as $\Delta\Phi \to \infty$ and $c_{V_L} \to c_A/2$ as $\Delta\Phi \to -\infty$, for *p*-type MIECs.

Figures 3-16b, 3-16d, 3-17b and 3-17d show that with *potential dependent* BDCs, the fluxes of electrons and holes each approach a maximum at $\Delta\Phi = 0$, i.e., at *open-circuit*, and

go to a minimum as $\Delta\Phi$ moves away form zero, i.e., as the external circuit grows less resistive. With *fixed* BDCs, the electron and hole fluxes show a similar dependence for $\Delta\Phi > 0$ but differ greatly in *reverse bias* where using *fixed* BDCs predicts $j_e \propto \Delta\Phi$. As discussed in the previous section, if the electronic defects become the dominant means of charge conduction when the MIEC is reverse biased then MIEC electrocatalytic reactors would become inefficient because the power supply drives a large electron flux through the MIEC at the expense of an oxygen vacancy (and therefore, oxygen) flux.

The ambipolar flux is also plotted on the figures and it illustrates, as expected, that the electronic flux is reduced and the vacancy flux is enhanced by ambipolar diffusion. In addition, it shows that oxygen vacancies and electrons diffuse in the same direction while vacancies and holes diffuse in opposite directions. Physically, it is hard to visualize how the diffusion potential is maintained in the latter result and it might better be pictured as vacancies and valence band electrons traveling together in the same direction.

Figures 3-18 and 3-19 are plots of the total current density, J versus $\Delta\Phi$. An expression for J is obtained by combining Eqs. (3.3.16) and (3.4.5) with the result:

$$J = \frac{qf\dfrac{\Delta\Phi}{L}\left\{ z_V^2 D_V\left[c_{V_L} - c_{V_0}\exp\left(z_{e,h}/\Delta\Phi\right)\right] + z_{e,h}^2 D_{e,h}\left[c_{e,h_L} - c_{e,h_0}\exp\left(z_{e,h}/\Delta\Phi\right)\right]\right\}}{1 - \exp\left(z_{e,h}/\Delta\Phi\right)} \quad (3.6.1)$$

For *potential dependent* BDCs, Figures 3-18a and 3-18c show the current density in the *n*-type MIEC, SDC, varies from being predominantly electronic (i.e., a leakage current), for $|\Delta\Phi|$ near zero, to predominantly ionic (i.e., no leakage current), as $|\Delta\Phi|$ moves away from zero. In contrast, for the *p*-type MIEC, which here is represented by a better electrolyte in ESB, Figures 3-19a and 3-19c show the current density is predominantly ionic (i.e., no leakage current) for all values of $\Delta\Phi$. However, consistent with the results for defect flux, J is shown to be predominantly electronic in *reverse* bias when *fixed* BDCs are used. Besides the points argued earlier (for conductivity, transference number

Figure 3-18. Defect current density in an *n*-type MIEC (SDC). Comparing the effect of using *potential dependent* versus *fixed* BDCs on (a) I_V when $\Delta\Phi > 0$, (b) I_e when $\Delta\Phi > 0$, (c) I_V when $\Delta\Phi < 0$ and (d) I_e when $\Delta\Phi < 0$.
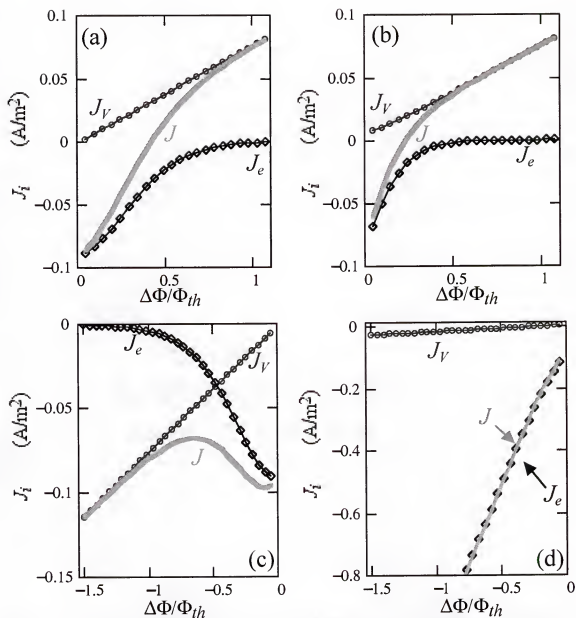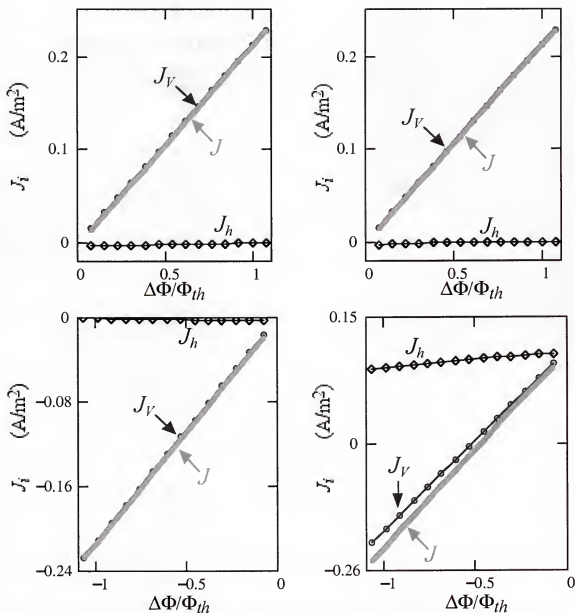
Figure 3-19. Defect current density in a *p*-type MIEC (ESB). Comparing the effect of using *potential dependent* versus *fixed* BDCs on (a) J_V when $\Delta\Phi > 0$, (b) J_h when $\Delta\Phi > 0$, (c) J_V when $\Delta\Phi < 0$ and (d) J_h when $\Delta\Phi < 0$.

and flux) its incorrectness, this result also suggests that the MIEC is somehow a good electronic conductor in reverse bias but a poor one in forward bias (somewhat like a diode).

3.6.4 Efficiency

The current efficiency, ζ_J, for an SOFC or electrocatalytic reactor, is the ratio of the total current to the ionic current ($J \leq J_V$ since J_e/J_h goes in an opposite direction to J_V) and is defined as (combining Eqs. (3.3.16) (3.4.5) and (3.6.1))

$$\zeta_J = \frac{J}{J_V} = \frac{J_V + J_e}{J_V} = 1 + \frac{z_{e,h}^2 D_{e,h}}{z_V^2 D_V} \cdot \frac{c_{e,h_L} - c_{e,h_0} \exp\left(z_{e,h}/\Delta\Phi\right)}{c_{V_L} - c_{V_0} \exp\left(z_V/\Delta\Phi\right)} \quad (3.6.2)$$

Similarly, the power efficiency, ζ_P, is defined as

$$\zeta_P = \frac{J}{J_V} \cdot \frac{\Phi_{app}}{\Phi_{th}} = \frac{\Phi_{app}}{\Phi_{th}}\left[1 + \frac{z_{e,h}^2 D_{e,h}}{z_V^2 D_V} \cdot \frac{c_{e,h_L} - c_{e,h_0} \exp\left(z_{e,h}/\Delta\Phi\right)}{c_{V_L} - c_{V_0} \exp\left(z_V/\Delta\Phi\right)}\right] \quad (3.6.3)$$

Figures 3-20 and 3-21 are plots of ζ_J and ζ_P as functions of $\Delta\Phi$ for MIECs under fuel cell conditions. The figures show that higher current and power efficiencies are obtained for the p-type MIEC. This is an expected result because the p-type MIEC has a higher $\bar{t}_{ion}$ and σ_{ion}. The efficiencies fall rapidly as $\Delta\Phi \to 0$ because of the onset of ambipolar diffusion. These results are typical and were produced by other Liu's model [63]. More interestingly (in this context), the use of *fixed* BDCs results in an overestimation of the efficiencies for both MIECs. As expected from earlier discussions, the error is appreciably smaller for the p-type MIEC because of its high $\bar{t}_{ion}$. The error is significant for the n-type MIEC, however, and should not be ignored.

Currently, extensive research is being conducted on acceptor-doped ceria because of its potential as an intermediate temperature (500 °C to 700 °C) fuel cell electrolyte [1, 2,
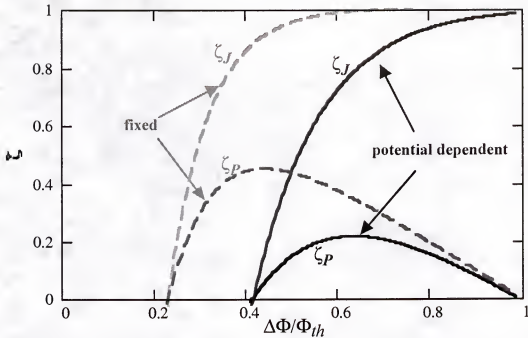
Figure 3-20. Current and power efficiency in an *n*-type MIEC (SDC). Comparing the results of using *potential dependent* (—) versus *fixed* (—) BDCs.
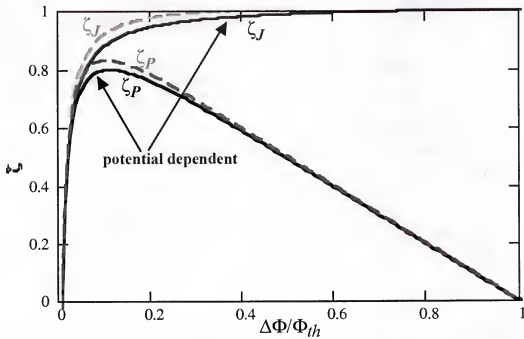

Figure 3-21. Current and power efficiency in a *p*-type MIEC (ESB). Comparing the results of using *potential dependent* (—) versus *fixed* (—) BDCs.

7, 8]. Much of this research is focused on finding better electrode materials for ceria-based electrolytes. This focus is a result of theoretical predictions for ceria-based electrolytes that suggest higher current and power efficiencies are possible than is being obtained experimentally [41, 44, 45, 59, 63]. The shortfall was attributed to problems with the electrodes. It is true that better electrodes are warranted. However, the targeted SOFC efficiencies may have been set too high because of inaccuracies in the theoretical models used to predict them.

3.7. Modeling Defect Distribution and Transport in MIECs without Assuming $\nabla^2\phi = 0$: The Non-Linear Potential Model

In the previous sections the impact of *potential dependent* versus *fixed* BDCs on the spatial distribution and transport properties of defects in *n*-type and *p*-type oxide MIECs was emphasized. In order not to compare "apples with oranges" the concentration profiles were modeled assuming a Laplacian potential, $\nabla^2 \cdot \phi = 0$, as other researchers have done. Thus the effect of introducing *potential dependent* BDCs could be evaluated without ambiguity. Having established the need for *potential dependent* BDCs in sections 3.5 and 3.6; this section now focuses on the effect of relaxing the assumption that $\nabla^2 \cdot \phi = 0$ (i.e., ϕ is not forced to vary linearly with position).

3.7.1 General Development of the Model

To obtain an expression for $c_V(x)$ Eqs. (3.3.14), (3.3.16), (3.3.17), (3.3.24) and (3.3.25) are combined to eliminate $c_{e,h}$ with the result:

$$-J = z_V q \Big(D_V - D_{e,h}\Big)\nabla c_V + z_V q f\Big(z_V D_V - z_{e,h} D_{e,h}\Big)c_V \nabla\phi + z_{e,h} D_{e,h} c_A q f \nabla\phi \qquad (3.7.1)$$

Differentiating Eq. (3.7.1) and combining it with Eq. (3.3.18) yields

$$z_V\Big(D_V - D_{e,h}\Big)\nabla^2 c_V + z_V f\Big(z_V D_V - z_{e,h} D_{e,h}\Big)\nabla(c_V\nabla\phi) + z_{e,h} D_{e,h} c_A f \nabla^2\phi = 0 \qquad (3.7.2a)$$

which in turn may be rearranged to give

$$-z_V f\left(z_V D_V - z_{e,h} D_{e,h}\right)\nabla\left(c_V \nabla\phi\right) = z_{e,h} D_{e,h} c_A f \nabla^2\phi + z_V\left(D_V - D_{e,h}\right)\nabla^2 c_V \quad (3.7.2b)$$

Combining Eqs. (3.7.2), (3.3.14) and (3.3.18) yields

$$\nabla^2\phi = \lambda\nabla^2 c_V \qquad (3.7.3)$$

where

$$\lambda = \frac{z_V - z_{e,h}}{z_{e,h} c_A f} \qquad (3.7.4)$$

Eq. (3.7.3) provides an explicit relationship between the potential and the oxygen vacancy concentration. One feature of this relationship, is that (for a given temperature) it shows that the gradient of the electric field approaches zero in two cases. Firstly, $\nabla^2\phi \approx 0$ for very large (acceptor) dopant concentrations ($\lambda \approx 0$), i.e., when the electronic defect concentrations are small. Secondly, $\nabla^2\phi \approx 0$ if the concentration gradient is equal to a constant ($\nabla^2 c_V \approx 0$), i.e., c_V varies linearly with x. There are two definitive cases where defect concentration varies linearly with x. The first is for binary electrolytes (e.g., MIECs where $c_A = 0$), in the absence of convection and homogenous chemical reaction in the bulk [10]. The second is in *open-circuit* conditions, as was shown earlier in section 3.4.2 (see Eq. (3.4.10)).

Given the usual boundary conditions,

$$\text{at } x = 0, \, c_i = c_{i_0} \qquad \text{and} \qquad \text{at } x = L, \, c_i = c_{i_L}$$

the second-order differential equation in Eq. (3.7.3) has solution

$$c_{V_0} - c_V(x) + \frac{\phi(x) - \phi_0}{\lambda} = \gamma x \tag{3.7.5}$$

where

$$\gamma = \frac{\phi_L - \phi_0 + \lambda\left(c_{V_0} - c_{V_L}\right)}{\lambda L} \tag{3.7.6}$$

While giving some information about the behaviour of the concentration and potential gradients, Eqs. (3.7.3) and (3.7.5) is still insufficient as it does not independently relate c_V and x nor ϕ and x. To derive such relationships, additional information about the system is required. Therefore, to determine the spatial distribution, Eq. (3.3.13) is written below for oxygen vacancies and electronic defects, respectively, as follows:

$$-\frac{j_V}{D_V} = \nabla c_V + z_V c_V f \nabla \phi \tag{3.7.7}$$

and

$$-\frac{j_{e,h}}{D_{e,h}} = \nabla c_{e,h} + z_{e,h} c_{e,h} f \nabla \phi \tag{3.7.8a}$$

Rewriting Eq. (3.7.8) as follows

$$f \nabla \phi = -\left(\frac{j_{e,h}}{D_{e,h}} + \nabla c_{e,h}\right) \frac{1}{z_{e,h} c_{e,h}} \tag{3.7.8b}$$

and substituting it along with Eqs. (3.3.24) and (3.3.25) into Eq. (3.7.7) yields

$$-\frac{j_V}{D_V} = \nabla c_V + \frac{z_V c_V}{z_V c_V - c_A} \frac{j_{e,h}}{D_{e,h}} - \frac{1}{z_{e,h}} \frac{z_V^2 c_V}{z_V c_V - c_A} \nabla c_V \tag{3.7.9}$$

Given that at $x = 0$, $c_V = c_{V_0}$, the solution to the first-order differential equation in Eq. (3.7.9) is

$$c_{V_0} - c_V(x) - \frac{\left(z_V a_1 + z_{e,h} a_2\right) c_A}{z_V \left(z_V - z_{e,h}\right)(a_1 + a_2)} \ln \frac{z_V (a_1 + a_2) c_V(x) - \alpha c_A}{z_V (a_1 + a_2) c_{V_0} - \alpha c_A} = \frac{z_{e,h}(a_1 + a_2)}{z_V - z_{e,h}} x \quad (3.7.9)$$

where

$$a_1 = -\frac{j_V}{D_V}$$

and

$$a_2 = -\frac{j_{e,h}}{D_{e,h}}$$

The form of the equation in (3.7.9) is similar to Eq. (3.7.5). Therefore by comparing the two, one obtains

$$a_1 + a_2 = \frac{z_V - z_{e,h}}{z_{e,h}} \gamma = \frac{z_V - z_{e,h}}{z_{e,h}} \cdot \frac{\phi_L - \phi_0 + \lambda\left(c_{V_0} - c_{V_L}\right)}{\lambda L} \quad (3.7.10)$$

and

$$\phi(x) = \phi_0 - \frac{z_V a_1 + z_{e,h} a_2}{z_V \left(z_V - z_{e,h}\right) f \gamma} \ln \frac{c_V - \dfrac{a_1}{z_V f \lambda \gamma}}{c_{V_0} - \dfrac{a_1}{z_V f \lambda \gamma}} \quad (3.7.11)$$

Finally, given that at $x = L$, $c_V = c_{V_L}$ and $\phi = \phi_L$, a_2 may be eliminated from Eqs. (3.7.9) through (3.7.11), yielding

$$\gamma x = c_{V_0} - c_V(x) + \frac{\phi_L - \phi_0}{\ln\left(c_{V_L} - \frac{a_1}{z_V f \lambda \gamma}\right) - \ln\left(c_{V_0} - \frac{a_1}{z_V f \lambda \gamma}\right)} \frac{1}{\lambda} \ln \frac{c_V(x) - \frac{a_1}{z_V f \lambda \gamma}}{c_{V_0} - \frac{a_1}{z_V f \lambda \gamma}} \quad (3.7.12)$$

$$\phi(x) = \phi_0 + \frac{\phi_L - \phi_0}{\ln\left(c_{V_L} - \frac{a_1}{z_V f \lambda \gamma}\right) - \ln\left(c_{V_0} - \frac{a_1}{z_V f \lambda \gamma}\right)} \ln \frac{c_V - \frac{a_1}{z_V f \lambda \gamma}}{c_{V_0} - \frac{a_1}{z_V f \lambda \gamma}} \quad (3.7.13)$$

and

$$(a_1 + \gamma) \ln \frac{c_{V_L} - \frac{a_1}{z_V f \lambda \gamma}}{c_{V_0} - \frac{a_1}{z_V f \lambda \gamma}} = -z_V(\phi_L - \phi_0) f \gamma \quad (3.7.14)$$

Through numerical solution of Eqs. (3.7.12) and (3.7.14), the defect distribution and defect flux and the positional dependence of the potential may now be determined from Eqs. (3.7.12) through (3.7.14), noting that

$$-\Delta \Phi = \phi_L - \phi_0 \quad (3.7.15)$$

3.7.2 Limiting Cases

The form of the relations in Eqs. (3.7.12) and (3.7.13) are similar to those derived by Liu [63]. Unlike Liu's [63] equations however, the constants are readily quantifiable. λ, γ, c_{V_0} and c_{V_L} all relate directly to the operating conditions imposed on the MIEC (i.e., any combination of temperature, dopant concentration, electric and oxygen potential at the boundaries).

To verify the validity of the system of equations their predictions for characteristic operating conditions should be evaluated for consistency. Under *open-circuit* conditions,

$-\Delta\Phi = \phi_L - \phi_0 = 0$, Eq. (3.7.12) reduces to

$$\frac{c_{V_0} - c_{V_L}}{L} x = c_{V_0} - c_V(x) \tag{3.7.16}$$

which is identical to Eq. (3.4.10) derived earlier in section 3.4.2 for *open-circuit* conditions. While Eq. (3.7.14) reduces to

$$a_1 = -\frac{j_{ambi}}{D_{ambi}} = -\frac{c_{V_0} - c_{V_L}}{L} x \tag{3.7.17}$$

(recall that $j_i \equiv j_{ambi}$ under *open-circuit* conditions) which is likewise identical to Eq. (3.4.8) derived in section 3.4.2 for *open-circuit* conditions.

Similarly, for *large* dopant concentrations, where $\lambda \to 0$ and $c_V \approx c_{V_0} \approx c_{V_L} = c_A/2$ (i.e., $\nabla \cdot c_V \approx 0$) Eq. (3.7.5) and (3.7.6) reduce to

$$\phi(x) - \phi_0 = \frac{\phi_L - \phi_0}{L} x \tag{3.7.18}$$

i.e., a linear potential, and

$$\gamma = \frac{\phi_L - \phi_0}{\lambda L} \tag{3.7.19}$$

respectively. Also, for *large* dopant concentrations, the concentration of electronic defects is suppressed and $a_1 \gg a_2$. Therefore, Eq. (3.7.10) reduces to

$$a_1 \approx \frac{z_V - z_{e,h}}{z_{e,h}} \gamma \approx \frac{z_V - z_{e,h}}{z_{e,h}} \cdot \frac{\phi_L - \phi_0}{\lambda L} \tag{3.7.20}$$

which shows that when the potential varies linearly with x the MIEC obeys Ohm's law. Nevertheless, substituting Eq. (3.7.20) into Eqs. (3.7.14) yields

$$a_1 = -\frac{j_V}{D_V} = z_V f \frac{\phi_L - \phi_0}{L} \frac{c_{V_L} - c_{V_0} \exp\left(-z_{e,h}(\phi_L - \phi_0) f\right)}{1 - \exp\left(-z_{e,h}(\phi_L - \phi_0) f\right)} \qquad (3.7.21)$$

Similarly, substituting Eqs. (3.7.19), (3.7.20), (3.3.24) (3.3.25) and (3.3.34) (assuming t_{ion} ≈ 1 since the concentration of electronic defects is suppressed by the large dopant concentration) into Eq. (3.7.12) yields

$$c_V(x) = \left(c_{V_0} - \frac{c_A}{z_V}\right) \exp\left(-z_{e,h} f(\phi_L - \phi_0)\frac{x}{L}\right) + \frac{c_A}{z_V} \qquad (3.7.22)$$

Eqs. (3.7.18), (3.7.21) and (3.7.22) are all either equivalent in form, or identical to the expressions derived for said properties in section 3.4 where the potential was forced to be linear.

Finally, for *small* dopant concentrations (i.e., a binary electrolyte with $t_{ion} \approx 0$), where $c_A \to 0$ and $\lambda \to \infty$, Eq. (3.7.12) through (3.7.14) reduce to

$$\frac{c_{V_0} - c_{V_L}}{L} x = c_{V_0} - c_V(x) \qquad (3.7.23)$$

$$\phi(x) = \phi_0 \qquad (3.7.24)$$

and

$$a_1 = -\frac{j_V}{D_V} = \frac{c_{V_L} - c_{V_0}}{L} \qquad (3.7.25)$$

3.7.3 Average Conductivity and Effective Transference Number

The form of the equation for the spatial distribution of defects in the MIEC, Eq. (3.7.12), is not suitable for substitution into Eq. (3.3.13) to obtain an expression, by

integration, for $\overline{\sigma}_i$ as was done in section 3.4.1. Consequently, a slightly different approach is introduced here to produce the desired relation. After multiplying through by L, Eqs. (3.3.14) and (3.3.15) may be combined and rearranged to yield

$$\frac{1}{L\sigma_i} = -\frac{1}{z_i^2 q^2 j_i} \nabla \tilde{\mu}_i = -\frac{1}{z_i^2 q^2 j_i L} \nabla (kT\ln c_i + z_i q\phi) \tag{3.7.26a}$$

Comparing Eq. (3.7.26a) with Eq. (3.3.13) shows that

$$\overline{\sigma}_i = \left\{ \frac{1}{L}\int_0^L \frac{1}{\sigma_i} \cdot dx \right\}^{-1} = \left\{ -\frac{1}{z_i^2 q^2 j_i L} \left[\int_0^L (kT\nabla \ln c_i + z_i q\nabla \phi) \cdot dx \right] \right\}^{-1}$$

$$= \left\{ -\frac{1}{z_i^2 q^2 j_i L} \left[kT\int_{c_0}^{c_L} \frac{dc_i}{c_i} + z_i q\int_{\phi_0}^{\phi_L} d\phi \right] \right\}^{-1} \tag{3.7.26b}$$

which may now be solved to obtain

$$\overline{\sigma}_i = \frac{z_i^2 q^2 j_i L}{kT\ln \dfrac{c_{i_0}}{c_{i_L}} - z_i q(\phi_L - \phi_0)} \tag{3.7.27}$$

This expression for $\overline{\sigma}_i$ may then be substituted into Eq. (3.3.7) for $\overline{i}_{ion}$ to obtain:

$$\overline{i}_{ion} = \left[1 + \frac{z_{e,h}^2 j_{e,h}}{z_V^2 j_V} \frac{kT\ln \dfrac{c_{V_L}}{c_{V_0}} + z_V q(\phi_L - \phi_0)}{kT\ln \dfrac{c_{e,h_L}}{c_{e,h_0}} + z_{e,h} q(\phi_L - \phi_0)} \right]^{-1} \tag{3.7.28}$$

Under *open-circuit* conditions, both Eq. (3.7.27) and Eq. (3.7.28) reduce to those derived earlier in section 3.4.2.

3.8.   Results and Discussion for the Non-Linear Potential Model

As was done earlier in section 3.6 for the linear potential model—developed in section 3.4—in this section, the results obtained above in section 3.7 for the spatial distribution, conductivity, transference number and flux of defects are plotted. In contrast to section 3.6, however, the plots are restricted to the n-type MIEC, SDC. This restraint is imposed for two reasons, firstly ESB, which was the p-type prototype used in section 3.6, is a good electrolyte (i.e., the vacancy concentration distribution is uniform) and the linear potential model developed in section 3.4 is sufficiently accurate. Secondly, (see section 3.6) the behaviour of the p-type MIEC is almost entirely analogous to that of n-type MIECs, with the primary *defining* difference being only the direction of the electron and hole fluxes. The only other difference between n-type and p-type MIECs is the shape of the average conductivity profile for *large* $\Delta\Phi$, but this is secondary effect since it is a consequence of the defect equilibria of the as defined p-type MIEC rather than a change in the identity of electronic charge carrier. Additionally, only *potential dependent* boundary conditions are considered in this section having demonstrated, exhaustively, their propriety over *fixed* BDCs.

Finally, the order in which the properties of the MIEC are examined below is different from the order used in section 3.6. This change is motivated by the form of the system of equations, Eqs. (3.7.12) through (3.7.14). Their solution requires that Eq. (3.7.14) is solved (numerically) first—to obtain a_1 (i.e., j_V)—followed by Eq. (3.7.12)—to obtain c_V—and then finally Eq. (3.7.13)—to obtain ϕ. Consequently, the discussion follows the same order.

3.8.1   Flux, Current, Conductivity, Transference Number and Efficiency

Figures 3-22 and 3-23 are plots of the functional dependence of j_i and J_i on $\Delta\Phi$ generated from the numerical solution of Eq. (3.7.14) for the MIEC. As before (in Figures 3-16 and 3-18), the plots are divided into two sections namely, $\Delta\Phi > 0$ (in Figures 3-22a
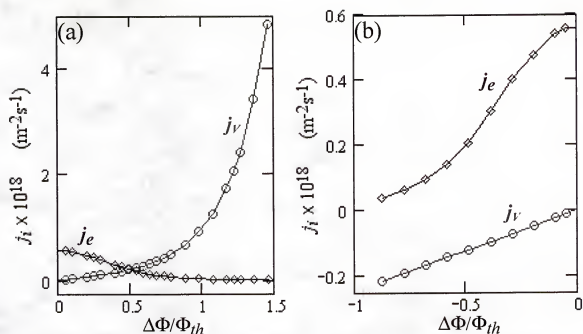
Figure 3-22. Defect flux in an n-type MIEC (SDC)—Non-Linear Potential Model—with *potential dependent* BDCs for (a) $\Delta\Phi > 0$ and (b) $\Delta\Phi < 0$.
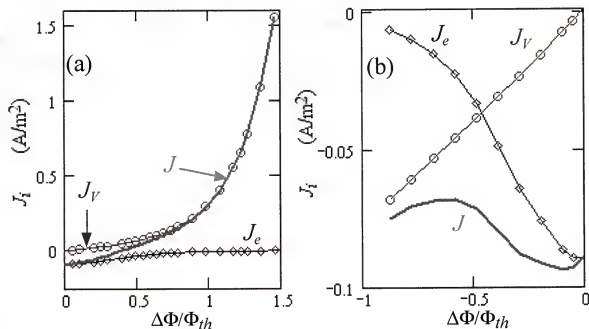

Figure 3-23. Defect current density in an n-type MIEC (SDC)—Non-Linear Potential Model—with *potential dependent* BDCs for (a) $\Delta\Phi > 0$ and (b) $\Delta\Phi < 0$.

and 3-23a) and $\Delta\Phi < 0$ (in Figures 3-22b and 3-23b). The separation is made because ambipolar diffusion occurs when $\Delta\Phi = 0$. The figures show that both j_V and J_V increase non-linearly as $\Delta\Phi$ increases. This is in contrast to the results obtained when a linear potential was assumed, in Figures 3-16 and 3-18. In those plots, j_V and J_V varied linearly (*ohmically*) with $\Delta\Phi$ because the MIEC was forced by that assumption to maintain a flat distribution of oxygen vacancies throughout most of the electrolyte by confining the vacancy concentration gradients to the near surface areas. Now that the MIEC has been unshackled from that constraint, j_V and J_V may now exhibit a non-linear response to $\Delta\Phi$ as the oxygen vacancy distribution changes from a fairly uniform at small $\Delta\Phi$ to highly non-uniform at large $\Delta\Phi$ as shown later in Figures 3-25 and 3-27.

In Figure 3-24 are plots of $\overline{\sigma}_i$, $\overline{t}_{ion}$, ζ_J, and ζ_P as functions of $\Delta\Phi$ for the MIEC. The shape and dimension of all these graphs are quite similar to those in Figures 3-14 and 3-20 except that unlike before, now

$$\lim_{\Delta\Phi \to \infty} \overline{\sigma}_V \neq z_V D_V q f c_A$$

Again this is a result of the defect concentration gradients not being confined to the near surface areas any longer.

The similarity observed between the plots in Figure 3-24 and those in Figures 3-14 and 3-20 may be attributed to the fact that all these properties are either average values ($\overline{\sigma}_i$) or dependent on average values ($\overline{t}_{ion}$, ζ_J, and ζ_P). The averaging process obscures the effect of the defect distribution because $\overline{\sigma}_i \leq \mathbf{inf}(\sigma_{i_k})$. In other words, since the smallest conductivity is always one of the boundary values (since the smallest defect concentration also occurs at a boundary) then that boundary value has a larger impact in determining $\overline{\sigma}_i$ (and therefore the other properties) than the actual conductivity profile.
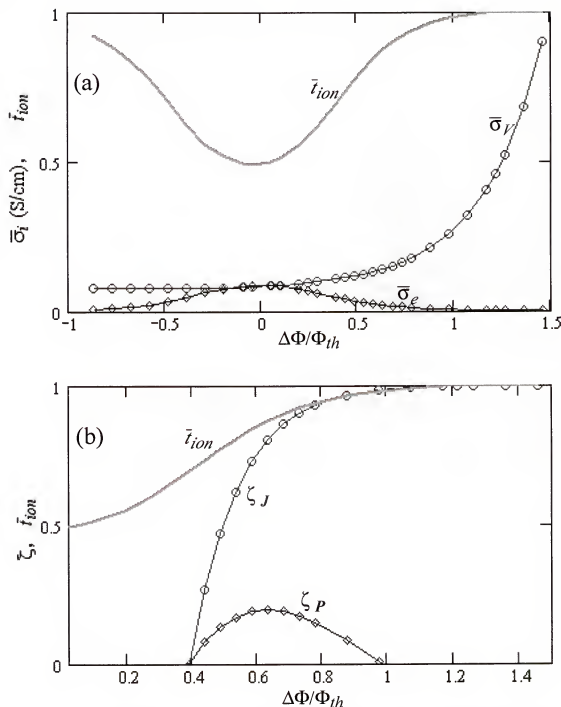
Figure 3-24. (a) Average defect conductivity and (b) effective transference number in an *n*-type MIEC (SDC)—Non-Linear Potential Model—with *potential dependent* BDCs.
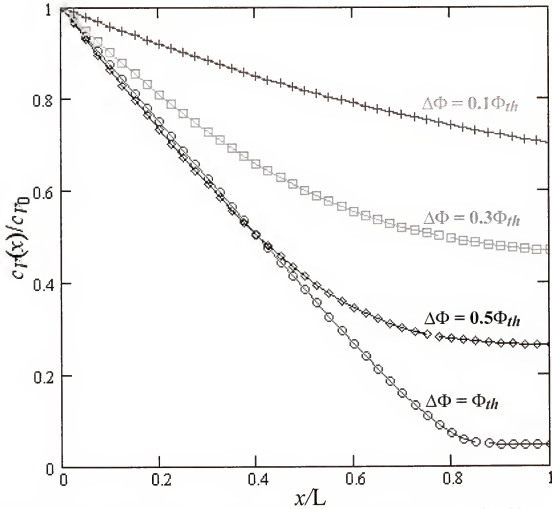
Figure 3-25. Oxygen vacancy concentration profile in an *n*-type MIEC (SDC)—Non-Linear Potential Model—with *potential dependent* BDCs.

3.8.2 Spatial Distribution of Defects and Potential

Figures 3-25, 3-26 and 3-27 show the spatial distribution of the defects in the MIEC. Immediately apparent is that, unlike in section 3.6 (see Figures 3-8, 3-9 and 3-12), the defect concentration gradients are not confined to the near boundary areas. Instead the gradients are spread out across most of the MIEC, especially for *large* $\Delta\Phi$. For example, a comparison of Figures 3-8 and 3-25 shows that in the linear potential model (Figure 3-8) c_V falls rapidly to ~$0.05c_{V_0}$ between $x = 0$ and x = 0.4L. Meanwhile, for the non-linear potential model (Figure 3-25) the same decrease in c_V occurs between $x = 0$ and x = 0.8L, a more gradual decrease. The same is true when the predictions for the spatial distribution
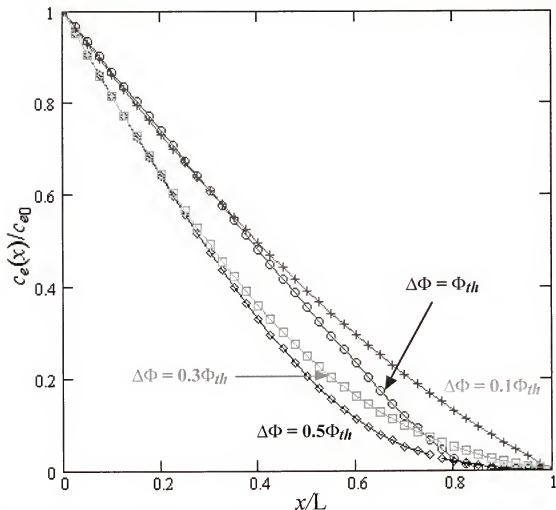
Figure 3-26. Electron concentration profile in an *n*-type MIEC (SDC)—Non-Linear Potential Model—with *potential dependent* BDCs

of c_e, made by the linear potential model and the non-linear potential model, are compared.

As $\Delta\Phi$ approaches zero, the c_V and c_e profiles get more linear in shape as the MIEC approaches *open-circuit* conditions (i.e., as $\Delta\Phi \to 0$). This trend shows that the assumption of a linear electric field, made in the linear potential model (and others like it [41, 59, 62]), gets weaker as one moves away from low current (low $\Delta\Phi$) conditions. In other words, the assumption of a linear electric field is most suitable when $\Delta\Phi$ is small (i.e., close to zero). Negative values of $\Delta\Phi$ are not examined because the highly non-linear
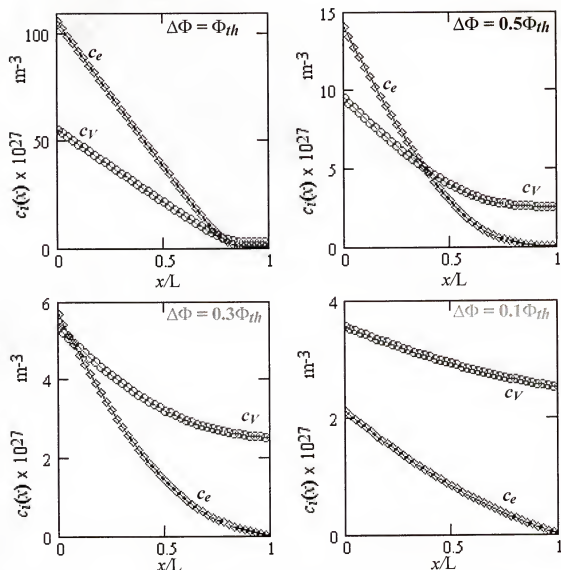
Figure 3-27. Comparison of the spatial distribution of oxygen vacancies and electrons in an *n*-type MIEC (SDC)—Non-Linear Potential Model—with *potential dependent* BDCs.

Eqs. (3.7.12) and (3.7.13) are numerically unsolvable (i.e., real roots of Eqs. (3.7.12) and (3.7.13) could not be found), even through graphical means.

Finally, Figure 3-28 shows how the potential varies with position in the MIEC. The potential is at its most non-linear—with respect to the positional variable, x—when $\Delta\Phi = \Phi_{th}$ (short-circuit conditions) and approaches a linearity as $\Delta\Phi$ goes to zero. This may be explained by considering (see Figure 3-27) that the oxygen vacancy concentration gradient
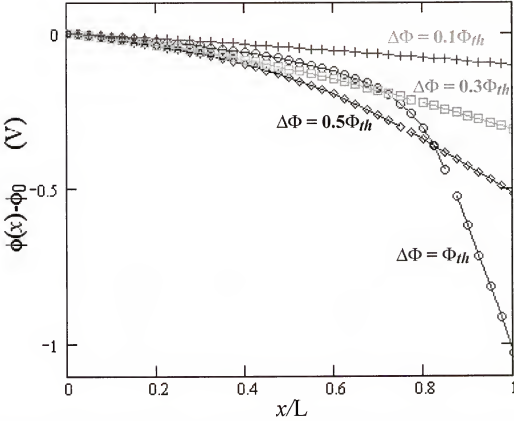
Figure 3-28. Spatial distribution of potential in an *n*-type MIEC (SDC) with *potential dependent* BDCs.

is highest (on average) when $\Delta\Phi = \Phi_{th}$ and gets progressively smaller as $\Delta\Phi$ approaches zero. This concurs with the deductions made in section 3.7.2, Eq. (3.7.18), that the potential becomes approximately linear when $\nabla c_V \approx 0$.

3.9 Experimental Verification of the Model (In *Open-Circuit* Conditions)

In this section, the model developed above is verified experimentally[22], in *open-circuit* conditions, by measuring Φ_{oc} for an SOFC with an SDC membrane and platinum electrodes, see Figure 3-29. Samples of SDC (composition: $Ce_{0.8}Sm_{0.2}O_{1.9}$) were fabricated by the solid state process. CeO_2 (ceria) and Sm_2O_3 (samaria) powders were

---

[22] The experimental work was performed by M. Camaratta and J. Park, members of the authors research group.
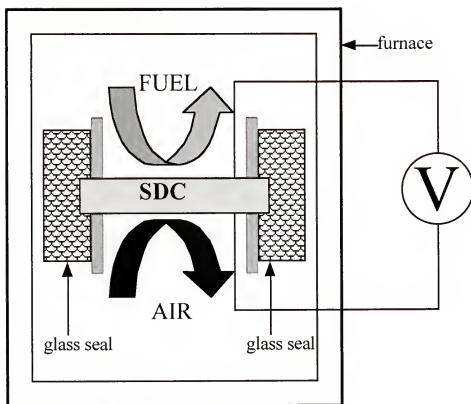
Figure 3-29. Setup of the fuel cell apparatus

weighed out and combined in proportion to produce the desired composition of SDC. These powder mixtures were ball milled for 24 hours, then dried and calcined at 1300 °C -1500 °C. Calcined powders were re-ground, sieved and pressed into pellets that were sintered at 1500 °C -1650 °C. X-ray diffraction was used to verify that the samples had the fluorite structure. Porous platinum electrodes were applied to samples with density $\geq$ 90 % of the theoretical density. These samples were used as membranes in a fuel cell apparatus (Figure 3-29) with air as the oxidizing gas and CO/CO_2 or H_2/H_2O gas mixtures as the reducing gas. The *open-circuit* voltage was then measured (using a Keithley 2000 multimeter) for various values of P_{O_2} set by the mixing ratio of the reducing gas combinations (the P_{O_2} on the oxidizing side was kept constant). The P_{O_2} of each reducing gas combination was measured by a zirconia based (automotive) oxygen sensor with air on its oxidizing side and the reducing gas combination to be measured on its reducing side. The sensor voltage is taken as equal to the theoretical (Nernst) voltage, Φ_{th} for the fuel
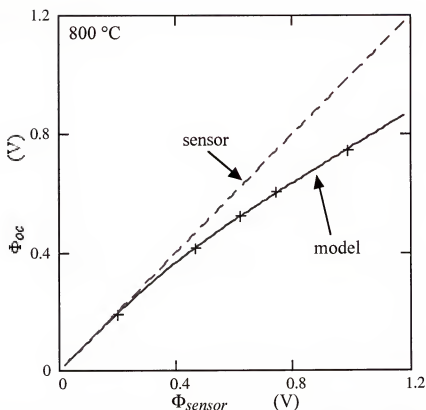
Figure 3-30. *Open-circuit* voltage, Φ_{oc}, versus Φ_{sensor} (Φ_{th}) at 800 °C, model (—) fitted to experimental data (+) for the fuel cell; sensor (- - -).

cell since $\bar{t}_{ion} = 1$ for zirconia. Therefore:

$$\Phi_{sensor} = \Phi_{th} = \frac{kT}{4q} \ln \frac{P_L}{P_0} \qquad (3.9.1)$$

where P_L is the P_{O_2} on the oxidizing/air side (at $x = L$) and P_0 is the P_{O_2} on the reducing/fuel side (at $x = 0$). P_0 may be then be calculated from a knowledge of the sensor voltage, P_L and temperature. Additional details of the experimental procedure may be obtained elsewhere [71]. The results of the experiment are plotted in Figures 3-30 through 3-36.

In to verify the accuracy and validity the model developed for *open-circuit* conditions in section 3.4.3, Eq. (3.4.17) is fitted to the experimental data in Figures 3-30 through 3-36. This was done by adjusting the parameters K_r and Θ (i.e., D_e/D_V) to maximize the
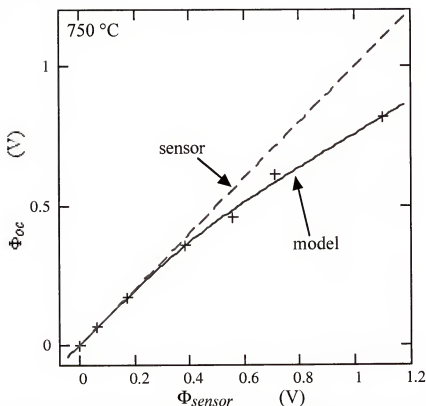
Figure 3-31. *Open-circuit* voltage, Φ_{oc}, versus Φ_{sensor} (Φ_{th}) at 750 °C, model (—) fitted to experimental data (+) for the fuel cell; sensor (---).

correlation coefficient, r, (and $\bar{r}$, the corrected[23] correlation coefficient) [72] between the data and the model (i.e., to obtain the best fit of the model to the data). Table 3-3 shows the parameters used for each plot and the correlation coefficients obtained.

Figures 3-30 through 3-36 show that as P_0 decreases below a critical value, the fuel cell voltage becomes less than the Nernst voltage. This corresponds to an increase in the electronic conductivity of the fuel cell membrane, which is attributable to the increasing concentration of electrons on the reducing side of the fuel cell membrane due to the decreasing P_{O_2} (see Figures 2-3, 2-9, 2-10, 2-11, 3-9 and 3-12b).

The deviation of the fuel cell voltage from the Nernst voltage starts progressively later as the temperature decreases which corresponds to a widening of the electrolytic

---

23 In fitting Eq. (3.4.19) to the experimental data two parameters K_r and Θ, the fitting parameters, are adjusted, hence the model has two *degrees of freedom*. The correlation coefficient, r, is sometimes corrected to reflect the presence of the fitting parameters [72].
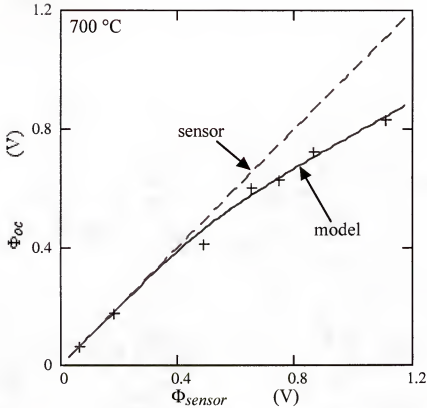
Figure 3-32. *Open-circuit* voltage, Φ_{oc}, versus Φ_{sensor} (Φ_{th}) at 700 °C, model (—) fitted to experimental data (+) for the fuel cell; sensor (- - -).

domain, a phenomenon reported by other researchers. At 800 °C the fuel cell voltage starts to deviate from the Nernst voltage at ~ 0.3 V while at 500 °C the deviation begins at ~ 0.7 V. This behaviour is a consequence of the exponential dependence of K_r on reciprocal temperature (1/T), as defined in Eq. (3.5.11). Thus, K_r increases and SDC produces electrons more readily (i.e., at a higher P_{O_2}) as the operating temperature increases (see Eq. (3.5.3)).

Another noteworthy feature of Figures 3-30 to 3-36, is that as the temperature decreases, the shape of the curve for the fuel cell voltage becomes more plateau-like once the deviation from the Nernst voltage begins. This phenomenon may be explained by considering that at low temperatures $D_e/D_V \gg 1$ and $c_{V_L} \ggg c_{e_L}$, under these conditions Eq. (3.4.17) reduces to:

Figure 3-33. *Open-circuit* voltage, Φ_{oc}, versus Φ_{sensor} (Φ_{th}) at 650 °C, model (—) fitted to experimental data (+) for the fuel cell; sensor (---).

$$\Phi_{oc} \approx -\frac{kT}{z_e q}\left\{\ln\frac{c_{V_L} + \Theta c_{e_L}}{\Theta c_{e_L}}\right\} = \text{constant} \qquad (3.9.2)$$

In other words, at low temperatures Φ_{oc} is independent of P_0, a circumstance predicted by the model and borne out by experiment.

As Figure 3-37 and Table 3-3. show, the values of K_r and D_e/D_V used to get the best fits to the data are respectively, larger and smaller than expected, especially for temperatures ≥ 600 °C. In particular the value of K_r and D_e/D_V obtained at 800 °C do not concur with the values obtained in sections 2.4.2 and sections 3.4.3. This outcome may be explained in two (complementary) ways. The first examines the impact of the (porous platinum) electrodes on the characteristics of the SDC surface as they relate to K_r and D_e/D_V. The second examines the sensitivity of K_r and D_e/D_V to experimental error.
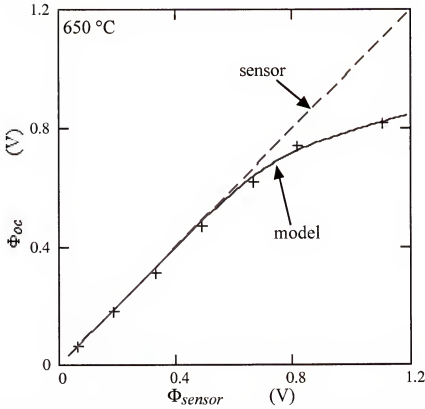
Figure 3-34. *Open-circuit* voltage, Φ_{oc}, versus Φ_{sensor} (Φ_{th}) at 600 °C, model (—) fitted to experimental data (+) for the fuel cell; sensor (---).

Electrode Effects. Figure 3-38a shows surface sites where the oxygen exchange can occur distributed across the surface of the SDC membrane in what may be described as their *normal* states (i.e., before application of the electrodes). When electrodes are introduced, (see Figure 3-38b) the nature of many of the surface sites changes. At the SDC-Pt-gas interface, the so-called triple-phase boundary, the oxygen exchange reaction is enhanced significantly because, for the cathodic reaction (i.e., oxygen incorporation), adsorbed oxygen species (from the gas phase) can obtain electron(s) readily (in comparison to SDC alone) from the metal phase. The adsorbed oxygen species are then transferred into a vacant oxygen site in the MIEC (the ceramic phase). This process is reversed for the anodic reaction (i.e., oxygen release) where oxygen atoms leave oxygen sites in the ceramic phase, release electrons to the metal phase and then reacts with the gas
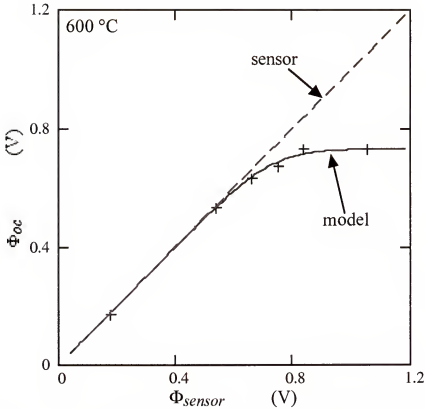
Figure 3-35. *Open-circuit* voltage, Φ_{oc}, versus Φ_{sensor} (Φ_{th}) at 550 °C, model (—) fitted to experimental data (+) for the fuel cell; sensor (---).

phase[24]. The oxygen exchange reaction is further catalyzed by the platinum, which adsorbs oxygen (and, potentially, species from the reducing gas) more readily than SDC [73]. The adsorbed oxygen (cathode reaction) migrates to the triple-phase boundary or even to surface sites in its neighbourhood that benefit from the spreading of electrons across the surface from the triple phase boundaries (i.e., the *enhanced* surface sites depicted in Figure 3-38b).

The platinum electrodes also have, potentially, deleterious effects. One such negative effect arises from the platinum particles *sitting* on top of some surface sites (i.e., the *diminished* surface sites as depicted in Figure 3-38b) and, thereby, effectively denying

---

24 This is a highly simplified description. The steps for the anodic reaction is very complex and involves several steps which have not yet been identified without ambiguity. A primary source of uncertainty for the anodic reaction is the presence (theoretically) of numerous paths by which the reaction between the fuel and the oxygen species can occur [73].
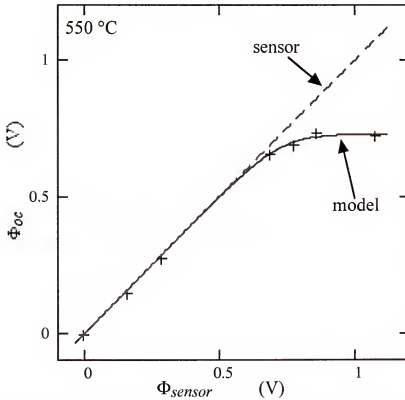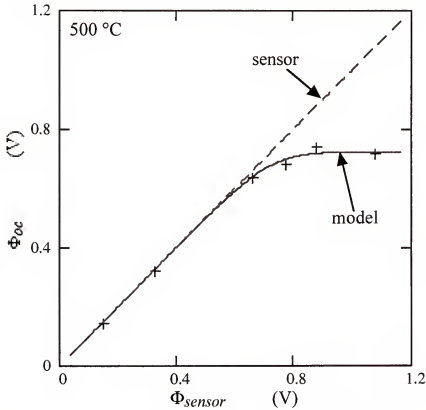
Figure 3-36. *Open-circuit* voltage, Φ_{oc}, versus Φ_{sensor} (Φ_{th}) at 500 °C, model (—) fitted to experimental data (+) for the fuel cell; sensor (---).

Table 3-3. Values of K_r and D_e/D_V used to fit the model to experimental data

Temperature (°C)	K_r (m^{-9}atm.$^{1/2}$)	$\ln K_r$	D_e/D_V	r	$\tilde{r}$
800	1.0×10^{72}†	165.8	1.1×10^2	0.958	0.929
800	1.4×10^{79}	182.3	1.4	1.00	1.00
750	1.6×10^{78}	180.1	1.6	0.999	0.999
700	4.0×10^{77}	178.7	1.5	0.996	0.995
650	5.6×10^{73}	169.8	5.6	0.999	0.998
600	1.0×10^{71}	163.5	71	0.999	0.998
550	4.5×10^{66}	153.5	5.7×10^3	0.999	0.999
500	4.0×10^{65}	151.1	1.0×10^4	0.999	0.998

† K_r calculated from thermogravimetric data of Kobayashi *et al.* [47] in section 2.4.2.3
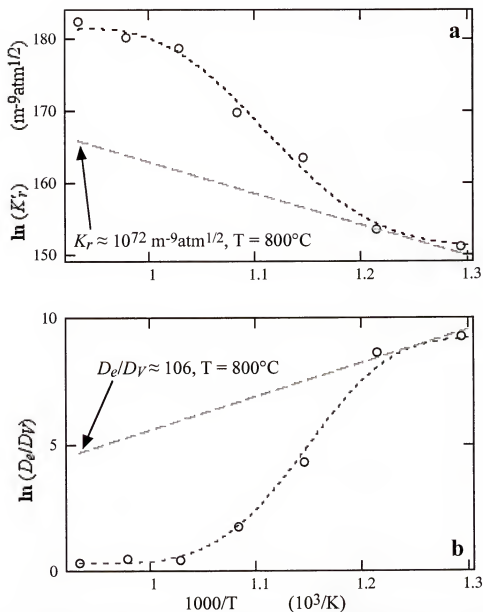
Figure 3-37. Plots of (a) K_r and (b) D_e/D_V versus reciprocal temperature. K_r and D_e/D_V values come from fitting the model in Figures 3-30 to 3-36. The dashed lines are for visual guidance and the straight lines indicate probable slopes without the impact of platinum electrodes, defect associates and electrode overpotential.
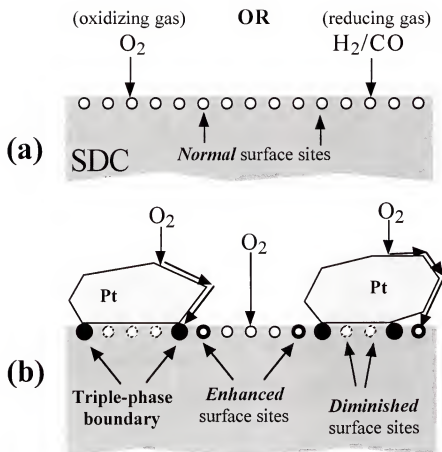
Figure 3-38. Comparison of the SDC-gas and SDC-Pt-gas interfaces showing: (a) *Normal* oxygen exchange surface sites for SDC in an oxidizing or a reducing gas, and (b) *Enhanced* and *diminished* oxygen exchange surface sites and triple phase (SDC-Pt-gas) boundaries.

them access to the gas phase or any adsorbed (non-electronic) species. (Indeed, dense platinum foil is often used as ion blocking electrodes in some experiments.)

At *high* temperatures the impact of the platinum (i.e., in spreading the effective area of the triple phase boundary by injecting electrons into the surface of the SDC and adsorbing gaseous species, which then migrate to the triple phase boundaries [74, 75]) is significant and, accordingly, oxygen exchange is higher than it would be for a bare SDC surface. Consequently, K_r, which is a measure of how easily oxygen is exchanged with the MIEC, appears to be greater than it would be for a bare ceria sample (Figure 3-38a)

which may explain the elevated K_r values obtained from fitting the model to the experimental data at temperatures $\geq 650\ °C$ (Figure 3-37a).

The heightened oxygen exchange induced by the platinum electrodes at the higher temperatures, causes an increase in the concentration of oxygen vacancies and electrons on the anode side of SDC. Accordingly, the concentration of defect associates increases (see section 2.4.4 and Figure 2-17). (This effect was not included in the models developed in this chapter because the values of the equilibrium constants associated with the defect association reaction, Eqs. (2.4.41) through (2.4.43), are unknown.)[25] By trapping the oxygen vacancies and electrons, the formation of the defect associates $\left(Sm'_{Ce} \circ V^{\bullet\bullet}_O \circ Sm'_{Ce}\right)^{\times}$ and $\left(Ce'_{Ce} \circ V^{\bullet\bullet}_O \circ Sm'_{Ce}\right)^{\times}$ reduces the oxygen permeation below what would be expected for the values of K_r, P_0 and P_L. Since the model has no provision for the formation of defect associates, it "interprets" the reduced oxygen permeation as a reduction in the electron diffusivity, i.e., a smaller D_e/D_V ratio (see Figure 3-37b).

As the temperature lowers, K_r for SDC decreases because the free energy for the oxygen release reaction, in Eq. (3.5.1), grows smaller. Secondly, at lower temperatures the electrolytic domain of SDC increases and, accordingly, the ability of SDC to incorporate electrons is reduced. This limits the spreading of the triple phase boundary, which takes place at higher temperatures, and so the impact of the platinum electrodes decreases. A third factor is that surface migration of adsorbed species important to the surface exchange reaction, may become rate limiting because of the reduction in thermal energy. Last, but not least, the decrease in available surface sites caused by platinum coverage on the SDC surface reduces the oxygen exchange below what it would be for a bare SDC surface (Figure 3-38a). Together, these (detrimental) electrode effects make the apparent K_r less than the K_r of a bare ceria sample. This may explain the (slightly) low K_r values obtained from fitting the model to the experimental data at temperatures $\leq 550\ °C$. The suitability

---

[25] Please note that the defect associate in Eq. (2.4.43) is exactly the neutral chemical species that migrates in the oxygen chemical potential gradient, see Figure 3.2 and section 3.4.2 and therefore will not be discussed.

(if not the validity) of this explanation is hard to justify at lower temperatures without independently obtained values for K_r and D_e/D_V. K_r may be estimated from Eq. (2.4.8) which gives $K_r\theta \approx 2.4 \times 10^{66}$ m^{-9}atm.$^{1/2}$ at 500 °C, but the magnitude of θ is unknown. Finally, a lower K_r also means lower concentrations of oxygen vacancies and electrons and, thus, defect associates[26].

At lower temperatures, the significance of electrode overpotentials increases and becomes just as important as the change in K_r. In *open-circuit* (I_{ext} = 0) conditions the dominant contributor to the electrode overpotential is slow electrocatalytic (charge transfer) reactions at the electrodes. At high temperatures, the electrocatalytic reactions are fast and the overpotential can be neglected. This is not true at lower temperatures. As temperatures decrease, the charge transfer rate at the interface slows causing an accumulation of charged oxygen species near the reaction sites. The accumulation creates an electric field that slows down and eventually stops other charged oxygen species from approaching the reaction sites. Thermodynamically, the material should still be able to reach thermodynamic equilibrium (i.e., the charge transfer reactions will take place if given enough time). However, if the reaction kinetics are slow enough, thermodynamic equilibrium will not be attained. Consequently, the effective oxygen potential gradient and, therefore, the *open-circuit* voltage, across the SDC membrane is less than that predicted by thermodynamics.

Where possible, electrodes are designed to minimize the overpotential. The platinum electrodes on the sensor are specially designed to optimize the performance of the sensor by minimizing the electrode overpotential. The simple porous platinum electrodes (made by applying a platinum paste) on the SDC membrane did not benefit from such optimization. Hence they produce a comparably larger overpotential, for similar conditions, than the electrodes on the commercial oxygen sensor, which are optimized. At

---

[26] The concentration of defect associates decreases with temperature but they are also harder to break up because of the correspondingly lower thermal energy available. Conversely, as the temperature increases the increased concentration of defect associates is counterbalanced by more thermal energy to break them apart.

high temperatures, one may expect that the differences between the electrodes are minimized as the electrocatalytic activity of the platinum dominates. However, as temperatures decrease, the differences between them increase. Thus, for the same conditions, the SDC membrane shows an *open-circuit* potential which (in comparison to the sensor) is reduced from theoretical by the electrode overpotential as well as oxygen permeation. Finally, this effect is exacerbated by the ability of SDC to pass an electronic current (increased surface interaction) which increases the potential drop across the electrode and the near surface region of the SDC membrane (i.e., the electrode overpotential). Conversely, YSZ does not allow an electronic current (decreased surface interaction) hence the electrode overpotential would be comparably larger for SDC, even for identical electrodes.

On the graphs in Figures 3-30 through 3-36 this effect would shift the points downward, "flattening" the curves. In the absence of the electrode overpotential, the curves would shift upwards. The model *interprets* the "flatter" curves as a lower value of K_r since the decreased charge transfer rate causing the overpotential also corresponds to a reduced ability of the membrane to exchange oxygen at its surface. Similarly, the reduced *open-circuit* potential, given the conditions—i.e., P_0 (from the sensor) and P_L (from thermodynamics) and T—is *interpreted* as being due to oxygen permeation hence the large D_e/D_V ratios obtained at lower temperatures; see Table 3-3.

Experimental Errors. The values of K_r in Table 3-3 show that the difference between K_r from the data of Kobayashi *et al.* [47] and that calculated from the model, at 800 °C is large. However, they also show that the corresponding values for $\ln K_r$ ($\propto \Delta G_r$) are within 10% of each other. The reason that this is significant is that the actual measured quantities in the experiment are voltage (Φ_{oc}) and temperature. Also Φ_{oc} is proportional to $\ln K_r$ as shown below:

$$\ln \frac{K_r}{K_r^*} = -\frac{\Delta G_r}{kT} = -\frac{2z_f q \Phi_{oc}}{kT} \tag{3.9.3}$$

Consequently, experimental errors made in the measurement of Φ_{oc} are magnified (exponentially) in the calculation of K_r. Moreover, from error analysis

$$\frac{\Delta_{err}\left(\ln\frac{K_r}{K_r^*}\right)}{\ln\frac{K_r}{K_r^*}} = \frac{\Delta_{err}\Phi_{oc}}{\Phi_{oc}} + \frac{\Delta_{err}T}{T} \tag{3.9.4}$$

where the symbol Δ_{err} indicates the error (so $\Delta_{err}y$ is the error in y). From the experiment done $\Delta_{err}\Phi_{oc}/\Phi_{oc}$ (i.e., the fractional error) is between ~0.05 and ~0.1 while $\Delta_{err}T/T$ lies between ~0.01 and ~0.05. Therefore, the fractional error in $\ln K_r/K_r^*$ falls in the range 0.06 to 0.15 (i.e., 6% to 15%). This result shows that if experimental errors are included, the K_r (or perhaps more appropriately $\ln K_r$) value obtained from Kobayashi *et al.* [47] approximately equal to that obtained from the Φ_{oc} experiments outlined above.

Finally, there is also the effect of the P_{O_2} range of in which the experiments were conducted. The data of Kobayashi *et al.* [47] (at 800 °C) spans a P_{O_2} range from ~10$^{-17.55}$ atm. to ~10$^{-20.5}$ atm. while for the same temperature the Φ_{oc} experiment spans a range of ~10^{-4} to ~10^{-19} atm. In addition, the data of Kobayashi *et al.* [47], in Table 2-8, shows an increasing trend for K_r as P_{O_2} decreases. Together, the implication is that had Kobayashi *et al.* [47] taken data over a larger range then, perhaps, a higher average K_r value would have been obtained from their data. This result is substantiated somewhat when the model is applied to the Φ_{oc} data using the K_r (and the corresponding D_e/D_V ratio) value calculated from the data of Kobayashi *et al.* [47] shown in Figure 3-39. The final data point, corresponding to $P_0 = $ ~10^{-19} atm., falls exactly on the modeled curve.

3.10. Summary

Models have been developed for the spatial distribution of defects and defect transport in *n*-type and *p*-type oxide MIECs. In developing the models, three typical
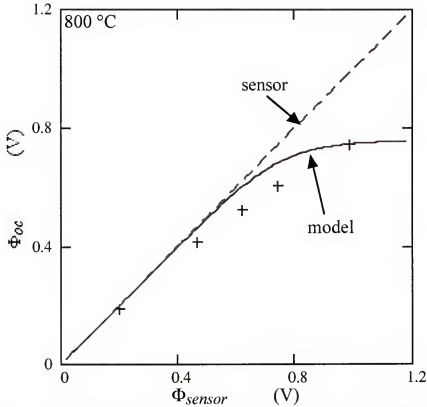
Figure 3-39. *Open-circuit* voltage, Φ_{oc}, versus Φ_{sensor} (Φ_{th}) at 800 °C without "fitting". The model (—) was fitted to experimental data (+) (sensor (---)) for the fuel cell using the K_r value obtained from the data of Kobayashi *et al.* [47] and the corresponding D_e/D_V ratio in Table 3-1.

assumptions were addressed namely:

    (a) uniformly distributed ionic species

    (b) *fixed* boundary conditions

and (c) constant electric field.

In sections 3.4 and 3.6 the assumption of uniformly distributed ionic species was shown to be unnecessary and incorrect. In sections 3.4 through 3.6 it demonstrated that the use of *fixed* boundary conditions leads to unrealistic defect distribution profiles and in some cases physically unjustified predictions especially for the variation defect flux and transference number with the potential across the MIEC, $\Delta\Phi$. Finally, the spatial

distribution of defects in an MIEC was modeled without assuming the electric field is independent of the positional variable x. At this point it should be clearly reiterated that this last achievement was attained previously by Liu [63]. However, the approach presented here is simpler and the constants are much more readily understood and accessible. Moreover, the plots Liu [63] presented were obtained from limiting cases (such as high or low acceptor-dopant concentrations) whereas the graphs obtained in section 3.8 were for more general conditions.

Irrespective of these accomplishments, one must, in fairness and the interest of good science, highlight the weaknesses of the model. The careful reviewer of this work will notice that in some situations the defect concentrations are inordinately high. This may readily be attributed in part to the need for more reliable values for constants such as K_r, D_e and D_V. However, it doesn't mask the possibility that in certain circumstances very high defect concentrations may exist. Hence, for a more complete model, one should be able to account for the possibility of defect association, which may greatly influence the spatial distribution profiles as well as defect transport. Also, because nature is at least three dimensional, explorations into the possibility and the necessity of expanding the models from their one-dimensional status may provide interesting revelations.

The need to account for defect association was brought into focus more distinctly when the model was applied to data for Φ_{oc} experiments. Excellent fits were obtained for fits to the experimental data. However, physical interpretation was hampered somewhat by the inability to account for defect association and to quantify the electrocatalytic effect of the platinum electrodes. Nonetheless, the exercise demonstrated the potential power of the model since unique values of K_r and D_e/D_V were obtained for the best fits.

CHAPTER 4
BILAYERED MEMBRANES

4.1   Introduction

Solid oxide fuel cells (SOFCs) have great potential for use in electrical power generation. Unfortunately, current SOFCs must operate at high temperatures (> 800 $^{\circ}$C) to deliver acceptable electric power. High temperatures demand (a) specialized (expensive) materials for the fuel cell interconnects and insulation, (b) time to heat up to the operating temperature and (c) energy input to arrive at the operating temperature. Therefore, if fuel cells could be designed to give a reasonable power output at intermediate[27] temperatures tremendous benefits may be accrued, not the least of which is reduced cost. The problem is that at lower temperatures the conductivity of the conventional solid oxide electrolyte, yttria-stabilized zirconia (YSZ), becomes too small to supply electrical current efficiently to an external load.

One potential solution for this problem is to replace YSZ with bismuth oxide. Bismuth oxide has the highest ionic conductivity of known solid oxide electrolytes, high enough that it could, in theory, deliver electrical power effectively at low temperatures. Unfortunately however, bismuth oxide decomposes at low (< ~10^{-13} atm.) oxygen partial pressures (P_{O_2}) in the presence of potential fuels such as hydrogen or methane, which are (necessarily) active reducing agents. Several attempts have been made to stabilize bismuth oxide [68, 69] in low oxygen partial pressures. Limited success has been achieved; but not enough to make it viable on its own.

---

[27]   The term intermediate temperatures is used here in accordance with current convention to mean temperatures in the range 500-700 $^{\circ}$C. The term intermediate is also used to distinguish SOFCs operating in the indicated temperature range from proton exchange membranes (PEMs) which, by current convention, are described as operating at low temperatures (i.e., ~ 100 $^{\circ}$C).
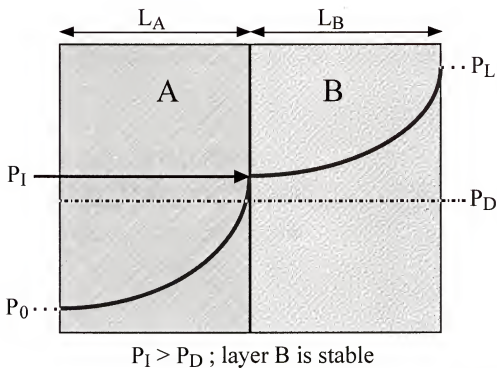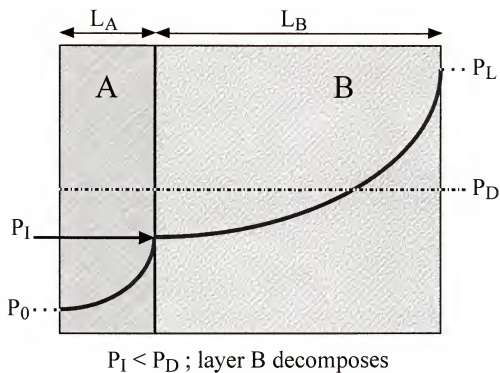
Figure 4-1. Conceptual representation of a bilayered solid oxide membrane showing the effect of relative thickness on interfacial P_{O_2}; P_D is the decomposition P_{O_2}.

Another potential solution is acceptor-doped ceria. Although not as conductive as bismuth oxide, it is the subject of much investigation as a potential intermediate temperature solid oxide electrolyte [32 - 35]. However, ceria is a mixed conductor (see Chapters 2 and 3) and in reducing atmospheres (low P_{O_2}) it displays significant n-type conduction. This diminishes the efficiency (defined in Chapter 3) of a ceria based SOFC enough to compromise its viability as an electrolyte (compare plots of efficiency versus operating voltage for SDC, in Figures 3-20 and 3-24, and ESB, in Figure 3-21).

A number of researchers [76 - 79] have investigated the possibility of using a bilayered electrolyte (see Figure 4-1) consisting of layers of YSZ and samaria or gadolinia-doped ceria (SDC or GDC). Some researchers [76, 79] proposed using a thin layer of YSZ on the fuel side of an SOFC to shield the SDC and thereby prevent its reduction by the fuel. Alternatively, those researchers [76, 79] have suggested placing the YSZ layer, which has a low electronic conductivity, on the air, (i.e., oxidizing) side of the SOFC where its function is only to block electronic flux (thereby increasing the efficiency of the SOFC). Of the two approaches the latter has been the most successful [76, 79]. However, in both cases the YSZ layer could not be made thin enough for the total ionic conductance of the bilayer to be high enough for efficient power generation at low temperatures. Generally, a YSZ\SDC or SDC\YSZ bilayer electrolyte has no intrinsic advantage over just a thin YSZ electrolyte itself, other than providing a non-porous substrate for YSZ deposition, due to the relatively low conductivity of YSZ.

Wachsman *et al.* [78] proposed a bilayered electrolyte consisting of a layer of erbia-stabilized bismuth oxide (ESB) on the oxidizing side and a layer of SDC or GDC on the reducing side. In this arrangement, the ceria layer would protect the bismuth oxide layer from decomposing by shielding it from very low P_{O_2}'s and the ESB layer would serve to block electronic flux. This arrangement has two significant advantages over the YSZ\SDC and SDC\YSZ bilayers. The first advantage is that both SDC and ESB are conductive enough by themselves to serve as intermediate temperature SOFC electrolytes.

Consequently, at worst an SDC\ESB bilayered SOFC should have the conductivity of SDC but with improved efficiency due to the electronic flux barrier provided by ESB. The second advantage is that small (dopant) concentrations of SDC in ESB or ESB in SDC, have been found to have conductivities comparable to the host lattice [68, 69, 80]. Therefore, if solid solutioning occurs at the SDC-ESB interface, it should not be detrimental to the performance of the bilayer (technically a tri-layer in that case). Contrastingly, solid solutions of SDC and YSZ have been found to be significantly less conductive than SDC or YSZ.

The disadvantage of the SDC\ESB bilayer is that ESB is disposed to decompose. Thus, it becomes important to have a way of assessing the stability of ESB in this arrangement for various fuel cell operating conditions. In fact, the primary issue for SDC\ESB bilayered electrolytes is optimizing the relative thickness of the SDC and ESB layers so that the oxygen partial pressure at the SDC-ESB interface is high enough to prevent decomposition of the ESB. In *open-circuit* conditions the stability of ESB must be determined by calculating (since direct measurement is not presently feasible) the effective P_{O_2} at the interface which as shown in Figure 4-1 is a function of the relative thicknesses of the layers. Ideally, the effective interfacial P_{O_2} should not fall below ~10^{-13} atm. (i.e., the P_{O_2} bismuth oxide below which decomposes) for the SDC\ESB bilayer. Under *closed-circuit* conditions one can no longer talk about an effective interfacial P_{O_2} since the oxygen is no longer permeating by ambipolar diffusion through the bilayer. Therefore, as shown later, other indicators of stability must be used.

In this chapter, the models developed in Chapters 2 and 3 are used to obtain the relationship between the thickness ratio of the constituent layers of the SDC\ESB bilayer and the interfacial conditions for various fuel cell operating conditions. By having such a relationship, the relative thickness of the SDC and ESB layers may be optimized to maximize total conductivity of the bilayer and the protection of ESB from decomposition under a range of operating conditions.

4.2. The Bilayer Model

4.2.1 *Open-Circuit* Conditions

Mechanistically, the diffusion of oxygen occurs by oxygen atoms jumping from an occupied site to an adjacent vacant site in the MIECs oxygen sub-lattice. Also, oxygen vacancies and electrons/electron holes travel together in an electrically neutral packet (see Figure 3-2), as discussed earlier in section 3.4.2. Consequently, the fluxes of the various species are related as follows:

$$2 z_V j_{O_2} = - z_V j_V = z_{e,h} j_{e,h} \tag{4.2.1}$$

For the bilayered electrolyte the flux of any species must be the same in both layers in steady state conditions. And, because of the relationships in Eq. (4.2.1), it is necessary to consider the flux of only one species. Therefore, for a bilayer consisting of an ε layer (SDC) and a δ layer (ESB), one may write:

$$j_{O_2}^{\varepsilon} = j_{O_2}^{\delta} \tag{4.2.2a}$$

$$j_V^{\varepsilon} = j_V^{\delta} \tag{4.2.2b}$$

or

$$z_{e,h} j_{e,h}^{\varepsilon} = z_{e,h} j_{e,h}^{\delta} \tag{4.2.2c}$$

where the superscript denotes the layer. At this point two approaches may be taken. An expression for j_V may be obtained from Eq. (2.4.39) which was derived from a combination of the thermodynamic model developed in Chapter 2 and Wagner's equation [53], Eq. (2.4.38). Alternatively, j_V may be obtained from Eq. (3.4.14) which was obtained by solving the transport laws outlined in sections 3.3 and 3.4.2. Both

approaches are used and the results compared below. One may expect that the expression for j_V in Eq. (3.4.14) is inherently more accurate than Eq. (2.4.39) since fewer assumptions were made in its development. Thus, the accuracy of the models developed in Chapter 2 for the functional dependence of defect concentration on P_{O_2} may, indirectly, be validated by comparing the results of both approaches.

4.2.1.1 "Thermodynamic" approach

From Eqs. (2.4.9), (2.4.10), (2.4.32), (2.4.33) and (3.3.1), the oxygen vacancy and electron conductivity of the n-type MIEC, SDC, as a function of P_{O_2}, is given by[28]

$$\sigma_V(P) = z_V^2 q^2 \frac{D_V}{kT} \left[\frac{3}{4} K_r^{\frac{1}{2}} P^{-\frac{1}{4}} + \left(\frac{1}{2} c_A \right)^{\frac{3}{2}} \right]^{\frac{2}{3}} \tag{4.2.3}$$

and

$$\sigma_e(P) = z_e^2 q^2 \frac{D_e}{kT} K_r^{\frac{1}{2}} P^{-\frac{1}{4}} \left[\frac{3}{4} K_r^{\frac{1}{2}} P^{-\frac{1}{4}} + \left(\frac{1}{2} c_A \right)^{\frac{3}{2}} \right]^{-\frac{1}{3}} \tag{4.2.4}$$

where σ is conductivity, P is oxygen partial pressure, K_r is an external equilibrium constant—see Eq. (2.3.2), (2.4.1) or (3.5.1)—c is concentration, D is diffusivity, q is the elementary charge on an electron, z is the charge equivalence, k is Boltzmann's constant and T is temperature; the subscripts "V", "e" and "A" refer to oxygen vacancies, electrons and the acceptor dopant respectively.

Similarly, from Eqs. (2.3.41), (2.3.43), (2.4.32) and (3.3.1), the oxygen vacancy and electron-hole conductivity of the p-type MIEC, ESB, as a function of P_{O_2}, is given by[29]

---

[28] For $P_{O_2} < \sim 1$ atm. SDC may be considered to be in the low P_{O_2} region as discussed in chapter 2. Therefore, Eqs. (2.4.9) and (2.4.10) adequately describe the defect concentration dependence on P_{O_2}.

[29] For $\sim 10^{-13}$ atm. $< P_{O_2} < \sim 1$ atm., ESB may be considered to be in the intermediate P_{O_2} region as discussed in chapter 2. Therefore, Eqs. (2.3.41) and (2.3.43) adequately describe the defect concentration dependence on P_{O_2}.

$$\sigma_V(P) = \frac{z_V^2 q^2 D_V}{16kT} \left[\left(K_m P^{\frac{1}{2}} + 8c_A \right)^{\frac{1}{2}} - K_m^{\frac{1}{2}} P^{\frac{1}{4}} \right]^2 \qquad (4.2.5)$$

and

$$\sigma_h(P) = \frac{z_h^2 q^2 D_h}{4kT} \left(-K_m P^{\frac{1}{2}} + \sqrt{8c_A K_m P^{\frac{1}{2}} + K_m^2 P} \right) \qquad (4.2.6)$$

where K_m is an external equilibrium constant—see Eq. (2.3.3) or (3.5.4)—and the subscript "h" refers to electron-holes. It should also be noted that in applying these formulae to ESB the erbium and bismuth cations are treated as aliovalent acceptor "dopants" sitting in a fluorite lattice [70]. A formal development of this approach is presented in Appendix C.

Wagner's equation for oxygen flux—Eq. (2.4.38)—may be combined with Eq. (4.2.1) with the result

$$-j_{O_2} = \frac{kT}{4^2 q^2 \mathcal{L}^\varepsilon} \cdot \int_{P_0}^{P_I} \frac{\sigma_V^\varepsilon(P)\sigma_e^\varepsilon(P)}{\sigma_V^\varepsilon(P) + \sigma_e^\varepsilon(P)} \cdot \frac{dP}{P} = \frac{kT}{4^2 q^2 \mathcal{L}^\delta} \cdot \int_{P_I}^{P_L} \frac{\sigma_V^\delta(P)\sigma_h^\delta(P)}{\sigma_V^\delta(P) + \sigma_h^\delta(P)} \cdot \frac{dP}{P} \qquad (4.2.7a)$$

which may be rewritten as

$$\tau(P_I) = \frac{\mathcal{L}^\varepsilon j_{O_2}^\delta}{\mathcal{L}^\delta j_{O_2}^\varepsilon} = \frac{\mathcal{L}^\varepsilon}{\mathcal{L}^\delta} = \frac{\displaystyle\int_{P_0}^{P_I} \frac{\sigma_V^\varepsilon(P)\sigma_e^\varepsilon(P)}{\sigma_V^\varepsilon(P) + \sigma_e^\varepsilon(P)} \cdot \frac{dP}{P}}{\displaystyle\int_{P_I}^{P_L} \frac{\sigma_V^\delta(P)\sigma_h^\delta(P)}{\sigma_V^\delta(P) + \sigma_h^\delta(P)} \cdot \frac{dP}{P}} \qquad (4.2.7b)$$

where τ is defined as the thickness ratio of the two layers, L is the thickness (i.e., length) of a layer and the subscripts "0" and "L" refer to the conditions at $x = 0$ (low P_{O_2} or fuel/reducing side of the SOFC/electrolyte) and $x = L$ (high P_{O_2} or air/oxidizing side of the

SOFC/electrolyte); the subscript "I" refers to the interface between the two constituent layers.

The integral in the numerator of Eq. (4.2.7) was obtained previously in section 2.4.3.2 and the result given in Eq. (2.4.39). The integral in the denominator exists but it is very unwieldy. For ESB, $K_m = 3.2 \times 10^{23}$ m^{-3}atm.$^{-1/2}$ and $c_A = 2.2 \times 10^{28}$ m^{-3} (see **section 3.6**), consequently, in the range of P_{O_2} under investigation (10^{-20} atm. to 0.21 atm.)

$$8c_A >>> K_m P^{1/2}$$

and Eqs. (4.2.5) and (4.2.6) reduce to

$$\sigma_V(P) = \frac{z_V^2 q^2 D_V c_A}{2kT} \tag{4.2.5b}$$

and

$$\sigma_h(P) = \frac{z_h^2 q^2 D_h}{kT} K_m^{\frac{1}{2}} P^{\frac{1}{4}} \left(\tfrac{1}{2} c_A\right)^{\frac{1}{2}} \tag{4.2.6b}$$

With this simplification the denominator in Eq. (4.2.7) is easily integrated and Eq. (4.2.7) becomes

$$\tau(P_I) = \frac{\dfrac{z_e^2 D_e^\varepsilon}{1+\frac{4}{3}\Theta^\varepsilon}\left\{\begin{array}{l}\left.\dfrac{c_V^\varepsilon(P)}{2} - \dfrac{\Omega^2}{6}\ln\dfrac{c_V^\varepsilon(P) - \Omega\sqrt{c_V^\varepsilon(P)} + \Omega^2}{\left(\sqrt{c_V^\varepsilon(P)} + \Omega\right)^2}\right.\\[2ex] \left.-\dfrac{\Omega^2}{\sqrt{3}}\tan^{-1}\dfrac{2\sqrt{c_V^\varepsilon(P)} - \Omega}{\Omega\sqrt{3}}\right|_{P_0}^{P_I}\end{array}\right\}}{-\dfrac{z_h^2 D_h^\delta c_A^\delta}{8\Theta^\delta}\cdot\left\{\ln\left(1 + \Theta^\delta\left(\tfrac{1}{2}c_A^\delta\right)^{-\frac{1}{2}} K_m^{\frac{1}{2}} P^{\frac{1}{4}}\right)\right|_{P_I}^{P_L}\right\}} \tag{4.2.7c}$$

where

$$\Omega = -\tfrac{4}{3}\Theta^{\frac{1}{3}}\left(\tfrac{1}{2}c_A^{\varepsilon}\right)^{\frac{1}{2}}\left(1+\tfrac{4}{3}\Theta\right)^{-\frac{1}{3}} \tag{4.2.8}$$

$$\Theta^{\varepsilon,\delta} = \frac{z_{e,h}^2 D_{e,h}}{z_V^2 D_V} \tag{4.2.9}$$

and, from Eq. (2.4.9),

$$c_V^{\varepsilon}(P) = \left[\tfrac{3}{4}K_r^{\frac{1}{2}}P^{-\frac{1}{4}} + \left(\tfrac{1}{2}c_A^{\varepsilon}\right)^{\frac{3}{2}}\right]^{\frac{2}{3}} \tag{4.2.10}$$

As in section 3.6, it is assumed that: $D_V(\text{SDC}) \approx D_V(\text{ESB}) = D_V$ and $D_e(\text{SDC}) \approx D_h(\text{ESB}) = D_{e,h}$; $c_A^{\varepsilon} = 5 \times 10^{27}$ m^{-3}, $c_A^{\delta} = 22 \times 10^{27}$ m^{-3}, $P_L = 0.21$ atm. and $P_0 = 10^{-20}$ atm. These values are used throughout this chapter.

4.2.1.2 "Transport" approach

From Eq. (3.4.14)

$$j_V = \frac{D_V D_{e,h}}{L}\left[\frac{\left(z_V - z_{e,h}\right)\left(c_{V_0} - c_{V_L}\right)}{z_V D_V - z_{e,h}D_{e,h}} + \frac{z_{e,h}\left(D_{e,h} - D_V\right)c_A}{\left(z_V D_V - z_{e,h}D_{e,h}\right)^2}\ln\frac{z_V^2 D_V c_{V_L} + D_{e,h}c_{e,h_L}}{z_V^2 D_V c_{V_0} + D_{e,h}c_{e,h_0}}\right] \tag{4.2.11}$$

Combining this equation with Eq. (4.2.1) and rearranging yields

$$\tau(P_I) = \frac{D_V^{\varepsilon}D_e^{\varepsilon}\left[\dfrac{\left(z_V - z_e\right)\left(c_{V_0}^{\varepsilon} - c_{V_L}^{\varepsilon}\right)}{z_V D_V^{\varepsilon} - z_e D_e^{\varepsilon}} + \dfrac{z_e\left(D_e^{\varepsilon} - D_V^{\varepsilon}\right)c_A^{\varepsilon}}{\left(z_V D_V^{\varepsilon} - z_e D_e^{\varepsilon}\right)^2}\ln\dfrac{\left(z_V D_V^{\varepsilon} - z_e D_e^{\varepsilon}\right)z_V c_{V_L}^{\varepsilon} + z_e D_e^{\varepsilon}c_A^{\varepsilon}}{\left(z_V D_V^{\varepsilon} - z_e D_e^{\varepsilon}\right)z_V c_{V_0}^{\varepsilon} + z_e D_e^{\varepsilon}c_A^{\varepsilon}}\right]}{D_V^{\varepsilon}D_h^{\delta}\left[\dfrac{\left(z_V - z_h\right)\left(c_{V_I}^{\delta} - c_{V_L}^{\delta}\right)}{z_V D_V^{\varepsilon} - z_h D_h^{\delta}} + \dfrac{z_h\left(D_h - D_V^{\delta}\right)c_A^{\delta}}{\left(z_V D_V^{\varepsilon} - z_h D_h^{\delta}\right)^2}\ln\dfrac{\left(z_V D_V^{\varepsilon} - z_h D_h^{\delta}\right)z_V c_{V_L}^{\delta} + z_h D_h^{\delta}c_A^{\delta}}{\left(z_V D_V^{\varepsilon} - z_h D_h^{\delta}\right)z_V c_{V_I}^{\delta} + z_h D_h^{\delta}c_A^{\delta}}\right]} \tag{4.2.12}$$

where

$$c_{V_k}^{\varepsilon}(P_k) = \left[\frac{3}{4} K_r^{\frac{1}{2}} P_k^{-\frac{1}{4}} + \left(\frac{1}{2} c_A^{\varepsilon} \right)^{\frac{3}{2}} \right]^{\frac{2}{3}}$$ (4.2.13)

and

$$c_{V_k}^{\delta}(P_k) = \frac{1}{16} \left[\left(K_m P_k^{\frac{1}{2}} + 8c_A^{\delta} \right)^{\frac{1}{2}} - K_m^{\frac{1}{2}} P_k^{\frac{1}{4}} \right]^2$$ (4.2.14)

and the subscript $k = 0, I, L$.

In Figures 4-2 and 4-3 are plots of τ versus log P_I in *open-circuit* conditions. As in section 3.6, at 800 °C, $D_V = 4.3 \times 10^{-12}$ m^{2}V^{-1}s^{-1} [49], $\Theta = 26.4$, $K_r = 9.97 \times 10^{71}$ m^{-9}atm.$^{1/2}$ [47], $K_m = 3.2 \times 10^{23}$ m^{-3}atm.$^{-1/2}$. Figure 4-2a shows very close agreement (enough, perhaps, to be indistinct experimentally) between the "thermodynamic" model—Eq. (4.2.7c)—and the "transport" model—Eq. (4.2.12)—giving credence to the propriety of both approaches. From the graph, the optimum thickness ratio, τ^*, to prevent decomposition of the ESB layer—ESB decomposes for $P_I \leq \sim10^{-13}$ atm. at 800 °C—at the SDC-ESB interface, is ~7.8. That is, the SDC layer needs to be at least 7.8 times thicker than the ESB layer to protect it in *open-circuit* conditions. Samaria-doped ceria is more electronically conductive than ESB and so it permeates oxygen by ambipolar diffusion more easily. If the layers had the same thickness, the chemical potential drop would be greater across the more *resistive* layer (analogous to an electrical circuit). Consequently, to increase the chemical potential drop across the SDC layer and offer protection to the ESB layer requires a thickening of the SDC layer relative to the ESB layer.

Given that $\tau = L^{\varepsilon}/L^{\delta}$, the total resistance of the bilayer, R_{tot}, where the cross-sectional area, S, is the same for both layers, is given by:
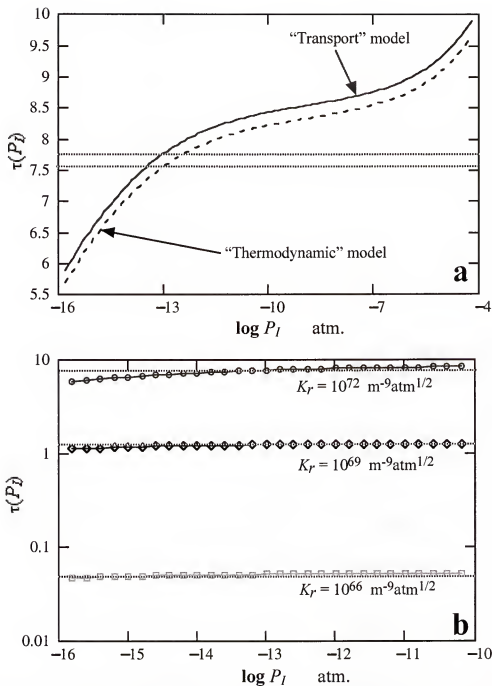
Figure 4-2. Thickness ratio dependence on interfacial P_{O_2} in *open-circuit* conditions at 800 °C. A comparison of transport and thermodynamic approaches is provided in (a)—where $K_r = 10^{72}$ m^{-9}atm.$^{1/2}$—and different materials are *simulated* by changing the K_r value for the SDC layer in (b).

$$R_{tot} = S\left(\frac{\mathcal{L}^\varepsilon}{\sigma^\varepsilon} + \frac{\mathcal{L}^\delta}{\sigma^\delta}\right) = S\left(\frac{\sigma^\delta + \sigma^\varepsilon\dfrac{1}{\tau}}{\sigma^\varepsilon\sigma^\delta}\right)\mathcal{L}^\varepsilon \qquad (4.2.15)$$

However, given $\tau^* \approx 8$

$$L = \mathcal{L}^\varepsilon + \mathcal{L}^\delta = \left(1 + \frac{1}{\tau}\right)\mathcal{L}^\varepsilon \approx \mathcal{L}^\varepsilon$$

where L is the length of the bilayer. Therefore, since $\sigma_{ESB}/\sigma_{SDC} \approx 4$, and $\tau^* \approx 8$ and

$$R_{tot} \approx S\left(\frac{1}{\sigma^\varepsilon}\right)\mathcal{L}^\varepsilon \approx S\left(\frac{1}{\sigma^\varepsilon}\right)L$$

In other words, the total resistance of the bilayer is, effectively, the resistance of the SDC layer alone (i.e., the ESB layer has a negligible effect on the resistance of the bilayer). While this result is not ideal, it is still has promise because the ESB layer blocks the conduction of electrons through the bilayer and, thereby, increases efficiency of power delivery to an external load compared to SDC alone—see Figures 3-20, 3-21 and 3-24.

In Figure 4-2b K_r was reduced (thereby decreasing the electron concentration) artificially (for SDC) to demonstrate the effect a less permeable layer (on the fuel side) would have on τ^*. As expected, the introduction of a less permeable (more *resistive*) layer decreases the chemical potential drop across the ESB layer, thereby reducing τ^*. Hence, if a material with comparable (or better) ionic conductivity to SDC, but lower electronic conductivity (and therefore lower oxygen permeability) could be found it should offer protection to the ESB layer at a smaller τ^*. Moreover, if τ^* is small enough, then the conductance of the bilayer would begin to approach that of a single ESB layer. One such material, currently under much investigation, is lanthanum gallate ($LaGaO_3$). Above ~700 °C, lanthanum gallate has a higher ionic conductivity than SDC and negligible
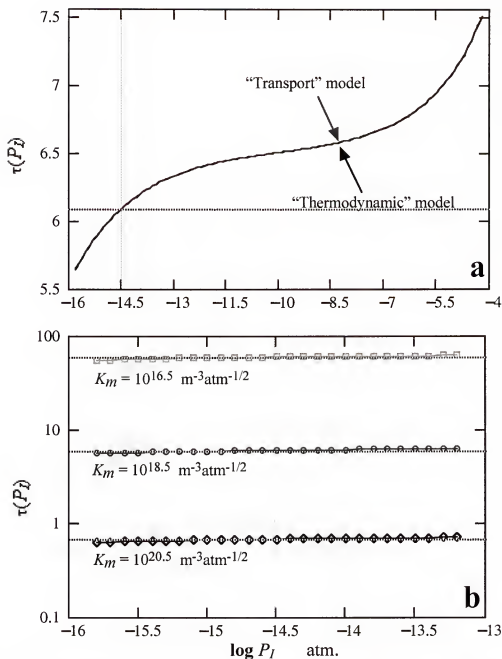
178

Figure 4-3. Thickness ratio dependence on interfacial P_{O_2} in *open-circuit* conditions at 500 °C. A comparison of transport and thermodynamic approaches is provided in (a)—where $K_r = 10^{72}$ m^{-9}atm.$^{1/2}$—and different estimates of K_m are compared in (b).

electronic conductivity [81, 82]. Indeed, it is a candidate SOFC electrolyte by itself. However, currently researchers are having difficulty finding compatible cathode materials (i.e., on the air side) for lanthanum gallate. This problem could, potentially, be alleviated by putting it in a bilayer configuration with an ESB layer on the air side of the SOFC.

Finally, if K_r (for SDC) decreases more rapidly with temperature than K_m (for ESB), and Θ remains approximately the same for both, then as T decreases, permeability of SDC would decrease more rapidly than ESB allowing SDC to offer protection to the ESB layer for a smaller τ^*. This scenario is depicted in Figure 4-3 where τ is plotted against log P_I at 500 °C. K_r ($= 4.0 \times 10^{65}$ m^{-9}atm.$^{1/2}$) and Θ (≈ 2500) were obtained from the experimental values used in section 3.9 (see Table 3-3) while K_m ($\approx 3.2 \times 10^{18}$ m^{-3}atm.$^{-1/2}$) was estimated from Eq. (3.4.17) assuming $\Phi_{oc}/\Phi_{th} \approx 0.996$ for ESB at 500 °C. Since ESB decomposes at $P_I \leq \sim 10^{-14.5}$ atm. at 500 °C, Figure 4-3a shows that the SDC layer should be at least 6.1 times the thickness of the ESB layer, i.e., $\tau^* \approx 6.1$. While this is an improvement over 800 °C it is still too thick to lower the total resistance of the bilayer much beyond the layer of SDC alone. As always, the accuracy of the results is heavily dependent on the accuracy of K_r, K_m and Θ. Figure 4-3b shows the effect different estimates of K_m would have on τ, which may be a small as ~ 0.7 (for $K_m \approx 3.2 \times 10^{16}$ m^{-3}atm.$^{-1/2}$) or as large as ~ 60 (for $K_m \approx 3.2 \times 10^{20}$ m^{-3}atm.$^{-1/2}$).

4.2.2 *Closed-Circuit* Conditions

For *closed-circuit* conditions, the principles and procedure are almost identical to those described and developed in the preceding sections for *open-circuit* conditions. However, there is one major difference: in *closed-circuit* conditions, oxygen does not permeate through the MIEC by ambipolar diffusion. In *closed-circuit* conditions, oxygen transport occurs via ions (oxygen vacancies). Consequently, one can no longer speak of a P_{O_2} at the interface (nor at any other point in either MIEC). Since there is no longer a P_{O_2} at the interface, a new gauge is required to indicate the stability of the ESB layer.

In *open-circuit* conditions there is an oxygen chemical potential difference across each layer (equivalent to a difference in P_{O_2}). In *closed-circuit* conditions the oxygen chemical potential difference still exists between $x = 0$ and $x = L$, however inside any layer (i.e., for $0 < x < L$) it is replaced by defect chemical potential differences and electrical potential differences. Additionally, the electric potential is a function of the defect concentration (and therefore the defect chemical potential) as shown in Eqs. (3.7.3), (3.7.11) and (3.7.13). Altogether, this suggests that in *closed-circuit* conditions, the electric potential difference across the ESB layer should be a suitable gauge of the stability of ESB at the SDC-ESB interface. At 800 °C, and with air on one side of an ESB electrolyte, it decomposes on the fuel side when at a P_{O_2} of $\sim 10^{-13}$ atm. This corresponds to a (Nernst) potential difference of ~ 0.66 V. It is arguable, therefore that if the electrical potential difference across the ESB layer (with air on the oxidizing side) is kept below 0.6 V then the ESB remains stable. In addition, it is known that [83, 84] an ESB (and other compounds) sample can be made to decompose in air, and in the absence of a P_{O_2} gradient, by applying a sufficiently large voltage across it.

To obtain an expression for $\tau(\Delta\phi)$ in *closed-circuit* conditions, consider Eqs. (3.7.10) and (3.7.11)

$$-\frac{j_V}{D_V} + \frac{j_{e,h}}{D_{e,h}} = \frac{z_V - z_{e,h}}{z_{e,h}}\gamma = \frac{z_V - z_{e,h}}{z_{e,h}} \cdot \frac{\phi_L - \phi_0 + \lambda\left(c_{V_0} - c_{V_L}\right)}{\lambda L} \quad (4.2.16)$$

$$\phi_L - \phi_0 = \frac{z_V\frac{j_V}{D_V} + z_{e,h}\frac{j_{e,h}}{D_{e,h}}}{z_V\left(z_V - z_{e,h}\right)f\gamma}\ln\frac{c_{V_L} + \frac{j_V}{z_V D_V f\lambda\gamma}}{c_{V_0} + \frac{j_V}{z_V D_V f\lambda\gamma}} \quad (4.2.17)$$

where, ϕ is potential, $f = q/k_B T$ and

$$\lambda = \frac{z_V - z_{e,h}}{z_{e,h}c_A f} \quad (4.2.18)$$

Since the ESB layer is a poor electronic conductor it blocks the flux of electrons and holes. Additionally, as one moves away from *open-circuit* conditions, the electronic flux inside the MIEC decreases (see Figures 3-16, 3-17 and 3-22). Hence, Eqs. (4.2.16) and (4.2.17) reduce to

$$-\frac{j_V}{D_V} \approx \frac{z_V - z_{e,h}}{z_{e,h}}\gamma = \frac{z_V - z_{e,h}}{z_{e,h}} \cdot \frac{\phi_L - \phi_0 + \lambda\left(c_{V_0} - c_{V_L}\right)}{\lambda L} \qquad (4.2.16b)$$

and

$$\phi_L - \phi_0 \approx \frac{z_V j_V}{z_V\left(z_V - z_{e,h}\right)D_V f\gamma}\ln\frac{c_{V_L} + \dfrac{j_V}{z_V D_V f\lambda\gamma}}{c_{V_0} + \dfrac{j_V}{z_V D_V f\lambda\gamma}} = -\frac{1}{z_{e,h}f}\ln\frac{c_{V_L} - \dfrac{c_A}{z_V}}{c_{V_0} - \dfrac{c_A}{z_V}} \qquad (4.2.17b)$$

Combining Eqs. (4.2.1), (4.2.16b) and (4.2.17b) yields

$$\tau(\Delta\phi) = \frac{D_V^\varepsilon \dfrac{z_V - z_e}{z_e}\left\{\dfrac{\Delta\phi^\varepsilon}{\lambda^\varepsilon} + \left(c_{V_0}^\varepsilon - \dfrac{c_A^\varepsilon}{z_V}\right)\left[1 - \exp\left(-z_e/\Delta\phi^\varepsilon\right)\right]\right\}}{D_V^\delta \dfrac{z_V - z_h}{z_h}\left\{\dfrac{\Delta\phi^\delta}{\lambda^\delta} - \left(c_{V_L}^\delta - \dfrac{c_A^\delta}{z_V}\right)\left[1 - \exp\left(z_h/\Delta\phi^\delta\right)\right]\right\}} \qquad (4.2.19)$$

where

$$\Delta\phi^\varepsilon = \phi_I - \phi_0 \qquad (4.2.20)$$

and

$$\Delta\phi^\delta = \phi_L - \phi_I \qquad (4.2.21)$$

Additionally, by definition (see Chapter 3)

$$\Delta\Phi = -\Delta\phi = -\left(\phi_L - \phi_0\right) \tag{4.2.22}$$

where $\Delta\Phi$ is the potential across a single layered electrolyte. Therefore, for the bilayer one may write

$$\Delta\Phi = \Delta\Phi^\varepsilon + \Delta\Phi^\delta = -\left(\phi_I - \phi_0\right) - \left(\phi_L - \phi_I\right) = -\Delta\phi^\varepsilon - \Delta\phi^\delta \tag{4.2.23}$$

Substituting Eq. (4.2.23) for $-\Delta\phi^\varepsilon$, into Eq. (4.2.19) yields

$$\tau(\Delta\phi^\delta) = -\frac{D_V^\varepsilon \dfrac{z_V - z_e}{z_e} \left\{ \dfrac{\Delta\Phi + \Delta\phi^\delta}{\lambda^\varepsilon} - \left(c_{V_0}^\varepsilon - \dfrac{c_A^\varepsilon}{z_V}\right)\left[1 - \exp\left(z_e \big/ \left(\Delta\Phi + \Delta\phi^\delta\right)\right)\right]\right\}}{D_V^\delta \dfrac{z_V - z_h}{z_h} \left\{ \dfrac{\Delta\phi^\delta}{\lambda^\delta} - \left(c_{V_L}^\delta - \dfrac{c_A^\delta}{z_V}\right)\left[1 - \exp\left(z_h / \Delta\phi^\delta\right)\right]\right\}} \tag{4.2.24}$$

Finally, from Eqs. (3.5.11) and (3.5.12), the external equilibrium constants K_r and K_m—Eqs. (4.2.13) and (4.2.14)—are functions of $\Delta\Phi^\varepsilon$ and $\Delta\Phi^\delta$ respectively (discussed previously in sections 3.5 and 3.6) and are given by

$$K_r(\Delta\Phi) = K_r^* \exp\left(-\frac{\Delta G_r \pm z_e q \Delta\Phi}{kT}\right) \tag{4.2.25}$$

and

$$K_m(\Delta\Phi) = K_m^* \exp\left(-\frac{\Delta G_m \pm z_h q \Delta\Phi}{kT}\right) \tag{4.2.26}$$

In Figures 4-4 and 4-5 are plots of τ versus $-\Delta\phi^\delta$ in *closed-circuit* conditions for various operating conditions. At the upper limit $\Delta\Phi = \Phi_{th}$ (i.e., *short-circuit* conditions, as discussed in section 3.6) and at the lower limit $\Delta\Phi = 0.25\Phi_{th}$. Figures 4-4b and 4-5b are magnifications of the region of most interest in Figures 4-4a and 4-5a respectively.
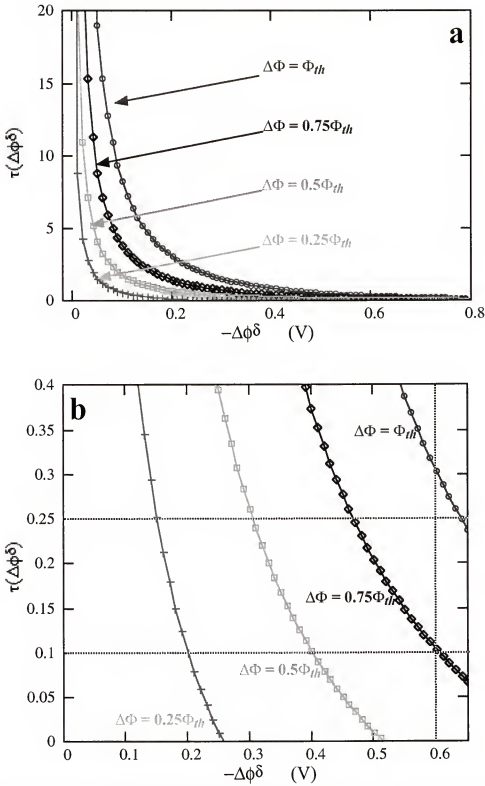
Figure 4-4. Thickness ratio versus potential difference across the ESB layer in *closed-circuit* conditions at 800 °C; (b) is a magnification of (a).
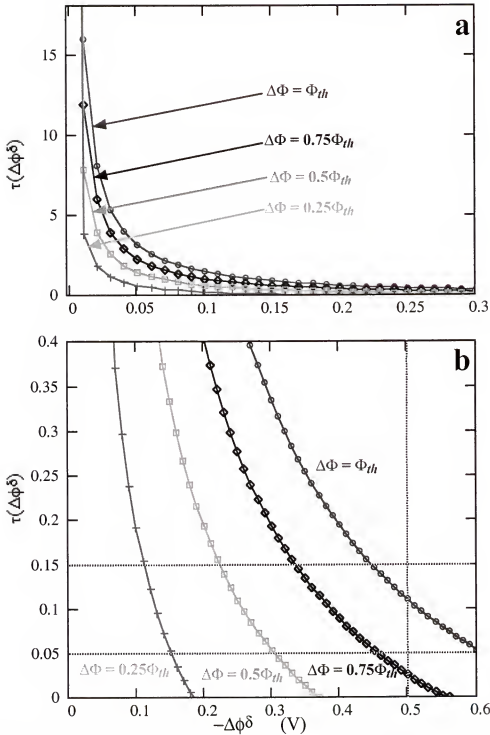
Figure 4-5. Thickness ratio versus potential difference across the ESB layer in *closed-circuit* conditions at 500 °C; (b) is a magnification of (a).

Figures 4-4 and 4-5 show that the optimum thickness ratio, τ^*, to prevent decomposition of the ESB layer, in *closed-circuit* conditions—ESB decomposes for $-\Delta\phi^\delta \geq \sim 0.6$ V at 800 °C and $-\Delta\phi^\delta \geq \sim 0.5$ V at 500 °C —is a function of the operating conditions. If the internal electronic current (the *leakage* current, I_e) is small, then external current (I_{ext}) is directly proportional to the internal ionic current (I_V)—see sections 3.3.2, 3.6.3 and Figures 3-1, 3-18, 3-19 and 3-23. Therefore, the largest values of $\Delta\Phi$ and $-\Delta\phi$ occur in *short-circuit* conditions because that is the point at which the external circuit draws the largest current from the fuel cell—and I_e is the smallest.

In this context, τ^* is then the optimal thickness ratio with respect to short-circuit conditions. Accordingly, Figure 4-4 shows that, at 800 °C, $\tau^* \approx 0.25$ while Figure 4-5 shows $\tau^* \approx 0.11$ at 500 °C. That is, in *closed-circuit* conditions, the SDC layer needs to be at least 0.25 the thickness of the ESB layer to protect it at 800 °C. At 500 °C the SDC layer needs to be at least 0.11 the thickness of the ESB layer to protect it. This is in stark contrast to the results obtained above for *open-circuit* conditions in Figures 4-2 and 4-3. The difference however is readily explained by considering that in *open-circuit* conditions ESB is more *resistive* than SDC to the transport (ambipolar diffusion) of oxygen because of the low concentration of electronic species in ESB.

However, in *closed-circuit* conditions (where the ionic and electronic species are no longer constrained to travel together) SDC is more resistive than ESB to the transport of oxygen vacancies because ESB has a higher concentration of oxygen vacancies than SDC. Hence, if the layers had the same thickness, there would be a larger electrical potential drop across the SDC layer. So to allow a larger voltage drop (up to 0.6 V at 800 °C or up to 0.53 V at 500 °C) across the ESB layer, the thickness of the SDC layer must be reduced relative to that of the ESB layer.

For $\tau = L^\varepsilon/L^\delta \approx 0.25$ (i.e., at 800 °C)

$$L = L^\varepsilon + L^\delta = \left(1 + \frac{1}{\tau}\right)L^\varepsilon \approx 5L^\varepsilon$$

Therefore, for $\sigma_{ESB}/\sigma_{SDC} \approx 4$ the total resistance of the bilayer (at 800 °C), calculated from Eq. (4.2.15), for *closed-circuit* conditions is roughly

$$R_{tot} \approx 2.5 \mathcal{S}\left(\frac{1}{\sigma^\epsilon}\right)L^\epsilon \approx \frac{2}{3} \mathcal{S}\left(\frac{1}{\sigma^\epsilon}\right)L$$

Similarly, for $\tau = L^\epsilon/L^\delta \approx 0.11$ (i.e., at 500 °C)

$$L = L^\epsilon + L^\delta = \left(1 + \frac{1}{\tau}\right)L^\epsilon \approx 11 L^\epsilon$$

Therefore, for $\sigma_{ESB}/\sigma_{SDC} \approx 4$ the total resistance of the bilayer (at 500 °C), calculated from Eq. (4.2.15), for *closed-circuit* conditions is roughly

$$R_{tot} = 3.5 \mathcal{S}\left(\frac{1}{\sigma^\epsilon}\right)L^\epsilon = \frac{3.5}{11} \mathcal{S}\left(\frac{1}{\sigma^\epsilon}\right)L$$

In other words, because of the lower τ^* obtained for *closed-circuit* conditions, the total resistance of the bilayer is reduced to ~40% at 800 °C and ~30% at 500 °C, of the resistance of a single SDC layer of the same thickness . These results are much closer to ideal because of the presence of the ESB layer which blocks electronic flux (leakage current) through the bilayer and gives a smaller total resistance than a single SDC layer of thickness L. Consequently, high current and power efficiencies (see Eqs. (3.6.2) and (3.6.3)) should be expected for an SOFC with a bilayered SDC\ESB electrolyte.

Figure 4-6 shows the concentration of oxygen vacancies in ESB at the SDC-ESB interface (Figure 4-3a) and at $x = L$, the solid-gas interface (Figure 4-4b). In similar fashion to Figures 3-10 and 3-13, Figure 4-6b shows that the c_{V_L} decreases as the $\Delta\Phi$ increases. The reverse trend is observed for c_{V_I} in Figure 4-6a, which instead bears resemblance to c_{V_0} in Figures 3-8, 3-12 and 3-27. This is a result of the direction and size of $\Delta\phi^\delta$. As $\Delta\phi^\delta$ gets larger c_{V_I} becomes constant and equal to $1/2\, c_A^\delta$ (1.1 x 10^{28} m^{-3}) as in
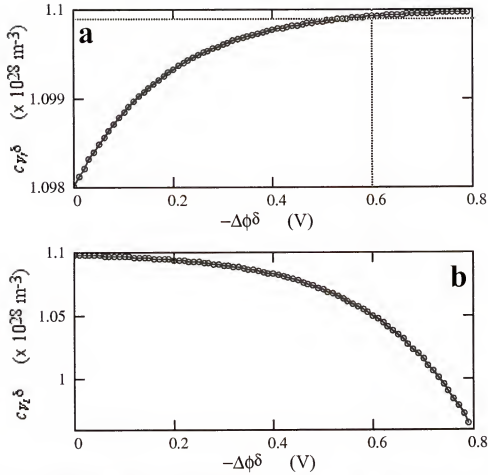
Figure 4-6. Oxygen vacancy concentration (a) at the interface and (b) on the air side, versus potential difference across the ESB layer at 800 °C.

Figure 3-13. What is more interesting about Figure 4-6a though, is that it shows that for $-\Delta\phi^\delta < 0.6$ V, $c_{V_I} < 1/2 \, c_A^\delta$. The reason this is important is that ESB decomposes in $P_{O_2} < \sim 10^{-13}$ atm. or for $-\Delta\phi^\delta > \sim 0.66$ V because those conditions generate more oxygen vacancies in ESB than it can support stably. Figure 4-4a shows that for $-\Delta\phi^\delta < 0.6$ V $c_{V_I} < 1/2 \, c_A^\delta$ and ESB should be quite stable.

4.3. Summary

In this chapter, the feasibility of a bilayered electrolyte consisting of a layer of SDC on the fuel (reducing side) side and ESB on the air (oxidizing) side of an SOFC was

studied. Expressly, the feasibility of the bilayered electrolyte depends on the optimization of the thickness ratio, τ, of the layers so that the ESB layer is protected from decomposition in a highly reducing (low P_{O_2}) atmosphere while the ionic conductance of the combination is maximized. Consequently, it was necessary to obtain a stability criterion for ESB and its functional relationship to τ. It was argued that in *open-circuit* conditions it was sufficient to know the P_{O_2} at the SDC-ESB interface while in *closed-circuit* conditions it was necessary to ascertain the voltage drop, $-\Delta\phi^\delta$, across the ESB layer.

In *open-circuit* conditions, the models developed for oxygen flux in Chapters 2 and 3 were used to obtain the functional relationship between the τ and the effective P_{O_2} at the SDC-ESB interface. Both approaches (from Chapter 2 and Chapter 3) produced almost identical results, further substantiating their validity. In *closed-circuit* conditions, the models developed for defect flux in Chapter 3 were used to obtain the functional relationship between τ and $-\Delta\phi^\delta$.

Finally, at 800 °C, the bilayer model showed that τ should be ~8 in *open-circuit* conditions and ~0.25 in *closed-circuit* conditions for appropriate protection of the ESB layer. At 500 °C, τ should be ~6.5 in *open-circuit* conditions and ~0.11 in *closed-circuit* conditions. In addition, because ESB has a higher ionic conductivity than SDC, a higher total ionic conductance for the bilayer is obtained for the smaller value of τ. And for the most efficient delivery of power, one would prefer the highest total ionic conductance allowable. This implies that an SDC-ESB bilayered SOFC should best be operated in such a way that *open-circuit* conditions are never experienced by the SOFC when a reducing gas is present on the fuel side. This is not a problem since in principle a fuel cell is used to deliver current to a load. Moreover, *open-circuit* conditions in the presence of a reducing gas are easily avoided by removing the gas. In other words, when the SOFC is to be shut off the reducing gas can be pumped away first or alternatively (and perhaps more cheaply) air can be allowed to flow into the fuel side. Another approach may be to just

allow the fuel cell to cool since the decomposition P_{O_2} for ESB decreases with temperature. This solution is attractive because of its simplicity, however it would have to be carefully implemented since the effective P_{O_2} of the fuel also reduces with temperature.

CHAPTER 5
CONCLUSIONS

Now that the end is near, and its time to face the final curtain, a review of the accomplishments and failures of the models developed in this work is pertinent and is discussed below.

In Chapter 2 point defect equilibria was used to develop, analytically, expressions describing the dependence of point defect generation on oxygen partial pressure, P_{O_2}, in mixed ionic-electronic conductors (MIECs) with the fluorite and perovskite structures. The model was able to reproduce the results of the established Brouwer approach [14] in the Brouwer regimes. Unlike the Brouwer approach [14], however, the models were not discontinuous across two Brouwer regimes.

A case study was done for samaria-doped ceria (SDC) in which the model was (a) compared to numerical solutions of SDC defect equilibria (b) used to obtain values for the external equilibrium constant, K_r, (c) fitted to experimental data for total (ionic plus electronic) conductivity as a function of P_{O_2}, (d) used to obtain an analytical solution of Wagner's equation for ambipolar flux without simplifying assumptions and (e) used to evaluate the impact of defect associates on (unassociated) oxygen vacancy concentration. Thus far, each application of the model was successful and suggests that it has some promise. As with any model however, its usefulness is heavily dependent on the accuracy and accessibility of the material constants (such as K_r and the ratio of defect diffusivities, Θ) contained therein. Consequently, much time, effort and discussion was devoted to how K_r could be obtained from thermodynamic tables (and arguments), data from *open-circuit* voltage (OCV) measurements (repeated in Chapter 3) and thermogravimetric data.

Through these efforts the term $K_r(3+4\Theta)^2$ was shown—Eq. (2.4.12)—to constitute a material constant. That agrees with the cooperative relationship that K_r and Θ share in the exchange of oxygen at the MIEC-gas interface. Furthermore, the ability of ceria (i.e., cerium (IV) oxide) to support defects (in this case, oxygen vacancies and electrons) rather than decomposing to cerium (III) oxide was correlated to its ability to (rapidly) supply the oxygen exchange reaction—Eq. (2.3.2)—with electrons (in oxidizing conditions) or sustain electrons formed during the exchange (in reducing conditions). This argument may be extended to other oxides—such as erbia-stabilized bismuth oxide (ESB) and lanthanum strontium manganate—whose decomposition in reducing environments may be interpreted as their inability to assimilate electrons (formed by the loss of oxygen to the lattice) fast enough. This reluctant assimilation of electrons precipitates their decomposition to forms more stable in reducing environments.

In Chapter 3 the fundamental laws of (mass and charge) transport—i.e., the Nernst-Planck and material balance equations—are used to derive models for the spatial distribution and transport of defects in an MIEC with a P_{O_2} gradient across it. The first model (the linear potential model) assumed that a linear potential gradient existed across the MIEC. This model was found to be most applicable to MIECs without an oxygen vacancy (i.e., the ionic species) concentration gradient (i.e., true electrolytes). The second model (the non-linear potential model) was developed without the assumption of a linear potential gradient across the MIEC. This model had general application to all MIECs and reduced to the linear potential model when the oxygen vacancy concentration approached uniformity. Although its potency is hardly diminished, it is regrettable that the non-linear potential model produced a trancendental function from which the defect concentration dependence on position has to be extracted numerically. Despite the prevalence and power of modern computers and software the non-linear potential model would have been that much more usable if that could be avoided.

As an advance over present models, *potential dependent* rather than *fixed* boundary conditions were used for both models. In the case of the linear potential model, the effect of *potential dependent* versus *fixed* boundary conditions, was thoroughly examined. *Fixed* boundary conditions were often found to give erroneous, impractical and misleading results for the spatial distribution and transport properties of defects.

Finally, the model (both models are identical under *open-circuit* conditions) was applied to experimental data consisting of OCV measurements for various reducing side P_{O_2} values from 500 °C to 800 °C. Excellent fits of the model to the experimental data were obtained which thereby demonstrated the correctness of the model. Moreover, since unique values were obtained from the best fits for the material constants K_r and Θ, the model has the potential to separate the impact of K_r and Θ on the behaviour of the MIEC. Unfortunately, however, both K_r and Θ were affected by the presence of metallic electrodes and possibly defect associates. Nevertheless, instead of searching for the values of K_r and Θ for a material, it may be more useful—at least from an engineering (versus scientific) perspective—to think of K_r and Θ as defining a system consisting a specific MIEC-electrode combination. For technological applications, it is more important to be able to evaluate the characteristics of a system rather than its constituents. This way of thinking doesn't obviate the need to be able to measure the fundamental material properties but provides a useful alternative.

In Chapter 4 the models developed in Chapters 2 and 3 were used to determine the optimal thickness ratio of an SDC\ESB bilayered electrolyte under *open-circuit* and *closed-circuit* conditions. The bilayer model predicts that, under *closed-circuit* conditions, a layer of SDC can protect a layer of ESB from reaching its decomposition potential (equivalent to a voltage). Moreover, the SDC layer need not be thicker than the ESB layer to protect it because SDC is more *ionically* resistive than ESB. Conversely, in *open-circuit* conditions, where ESB is more resistive to ambipolar oxygen permeation than SDC; the SDC layer has to be thicker than the ESB layer to offer protection from its

decomposition potential (equivalent to a P_{O_2}). In both cases, the SDC\ESB thickness ratio may be improved ($\tau \rightarrow 0$) by going to a lower temperature if the permeative/electrical resistivity for SDC grows faster (with decreasing temperature) than for ESB.

Overall, the modeling exercises showed how the defect equilibria of an MIEC, could be combined with the relevant thermodynamics and transport laws to fully describe its performance in a P_{O_2} gradient or in an equipotential P_{O_2} environment. Moreover, the usefulness of the models to extract information from experimental data and to advance device application is clear.

APPENDIX A
EVALUATING K_- AND K_+ FOR THE SMALL POLARON
FORMATION REACTION

It is safe to assume that when there are only a few electrons or holes in the MIEC, then nearly all of them are in the form of small polarons (see Figures 2-3 and 2-4), i.e., each electron or hole is trapped on a cation site in the form of M'_{cat} or $M^{\bullet}_{cat}$ for *negatively* or *positively charged* small polarons respectively. Accordingly, from Eqs. (2.3.32) and (2.3.33), the concentration of itinerant electrons and holes ($c_{e>}$ and $c_{h>}$ respectively) is negligibly small (i.e., $c_{e>} = c_{h>} \approx 0$). Mathematically, this description may be expressed as:

$$\lim_{c_e \to 0} c_{sp-} = c_e \tag{A1}$$

and

$$\lim_{c_h \to 0} c_{sp+} = c_h \tag{A2}$$

where c_e, c_h, c_{sp-} and c_{sp+} are the concentrations of electrons, holes, *negatively* and *positively charged* small polarons respectively. Combining Eq. (2.3.16) and Eq. (A1) yields

$$\lim_{c_e \to 0} K_- = \lim_{c_e \to 0} \frac{c_{sp-}}{c_{cat} \cdot c_e} = \lim_{c_e \to 0} \frac{c_{sp-}}{\left(c_{cat} - c_{sp-}\right)c_e} = \lim_{c_e \to 0} \frac{c_e}{\left(c_{cat} - c_e\right)c_e} = \frac{1}{c_{cat}} \tag{A3}$$

where c_{cat° and c_{cat} are the concentration *uncharged* (relative to the cation site) cations and the total cation concentration, respectively. Similarly, combining Eq. (2.3.17) and Eq. (A2) yields

$$\lim_{c_h \to 0} K_+ = \lim_{c_h \to 0} \frac{c_{sp+}}{c_{cat^\circ} c_h} = \lim_{c_h \to 0} \frac{c_{sp+}}{\left(c_{cat} - c_{sp+}\right) c_h} = \lim_{c_h \to 0} \frac{c_h}{\left(c_{cat} - c_h\right) c_h} = \frac{1}{c_{cat}} \quad (A4)$$

At first glance, the results in Eqs. (A3) and (A4) seem to imply that the equilibrium constants K_- and K_+, are determined by c_{cat}, rather than the free energy of the small polaron formation reactions and temperature. However, the results are artifacts arising from defining K_- and K_+ in terms of defect concentrations—in Eqs. (2.3.16) and (2.3.17) respectively—instead of activities or mole fractions both which would have made K_- and K_+ dimensionless. K_- and K_+ were so defined at that point (in section 2.3.2) for convenience and consistency. However, to gain insight into small polaron formation, they are now rewritten in terms of mole fractions as follows

$$K_- = \frac{X_{M_{cat}'} N_c}{X_{M_{cat}^\times} c_e} \quad (A5)$$

and

$$K_+ = \frac{X_{M_{cat}^\bullet} N_v}{X_{M_{cat}^\times} c_h} \quad (A6)$$

where X is the mole fraction and N_c and N_v are the density of states per unit volume in the conduction and valence bands respectively. The mass balance equation in Eq. (2.3.19) should also be replaced by

$$X_{M_{cat}'} + X_{M_{cat}^\times} = 1 \quad (A7)$$

if the MIEC is dominated by *negatively charged* small polarons, and by

$$X_{M_{cat}^\bullet} + X_{M_{cat}^\times} = 1 \tag{A8}$$

if the MIEC is dominated by *positively charged* small polarons.

Applying the rationale outlined earlier in Eqs. (A1) through (A4), then for *negatively charged* small polarons:

$$\lim_{c_e \to 0} X_{M_{cat}'} = \frac{c_e}{N_c} \tag{A9}$$

and

$$\lim_{c_e \to 0} K_- = \lim_{c_e \to 0} \frac{X_{M_{cat}'} N_c}{X_{M_{cat}^\times} c_e} = \lim_{c_e \to 0} \frac{X_{M_{cat}'} N_c}{\left(1 - X_{M_{cat}^\times}\right) c_e} = \lim_{c_e \to 0} \frac{c_e}{\left(1 - \frac{c_e}{N_c}\right) c_e} = 1 \tag{A10}$$

Similarly, for *positively charged* small polarons

$$\lim_{c_h \to 0} X_{M_{cat}^\bullet} = \frac{c_h}{N_v} \tag{A11}$$

and

$$\lim_{c_h \to 0} K_+ = \lim_{c_h \to 0} \frac{X_{M_{cat}^\bullet} N_v}{X_{M_{cat}^\times} c_h} = \lim_{c_h \to 0} \frac{X_{M_{cat}^\bullet} N_v}{\left(1 - X_{M_{cat}^\bullet}\right) c_h} = \lim_{c_h \to 0} \frac{c_h}{\left(1 - \frac{c_h}{N_v}\right) c_h} = 1 \tag{A12}$$

The *activation energies*, for the formation of *negatively* and *positively charged* small polarons may be defined as $\Delta G_- = -k_B T \ln K_-$ and $\Delta G_+ = -k_B T \ln K_+$ respectively.

Therefore if $K_- = K_+ = 1$, then $\Delta G_- = \Delta G_+ = 0$. This result suggests that the "reaction" to form small polarons—in Eqs. (2.3.16) and (2.3.17)—is not characterized by an activation energy. This is not incredible since, according to Madelung [24], the binding energy, E, of a small polaron in its potential well is given by:

$$E = -\frac{q^2}{16\pi\varepsilon_0 r_p}\left(\frac{1}{\varepsilon(\infty)} - \frac{1}{\varepsilon(0)}\right) = -\frac{m^* q^4}{128\pi^2\varepsilon_0^2\hbar^2}\left(\frac{1}{\varepsilon(\infty)} - \frac{1}{\varepsilon(0)}\right)^2 \qquad (A13)$$

where q is the charge on an electron; r_p is the radius of the small polaron; ε_0 is the permittivity of free space; $\varepsilon(\infty)$ is the relative permittivity outside the potential well and $\varepsilon(0)$ is the relative permittivity inside the potential well; m^* is the effective mass of the electron (small polaron); and $\hbar$ is Planck's constant. None of the terms in the equation for the binding energy of a small polaron is characterized by an activation energy so the estimation of $\Delta G_{-,+} = 0$ seems appropriate. Moreover, the formalism of Eq. (A13)—and its development by Madelung [24]—suggests that the formation a small polaron is electrostatic in nature. Additionally, one may also deduce that the trapped electron must then be supplied with enough energy (usually thermal) to escape the energy well and respond to an electric field.

APPENDIX B
DEFECT GENERATION FORMULAE FOR OXYGEN INTERSTITIALS AND CATION VACANCIES

Expressions for the concentration of oxygen interstitials, c_{O_i}, and metal vacancies, $c_{V_{A,B}}$, on the A-site or the B-site (hence the sub-sub-script "A, B") may be obtained for the *Low, Intermediate and High* P_{O_2} regions and for a general solution by combing Eqs. (2.3.4) through (2.3.10), (2.3.23), (2.3.24), (2.3.37), (2.3.39), (2.3.41), (2.3.43), (2.3.48), (2.3.50) and (2.3.53) through (2.3.61). The results are listed below

Low P_{O_2} region

$$c_{O_i}(P) = K_f c_{V_O}^{-1} = K_f \left[\frac{3}{4} K_r^{\frac{1}{2}} P^{-\frac{1}{4}} + \left(\frac{1}{2} c_A \right)^{\frac{3}{2}} \right]^{-\frac{2}{3}} \tag{B1}$$

and

$$c_{V_{A,B}} = K_{s_{A,B}}^{\frac{1}{2}} c_{V_O}^{-\frac{3}{2}} = K_{s_{A,B}}^{\frac{1}{2}} \left[\frac{3}{4} K_r^{\frac{1}{2}} P^{-\frac{1}{4}} + \left(\frac{1}{2} c_A \right)^{\frac{3}{2}} \right]^{-1} \tag{B2}$$

Intermediate P_{O_2} region

$$c_{O_i}(P) = K_f c_{V_O}^{-1} = \frac{1}{16} K_f \left[\sqrt{K_m P^{\frac{1}{2}} + 8 c_A} - K_m^{\frac{1}{2}} P^{\frac{1}{4}} \right]^{-2} \tag{B3}$$

and

APPENDIX C
MODELING THE ACCOMMODATION OF CUBIC BISMUTH OXIDE IN THE FLUORITE STRUCTURE

The stoichiometry of bismuth oxide, Bi_2O_3, suggests that it should not be able to crystallize in the fluorite structure, which ordinarily requires a 1:2 cation to anion ratio (e.g., CaF_2, ZrO_2). In order to conform bismuth oxide to the defect equations and models discussed and developed in Chapter 2 it is convenient to think of it as a "dopant" in a fluorite lattice as follows

$$Bi_2O_3 \xrightarrow{FlO_2} 2Bi'_{Fl} + V_O^{\bullet\bullet} + 3O_O^{\times} \tag{C1}$$
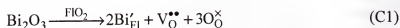
where FlO_2 is a hypothetical fluorite oxide representing the fluorite structure containing a typically charged Fl^{4+} cation (e.g., Zr^{4+}). The corresponding charge neutrality equation is

$$c_A = c_{Bi'_{Fl}} = 2c_{V_O} \tag{C2}$$

Consequently, there is one oxygen vacancy for each pair of bismuth atoms. In addition, the stoichiometry of Bi_2O_3—also seen in Eq. (B1)—shows that there are three oxygen atoms for each pair of bismuth atoms, i.e.,

$$3c_{Bi'_{Fl}} = 2c_{O_O} = 6c_{V_O} \tag{C3}$$

In other words, the oxygen atoms occupy three quarters of the available anion sites leaving one quarter of them vacant.

This description of bismuth oxide allows its behaviour (i.e., regarding defect generation, distribution and transport) to be treated by the defect equations and models discussed and developed in Chapters 2, 3 and 4 without modification.

REFERENCES

[1]   B. C. H. Steele, *J. Mat. Sci.* **36** (2001) 1053.

[2]   S. C. Singhal, *Solid State Ionics* **135** (2000) 305.

[3]   P. Vernoux, M. Guillodo, J. Fouletier and A. Hammou, *Solid State Ionics* **135** (2000) 425.

[4]   Jin H. Choi, Jong H. Jang and Seung and M. Oh, *Electrochimica Acta* **46** (2001) 867.

[5]   P. Charpentier, P. Fragnaud, D. M. Schleich and E. Gehain, *Solid State Ionics* **135** (2000) 373.

[6]   J. Will, A. Mitterdorfer, C. Kleinlogel, D. Perednis and L. J. Gauckler, *Solid State Ionics* **131** (2000) 79.

[7]   B. C. H. Steele, *Solid State Ionics* **129** (2000) 95.

[8]   Mogens Mogensen, Nigel M. Sammes and Geoff A. Tompsett, *Solid State Ionics* **129** (2000) 63.

[9]   V. V. Kharton and F. M. B. Marques, *Solid State Ionics* **140** (2001) 381.

[10]   J. Newman, Electrochemical Systems (Prentice-Hall, 1991).

[11]   O. Porat and H. L. Tuller, *J. Electroceramics* **1** (1997) 42.

[12]   F. W. Poulsen, *Solid State Ionics* **129** (2000) 145.

[13]   F. W. Poulsen, *J. Solid State Chem.* **143** (1999) 115.

[14]   G. Brouwer, *Philips Res. Rep.* **9** (1954) 366.

[15]   I. Kosacki, H. L. Tuller, *Solid State Ionics* **80** (1995) 223.

[16]   I. Kosacki, T. Suzuki, V. Petrovsky and H. U. Anderson, *Solid State Ionics* **136** (2000) 1225.

[17]   G. B. Zhang and D. M. Smyth, *Solid State Ionics* **82** (1995) 161.

[18]   O. Porat, Ph.D. Thesis, The Technion, Israel Institute of Technology (1994).

[19]   O. Porat and I. Riess, *Solid State Ionics* **81** (1995) 29.

[20]   G. Spinolo and U. Anselmi-Tamburini, Ber. Bunsenges, *Phys. Chem* 99 (1995) 87.

[22]   N. Bonanos and F. W. Poulsen, *J. Mater. Chem.* **9** (1999) 431.

[23]   M. Barsoum, in Fundamentals of Ceramics (McGraw-Hill, 1977).

[24]   O. Madelung, in Introduction to Solid State Theory (Springer-Verlag, 1978).

[25]   P. J. Wilde and C. R. A. Catlow, *Solid State Ionics* **112** (1998) 173.

[26]   G. Ch. Kostogloudis, P. Fertis and Ch. Ftikos, *Solid State Ionics* **118** (1999) 241.

[27]   L. -W. Tai, M. M. Nasrallah, H. U. Anderson, D. M. Sparlin and S. R. Sehlin, *Solid State Ionics* **76** (1995) 259.

[28]   I. Kaus and H. U. Anderson, *Solid State Ionics* **129** (2000) 189.

[29]   H. Inaba and H. Tagawa, *Solid State Ionics* **83** (1996) 1.

[30]   T. Masui, K. Fujiwara, Y. Peng, T. Sakata, K. Machida, H. Mori and G. Adachi, *J. Alloys and Compounds* **269** (1998) 116.

[31]   S. Park, R. J. Gorte and J. M. Vohs, *App. Catal. A* **200** (2000) 55.

[32]   M. Sahibzada, B. C. H. Steele, K. Hellgardt, D. Barth, A. Effendi, D. Mantzavinos and I. S. Metcalfe, *Chem. Eng. Sci.* **55** (2000) 3077.

[33]   M. Sahibzada, B. C. H. Steele, D. Barth, R. A. Rudkin and I. S. Metcalfe, *Fuel* **78** (1999) 639.

[34]   R. Doshi, V. L. Richards, J. D. Carter, X. Wang and M. Krumpelt, *J. Electrochem. Soc.* **146** (1999) 1273.

[35]   V. Kharton, F. Figueiredo, L. Navarro, E. Naumovich, A. Kovalevsky, A. Yaremchenko, A. Viskup, A. Carneiro, F. Marques and J. Frade, *J. Mat. Sci.* **36** (2001) 1105.

[36]   H. L. Tuller and A. S. Nowick, *J. Electrochem. Soc.* **126** (1979) 209.

[37]   H. L. Tuller and A. S. Nowick, *J. Electrochem. Soc.* **122** (1975) 255.

[38]   J. Hwang and T. O. Mason, *Zeitschrift fur Physikalische Chemie* **207** (1998) 21.

[39]   T. G. Stratton and H. L. Tuller, *J. Chem. Soc., Faraday Transactions 2.* **83** (1987) 1143.

[40]   W. H. Strehlow and E. L. Cook, *J. Phys. Chem. Ref. Data* **2** (1973) 163.

[41]   I. Riess, *J. Electrochem. Soc.* **128** (1981) 2077.

[42]   S. Yuan and U. Pal, *J. Electrochem. Soc.* **143** (1996) 3214.

[43]   I. Barin in *Thermochemical Data of Pure Substances 3rd. ed.* (VCH, New York, 1995).

[44]   M. Godickemeier, K. Sasaki, L. Gauckler and I. Riess, *J. Electrochem. Soc.* **144** (1997) 1635.

[45]   M. Godickemeier and L. Gauckler, *J. Electrochem. Soc.* **145** (1998) 414.

[46]   S. Wang, H. Inaba, H. Tagawa, M. Dokiya and T. Hashimoto, *Solid State Ionics* **107** (1998) 73.

[47]   T. Kobayashi, S. Wang, M. Dokiya, Hiroaki T. and T. Hashimoto, *Solid State Ionics* **126** (1999) 349.

[48]   P. W. Atkins, in Physical Chemistry, 4th edition (Oxford University Press, Oxford 1990).

[49]   K. Eguchi, T. Setoguchi, T. Inoue and H. Arai, *Solid State Ionics* **52** (1992) 265.

[50]   H. L. Tuller in: Nonstoichiometric Oxides, ed. O. Sorensen (Academic Press, New York, 1981) chap. 6, pp. 271.

[51]   W. Huang, P. Shuk, M. Greenblatt, *J. Electrochem. Soc.* **147** (2000) 439.

[52]   C. H. Lee and G. M. Choi, *Solid State Ionics* **135** (2000) 653.

[53]   C. Wagner, *Z. Elektrochem.* **60** (1956).4.

[54]   H. J. M. Bouwmeester and A. J. Burggraaf in: Handbook of Solid State Electrochemistry, ed. P. J. Gellings and H. J. M. Bouwmeester (CRC Press, 1997) chap. 14, p. 481.

[55]   J. E. ten Elshof, H. J. M. Bouwmeester and H. Verweij, *Solid State Ionics* **81** (1995) 97.

[56] J. A. Lane, S. J. Benson, D. Waller and J. A. Kilner, *Solid State Ionics* **121** (1999) 201.

[57] D. Schneider, M. Godickemeier and L. Gauckler, *J. Electroceramics* **1** (1997) 165.

[58] J. A. Kilner and B. C. H. Steele in: Nonstoichiometric Oxides, ed. O. Sorensen (Academic Press, New York, 1981) chap. 5, p. 271.

[59] I. Riess, *Solid State Ionics* **52** (1992) 127.

[60] A. Mineshige, T. Taji, Y. Muroi, M. Kobune, S. Fujii, N. Nishi, M. Inaba and Z. Ogumi, *Solid State Ionics* **135** (2000) 481.

[61] N. S. Choudhury and J. W. Patterson, *J. Electrochem. Soc.* **118** (1971) 1384.

[62] H. Näfe, *J. Electrochem. Soc.* **144** (1997) 265.

[63] M. Liu, *J. Electrochem. Soc.* **144** (1997) 1813.

[64] V. V. Kharton, A. P. Viskup, F. M. Figueiredo, E. N. Naumovich, A. A. Yaremchenko and F. M. B. Marques, *Electrochimica Acta* **46** (2001) 2879.

[65] J. O'M. Bockris and A. K. N. Reddy in Modern Electrochemistry, vol. 2 (Plenum Press, New York 1970).

[66] S. R. Morrison in, The Chemical Physics of Surfaces, 2nd edition (Plenum Press, New York 1977).

[67] R. J. D. Miller, G. L. McLendon, A. J. Nozik, W. Schmickler, F. Willig, in Surface Electron Transfer Processes (VCH, 1995).

[68] P. Shuk, H. -D. Wiemhöfer, U. Guth, W. Gopel and M. Greenblatt, *Solid State Ionics.* **89** (1996) 179.

[69] A. M. Azad, S. Larose and S. A. Akbar, *J. Mat. Sci.* **29** (1994) 4135.

[70] E. D. Wachsman and K. L. Duncan, in *Solid oxide fuel cells V*, S. C. Singhal and M. Dokiya ed. (1999) p. 264 Electrochem. Soc. Proc. Series.

[71] J. -Y. Park, M. Sc. Thesis, University of Florida, in preparation.

[72] M. R. Spiegel in, Schaum's Outline Series: Theory and Problems of Statistics 2nd. edition (McGraw-Hill, 1994).

[73] I. Riess and J. Schoonman in: Handbook of Solid State Electrochemistry, ed. P. J. Gellings and H. J. M. Bouwmeester (CRC Press, 1997) chap. 8, p. 269.

[74]   E. D. Wachsman, Ph. D. Thesis, Stanford University (1990).

[75]   E. D. Wachsman, N. Jiang, C. W. Frank, D. M. Mason, D. A. Stevenson, *Appl Phys A* **50** (1990) 545.

[76]   K. Mehta, S. J. Hong, J. -F. Jue and A. V. Virkar, in *Solid Oxide Fuel Cells III*, S. C. Singhal and H. Iwahara, ed., PV 93-4, p. 92, Electrochem. Soc. Proc. Series.

[77]   H. Yahiro, Y. Baba, K. Eguchi and H. Arai, *J. Electrochem. Soc.* **135** (1988) 2077.

[78]   E. D. Wachsman, P. Jayaweera, N. Jiang,, D. M. Lowe, and B. G. Pound, *J. Electrochem. Soc.* **144** (1997) 233.

[79]   P. Soral, U. Pal and W. L. Worrell, *J. Electrochem. Soc.* **145** (1998) 99.

[80]   S. Dikmen, P. Shuk and M. Greenblatt, *Solid State Ionics* **112** (1998) 299.

[81]   K. Q. Huang, R. S. Tichy, J. B. Goodenough, *J. Amer Ceram Soc.* **81** (1998) 2565.

[82]   K. Q. Huang, R. S. Tichy, J. B. Goodenough, *J. Amer Ceram Soc.* **81** (1998) 2576.

[83]   T. Takahashi, T. Esaka and H. Iwahara, *J. App. Electrochem.* **7** (1977) 303.

[84]   N. Jiang, M. Sc. Thesis, Stanford University (1994).

BIOGRAPHICAL SKETCH

I was born in St. Andrew, Jamaica at the University Hospital of the West Indies in 1968 to Merdean Bennett and Kenneth Duncan. My early life was spent in Kingston, Jamaica. For a few years I was raised as part of an extended family consisting of my mother, sister Ann (different father) my Aunt Phyllis and her two daughters: Charmaine and Sonia. We lived in a large old house which had been converted to a tenement yard. My first formal schooling begun when I was about three or four years old, at Miss Sissy's (basic) school—the equivalent to a pre-school. There I was introduced to the alphabet, multiplication tables, addition and subtraction and cursive writing. At five years old I moved on to Alpha Infant School. My mother wanted to send me to a private kindergarten but we could not afford it. At seven I moved on to Alpha Primary School. Entering the sixth grade at 10 years old, I was turned on to mathematics by Ms. Wolfe, a strict (she would beat us with sticks and canes if we misbehaved or did poorly on our assignments) teacher who expected a lot from her students.

After passing my common entrance examinations at eleven years old, I entered St. George's College (an all boys school). My interest in mathematics was further developed by Mr. White, a young but very earnest teacher. And I discovered the joys of physics in Mr. Douglas' and Fr. Larkin's classes. (Mr. White and Mr. Douglas eventually left teaching because they could not support their families with a teacher's salary.) After initially doing well at St. George's, the distractions of the teenage years threatened my academic development. By this time my mother and I were living in Portmore, a working class suburb of Kingston. While there I became involved in church at Portmore United

Church. Through the positive influence of my friends there I re-focused on doing my school work. More importantly however, I became a born again Christian in September 1983. With a new awareness of God and a growing desire to follow Him my life begun to take shape.

I entered the University of the West Indies, Mona in 1986. There I majored in applied physics and mathematics and received my B.Sc.. in applied physics in 1989. I spent the next year of my life working with a church affiliated social work institute. Ostensibly to fulfill my desire to serve God and find my place in Him. I didn't last long there, however, and I soon moved on. My yearning for God didn't die but I was bored with my job. I then taught at the College of Arts Science and Technology (now the University of Technology) from sixteen month before returning to the University of the West Indies to pursue (part time) a masters degree in Physics.

While studying for the masters degree, I had the opportunity to go to Argonne National laboratory in Illinois, USA. The experience was wonderful. I returned and got married to Nicole Waite in January 1995. I finished my masters degree and returned to the University of technology to teach. Unfortunately, my classes —the material not the students and hopefully not the teacher—which were all at the introductory level) were not very stimulating. I was getting bored. Moreover, my son was born in, November 1996 and I (like Mr. White and Mr. Douglas and numerous other teachers) was worried that I would not be able to afford to buy a house for family to live in. Both factors combined plus a genuine love for research discovered while at Argonne, created a desire to pursue a doctoral degree.

My initial efforts failed, but just as I was about to give up, God made a way for me. I was invited to visit the University of Florida, but I had only a day's notice. On such short notice it seemed impossible. The only flight available from Jamaica that I could get on (in time) was from Montego Bay a five hour drive from where I lived. God made a way and I was able to get everything together in time. My friends drove me there in the

dead of night and I was off. The rest, as they say, is history. I don't know what the rest of my life holds but, God has been good. He has provided for me and my family and I hope that I will hold His hand, hear His voice and heed His call.

I certify that I have read this study and that in my opinion it conforms to acceptable standards of scholarly presentation and is fully adequate, in scope and quality, as a thesis for the degree of Doctor of Philosophy.

Eric D. Wachsman, Chairman
Associate Professor of Materials Science
and Engineering

I certify that I have read this study and that in my opinion it conforms to acceptable standards of scholarly presentation and is fully adequate, in scope and quality, as a thesis for the degree of Doctor of Philosophy.
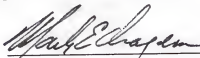
Robert T. Dehoff
Professor of Materials Science and
Engineering

I certify that I have read this study and that in my opinion it conforms to acceptable standards of scholarly presentation and is fully adequate, in scope and quality, as a thesis for the degree of Doctor of Philosophy.

Rolf Hummel
Professor of Materials Science and
Engineering

I certify that I have read this study and that in my opinion it conforms to acceptable standards of scholarly presentation and is fully adequate, in scope and quality, as a thesis for the degree of Doctor of Philosophy.

Mark Orazem
Professor of Chemical Engineering

I certify that I have read this study and that in my opinion it conforms to acceptable standards of scholarly presentation and is fully adequate, in scope and quality, as a thesis for the degree of Doctor of Philosophy.

Susan Sinnott
Associate Professor of Materials Science
and Engineering

This thesis was submitted to the Graduate Faculty of the College of Engineering and to the Graduate School and was accepted as partial fulfillment of the requirements for the degree of Doctor of Philosophy.

August 2001

Pramod P. Khargonekar
Dean, College of Engineering

Winfred M. Phillips
Dean, Graduate School